Evaluation of ocean heat advection role on sea surface temperature anomaly in ocean reanalysis models and Coupled Model Intercomparison Project phase 5 (CMIP5) models in western Indian Ocean

A Dissertation

by

IBNU FATHRIO

Submitted to the Graduate School of Science and Engineering
in partial fulfillment of the requirements
for the Degree of Doctor of Philosophy in Science

HIROSAKI UNIVERSITY
February 2018

Declaration of Originality

I hereby certify that I am the sole author of this thesis. This thesis contains no material which has been accepted for a degree or diploma by the University or any other institution, except by way of background information and duly acknowledged in the thesis, and to the best of my knowledge and belief no material previously published or written by another person except where due acknowledgement is made in the text of the thesis, nor does the thesis contain any material that infringes copyright.

Ibnu Fathrio
February 2018

Abstract

Recently, the state-of-the-art coupled global circulation models in coupled model intercomparison project phase five (CMIP5) are still modulated by a systematic bias in simulating sea surface temperature (SST) in the western Indian Ocean (WIO). It was shown that positive-Indian Ocean dipole (IOD)-like bias presents during boreal autumn. Previous studies have shown that weak southwest summer monsoon creates warm SST bias in WIO. In boreal autumn, Bjerknes feedback helps to amplify the warm SST biases into an IOD-like bias pattern, with easterly wind bias and an unrealistic mean thermocline slope tilting upward toward the eastern Indian Ocean (EIO). This is accompanied by greater precipitation bias in WIO and less precipitation bias in EIO. However, the process to initiate warm SST bias under weak southwest monsoon remains unclear. The role of ocean advection to the SST bias has not been fully discussed yet. Therefore, the main objective of this study is to investigate the ocean advection role in forming SST bias under weak southwest summer monsoon bias in CMIP5 models. We studied the role by analyzing how the advection process in ocean reanalysis models initiates the SST anomaly under weak and strong southwest monsoon.

In this study, we analyzed four ocean reanalysis models namely: GECCO2, SODA3, ORAS4, and GODAS. Heat budget analysis showed that there is a strong relationship between mixed layer temperature anomaly (as a proxy of SST) in WIO and the advection process. The results showed zonal advection is the important process to initiate SST anomaly in western equatorial Indian Ocean (WEIO), while vertical advection initiates the SST anomaly in the western Arabian Sea (WAS) and the southwestern Indian Ocean (SWIO).

More detailed investigation on CMIP5 models shows that about half of models pronounce warm SST bias, while the other half of models pronounce cool SST bias. The models with warmer SST biases exhibit a pattern that is similar to the IOD, with stronger equatorial easterly wind biases during fall and a deeper thermocline in the western equatorial Indian Ocean. In the models with cooler SST biases, negative SST biases are observed over the entire tropical Indian Ocean throughout the year and the wind biases over the equatorial Indian Ocean are southeasterly during summer and fall. The new findings of this study reveal the role of ocean current in forming the early summer development of SST biases over the WEIO. Heat budget analysis showed the formation of SST biases is related to surface current biases induced by the weaker

biases of southwesterly monsoon winds and SST biases over the southwestern equatorial Indian Ocean, which is advected by the East African Coastal Currents.

This study is highly significant for further understanding the evolution of systematic bias of SST over WIO. This study suggested realistic simulation of western boundary current in CMIP models is important to reduce the SST bias. It was documented that the CMIP5 models show a future IOD-like climate change. The peak of the SST warming over the WEIO occurs off the equator, somewhat similar to the biases in the historical simulations among the CMIP5 models. Examination of the process causing the future SST changes over the western Indian Ocean will be performed in future work.

Acknowledgements

Alhamdulillah, all praises to Allah for the strengths and His blessing in completing this dissertation. The dissertation is specially dedicated to Prof. Yasu-Masa Kodama and his families. I am very grateful to my supervisor Prof. Yasu-masa Kodama, for his guidance, encouragement and patience during my study and early life in Japan. His spirit and dedications always motivate every student.

I thank to Prof. Atsuyoshi Manda and Dr. Satoshi Iizuka as supervisors for their guidance and patience for me to finish the dissertation and their big contribution to published papers.

I thank to all supervisors, Prof. Masahiro Kosuga, Dr. Sachinobu Ishida, Dr. Tomoyuki Nagase, Prof. Akiyo Yatagai and Prof. Yukihiro Nojiri for their supports, comments and suggestion for this dissertation.

I thank the Ministry of Research and Technology (RISTEK), Indonesia, for their funding support under the RISTEK scholarship program

I thank to LAPAN, especially for Prof. Thomas Djamaluddin, Dr. Didi Satiadi and Halimurrahman, MT for their continuous support to complete the doctoral program

I sincerely thank to my parents and brothers, my lovely wife, dear Yanti and my little strong boy Ghaisan, who always encourage and inspire me in all conditions and all my families in Indonesia.

I thank to all Muslim brothers in Japan, especially in Hirosaki and Aomori.

Table of Contents

List of Figures

List of Table

1 Introduction

The oceans cover around 70 percent of the Earth's surface. Oceans are tightly linked to the atmosphere and together with atmosphere form the most dynamic component of the climate system. Oceans play an important role in shaping our weather and climate and in global warming. Patterns of ocean circulation and upwelling can affect climate variability. However, the oceans are among the most poorly known and understood, because of data sparseness. This study mainly discusses about the ocean. Before proceeding to the main discussion, it is important to review some basic knowledge about vertical ocean structure briefly.

1.1 Vertical Structure of the ocean

Based on density stratification, the ocean vertical structure can be divided into three vertical regions, namely, ocean mixed layer, pycnocline and the deep water (Figure 1.1). The upper ocean layer is warmed by incoming solar radiations. This condition makes the water near the surface has density lighter than that of water at deeper layer. The upper layer of water, at the uppermost 100m, is still influenced by surface wind. The surface wind induces the ocean surface current that is responsible for redistributing ocean water mass, heat and salinity.

The ocean mixed layer, typically tens of meters deep below the surface, is the ocean layer where the temperature and salinity is well mixed. This is characterized by vertically uniform properties of temperature, salinity and density. In the mixed layer, exchange of momentum, energy and heat occurs between the atmosphere and the ocean. The water in the mixed layer experiences warming and cooling by shortwave, longwave radiation and sensible heat flux. Cooling could also be attributed to latent heat loss due to evaporation. Mixing at the upper mixed layer could be caused by the winds, waves, and buoyancy fluxes. In the lower layer, the entrainment driven by large turbulent eddies in the base of mixed layer mixes the denser and cold water below the base of mixed layer. Mixing with cold water deepens the mixed layer depth. These changing of mixed layer properties, in turn, could greatly influence the weather and climate.

One of the causes of mixed layer cooling is ocean upwelling (Figure 1.2). Ocean upwelling is oceanographic phenomenon when the cool and deep water rises and

replaces warm water at the surface. This is induced by the wind, which pushes the water away from an area. The water is transported a net of 90° degrees from the direction of the wind due to Coriolis forces and Ekman transport. Upwelling usually brings nutrient rich water to ocean surface that is beneficial for fisheries. Upwelling can occur in the open ocean and along coastlines. One of well-known coastal upwelling areas is upwelling near Oman-Somali coast (Figure 1.2a), which is induced by strong southwesterly monsoon wind in boreal summer. In open ocean, the upwelling happens in the equatorial region i.e. in equatorial Pacific Ocean. In the equatorial Pacific, the wind blows westward near the equator (Figure 1.2b). The wind stress induces Ekman transport which is directed at 90° to the direction of the wind. In the north (south) of equator, the trade winds move the surface water northward (southward) away from the equator. It creates divergence at the equator that brings the deep and cold water to the surface that is rich of nutrient. As a result, broad line of high phytoplankton concentration is detected by satellite observation in the equatorial Pacific Ocean.

The layer in between the mixed layer and deep layer is the pycnocline, the layer where the density changes rapidly because of changes in temperature and salinity. The denser water could be attributed by colder temperature and/or contains more salt. The pycnocline could also be considered as thermocline and/or halocline. If the changes of density are attributed to changes of temperature (salinity), the pycnocline could be considered as thermocline (halocline). The depth of thermocline is an important part of air-sea interaction. Thermocline variations may influence the weather and climate through sea surface temperature (SST) variations. For example, thermocline dome in southwestern Indian Ocean (SWIO) greatly influences the SST variations. The ocean layer below pycnocline is the deep layer. The deep layer is the layer with the dark, cold layer below the pycnocline. In this layer, temperature and salinity vary little with depth. The density increases gradually with depth and water moves slowly.

1.2 Variability in Indian Ocean

Indian Ocean is the largest warm pool on Earth that has important role on weather and climate condition in the world. Indian Ocean enclosed to the west by African continent, maritime continent and Australia continent to the east, and Asian continent to the north, which makes the Indian Ocean differs from Pacific and Atlantic Ocean. It joins Atlantic Ocean in the south of Africa and Pacific Ocean in the Southeast.

Being bounded by Asian Continent prevents the northward heat transport and only weak ventilation of Indian Ocean thermocline from the north (Schott et al., 2009) is allowed.

Variations of SST in tropical Indian Ocean are important subject of study as local and remote effects greatly influence the atmosphere in many regions. When El Niño Southern Oscillation (ENSO) and Indian Ocean dipole (IOD) occurred in year of 1997, it caused disaster in many countries. Several thousands of deaths happened in Peoples of East African countries, e.g. Somalia, Ethiopia, Kenya, Sudan and Uganda, because of flooding happened during October and November. Flooding also destroyed crops and large numbers of livestock were drowned which cause major food deficit. In the western part of Indian Ocean, Southeast Asian countries suffered severe drought and it caused forest fire producing smokes and haze. Beside great economic loss, the smoke and haze caused heart and respiratory disorder for people's health. In Indonesia, the local governments had to stop academic activities for long period because of smokes and furthermore it disrupted transportation and caused airport closing.

1.2.1 Seasonal variations in Indian Ocean

Monsoon is originated from Arabic word known as "season". The monsoon circulation is known as giant land-sea breeze. Land-sea breeze is mainly caused by difference in heat capacity between sea and land surface. During the day, the land surface warms faster than the ocean surface because heat capacity of ocean is greater than land surface. The air temperature above the land surface is heated, lighter than surrounding and raises which makes the pressure over the land is lower than that over ocean surface. This condition makes the air over the ocean flows towards the land and replaces the lighter air mass aloft. Relatively thicker ocean surface than land surface penetrated by sunlight also contribute to unequal heating between ocean surface and land surface.

Seasonal wind reversal occurs over India and Southeast Asia, northern Australia, and West and central Africa. This is accompanied by seasonal variation of surface temperature and precipitation (Figure 1.3 and 1.4). These regions are the major monsoons of the global circulation according to Ramage classification (1971). Monsoon presents due to a thermal contrast between the land and the ocean. Large continent i.e. Asia, Africa, and Australia warm faster during spring and summer due to

greater heat capacity than surrounding ocean. Greater contrast of temperature gradient between continent and oceans (Figure 1.3) allows greater wind over the ocean blows towards continent and brings more moisture from the surrounding ocean like a giant sea breeze. This results in greater precipitation during monsoon seasons (Figure 1.4). Changes of monsoon precipitation may impact many peoples. In monsoon countries like India, agriculture depends on monsoon precipitation. About 18 percent of India's economy is made up by agriculture and employs more than half of population. Greater precipitation in extreme monsoon season could bring disastrous impact i.e. flooding and landslide. Hence, variability and prediction of monsoon precipitation becomes very important to study.

In the north of the equator of Indian Ocean, the seasonal cycle is dominated by the Asian monsoon with reversals of wind from northeasterly in boreal winter to southwesterly in boreal summer (Figure 1.5). In boreal summer, strong southwesterly wind presents in Arabian Sea and Bay of Bengal (Figure 1.5c). Moisture is transported from the Indian Ocean and the Arabian Sea by southwesterly wind. This is particularly noticeable along the coast of East Africa. The Findlater Jet (Findlater, 1969) feeds moisture transport to the Indian summer monsoon. The southwesterly monsoonal wind converges over northern plains of Indian, which results in the highest precipitation in Asia continent. During winter, the northwesterly wind blows away from the Asian continent towards Indian Ocean (Figure 1.5a). Strong northeasterly wind presents in the Arabian Sea and Bay of Bengal, which transports dry air away from the Asia continent. In boreal spring and autumn season, the wind over Northern Indian Ocean is weaker than during boreal monsoon season (Figure1.5b and d). At the equator, there is semiannual variation of westerly wind burst that occurs during boreal spring and autumn season (Schott et al., 2009). In the Southern Hemisphere, the seasonal cycle of the winds is weak and it blows eastward throughout the year. The southeasterly wind is strongest when as the Asian summer monsoon develops. On the other hand, it is weaker in the rest of seasons.

Seasonal SST variations in the WIO displays strong seasonal than other regions in Indian Ocean. Before the summer monsoon onset, the SST over Northern Indian Ocean become warmest as a result of radiation heating due to clear sky and light winds. When southwest monsoon established, the strong southwesterly wind Findlater Jet induces the coastal upwelling in Somali-Oman coast. Coastal upwelling happens when the deeper ocean layer replaces the warmer water at the upper ocean layer, which is

pushed away the coastline by the Ekman transport. The SST returns to normal during boreal autumn when the southwesterly wind retreats (Slingo et al., 2004). During winter, strong cooling is caused by latent heat loss due to strong and dry northeasterly wind from the Asian continent.

The reversing seasonal monsoonal wind influences the ocean circulation in the tropics and northern Indian Ocean (Schott and McCreary, 2001). During boreal summer monsoon (Figure 1.6), the south equatorial current (10-15°S) is forced by monsoon flows westward throughout the year and it splits at coast of Madagascar into the Northeast Madagascar Current (NEMC) and East Madagascar Current. The NEMC flows northward and splits into southward flow through Mozambique Channel and northward East African coastal current (EACC). When southwesterly wind emerges in summer, the EACC crosses the equator and feeds Somali current together with South Equatorial Counter current (SECC). This northward current flows further to Arabian Sea as East Arabian Current (Tomczak and Godfrey, 1994). The Somali current can develop wind driven circulating ocean current called "gyre". When the Somali current crosses the equator, part of Somali current turns eastward while the other part recirculates and forms the Southern gyre. The Southwest Monsoon current (SMC) south of Srilanka flows eastward, fed partly by Somali current and West Indian Coastal Current (WICC). In this season, part of SMC supplies the eastward flowing East Indian Coastal current (EICC) in the Bay of Bengal.

During winter monsoon (Figure 1.7), the EACC joints southward flowing coastal current at 2-4°S and supply SECC. In the eastern boundary, the Java current flows southeastward along Sumatra coast. The Northwest monsoon current flows westward in the south of Srilanka, which partly supplies WICC and southward flowing Somali current. Meanwhile, the WICC and EICC flow westward during this season. During monsoon transition period in April-June and October-November when the monsoon wind relaxes, the semiannual westerly wind generates Yoshida–Wyrtki Jet (Yoshida, 1959; Wyrtki, 1979) that flows eastward at narrow band (2-2°S) along the equator (Figure 1.8). The Wyrtki Jet transport warm waters to the east and maintains the EIO warms.

Another important upwelling region near the Somali-Oman coast is known as Srilanka Dome (Vinayachandran and Yamagata, 1998) located in the southwestern Bay of Bengal and east of Srilanka. The strongest upwelling presents in July and retreats in September. In the Southern Indian Ocean, the upwelling dome exists in the southern

tropical Indian Ocean, called Seychelles dome (Vialard et al., 2009; Yokoi et al., 2008; Tozuka et al., 2010). Weak upwelling also presents along Sumatra and Java. This upwelling is sometimes enhanced due to modulation of IOD. The regions with strong upwelling are associated with shallow thermocline region as displayed in Figure 1.8.

1.2.2 Interannual variability

1.2.2.1 El Niño-Southern Oscillation (ENSO)

In equatorial Pacific there is powerful climatic and oceanic oscillation called El Niño-Southern Oscillation (ENSO). In the beginning, ENSO is still considered as two independent phenomena (Niedzielski, 2014), which comprises of Southern Oscillation and El Niño. Southern Oscillation is atmospheric phenomenon characterized by surface pressure difference between the eastern Pacific and Indian Ocean. Sir Gilbert Walker found that the anomaly of surface pressure in Southern Oscillation was driven by anomaly of surface wind and precipitation in Pacific and Indian Ocean (Lau and Waliser, 2011). Meanwhile the El Niño is oceanic phenomenon indicated by warmer SST anomaly in the Central and Eastern equatorial Pacific. This condition was observed by fishermen in Peru few centuries ago when the presents of anomalous ocean current led to warming of SST and decreased fish production. This co-occurred with increase of precipitation at that time. Not until second half of 20th century, Southern Oscillation and ENSO were considered interrelated with statistical evidence proposed by Berlage and De Boer (1960).

Bjerkness (1969) proposed the underlying mechanism than link between Southern Oscillation and El Niño. The wind circulation over the equatorial pacific was called as Walker Circulation (Figure 1.9b). Normal Walker circulation is characterized by easterly wind, which transport cold air from the eastern Pacific. The air is warmed up due to warmer SST in the western Pacific warm pool. The warmer air is moist and moves upwards resulting in precipitation. The air returns to the east and falls as cold and dry air in the western Pacific. The ocean structure differences in oceans along the equatorial Pacific is shown in thermocline depth. Thermocline is ocean layer indicated by steep changes of vertical temperature of the ocean. Thermocline separates ocean mixed layer, the upper ocean warm layer that is still influenced by atmosphere, and cold subsurface layer. Due to strong trade winds (easterly wind), upwelling in the eastern

equatorial Pacific is stronger than the western pacific. The upwelling raises cold water in the Eastern Pacific and shoals the thermocline there. Meanwhile, upwelling in the western equatorial pacific is weak hence the thermocline is deeper. Hence, the thermocline in the equatorial Pacific Ocean is inclined towards the west during normal condition. Anomaly condition from "normal walker circulation" is called El Niño (warm ENSO) and La-Niña (cold ENSO).

Bjerkness (1969) pointed out that ocean and atmosphere coupling is essential to the development of ENSO. The zonal difference of SST anomalies between western and eastern equatorial Pacific influence the Walker circulation in term of surface pressure gradients, trade winds, and precipitation. In turn, the anomalous atmospheric circulation causes the anomalous oceanic circulation that forms horizontal gradient of SST anomalies at the first places (Neelin, 2011). During warm phase of ENSO (El Niño) (Figure 1.9a), warm SST anomalies present in the central to eastern equatorial Pacific. The horizontal SST gradient and surface pressure gradient weakens which slows the easterly wind (trade winds). Changes in zonal SST distribution shift the center of convection in the western Pacific, indicated by the convergence of wind and rising motion, to the east. As a result, reduced precipitation occurs in the western equatorial Pacific. The anomalies also appear in the thermocline. Due to weakening trade winds, the upwelling is suppressed in eastern equatorial Pacific hence the thermocline is deeper than normal condition. The west-east thermocline slope along the equatorial Pacific is flatter. Conversely, the normal Walker circulation is strengthened during La Niña conditions (Figure 1.9c). The anomalous SST in eastern Pacific is colder than usual which strengthen the trade winds. There is enhanced precipitation and deepening of thermocline in western Pacific.

ENSO occurs every 3-7 years that has seasonal peaks on boreal winter, December, January and February (DJF). Few years are considered as extreme ENSO years occurred in 1982-1983, 1997-1998, 2015-2015 for El Niño and 1973-1975, 1975-1976, 1988-1989, 1998-1999, 1999-2000, 2007-2008, 2010-2011 for La Niña (www.ggweather.com). The remote effects of ENSO, called teleconnection, affects changes in temperature and precipitation in Southeast Asia, India, Africa, USA and South America, etc. ENSO controls the weather conditions in the remote area by modifying the airflow and modifies location of low-high pressure centers. ENSO-induced precipitation anomaly could indirectly affects the hydrological cycle in the

remote region which further impacts not only to environmental issues, but also social and economic.

Observation and modeling studies showed there is connection between SST anomalies in the equatorial Pacific and SST anomalies in North Pacific, North Tropical Atlantic, and Indian Oceans during boreal winter and spring. Changes in location of center of convection in equatorial Pacific during extreme phase of ENSO induces anomaly of circulation in remote regions via atmospheric wave adjustment called as "atmospheric bridge" (Alexander et al., 2002; Liu and Alexander, 2007). Warming in the Indian Ocean basin presents about one season after peaks of ENSO in Pacific. This is attributed to ENSO-induced-surface heat flux anomalies, in particular incoming shortwave radiation and latent heat flux. During El Niño, ENSO-induced easterly wind anomaly in EIO generates Ekman pumping that cools the SST there. In the southeastern Indian Ocean (SEIO), ENSO-induced wind stress curl anomaly generates westward downwelling Rossby waves. Figure 1.10 displays the eastward Rossby waves deepen the thermocline and warm the SST, accompanied by high precipitation anomaly in the southwestern Indian Ocean about one season after ENSO peaks (Xie et al., 2002; Rao and Behera, 2005; Izumo et al., 2008).

1.2.2.2 Indian Ocean Dipole (IOD)

Indian Ocean dipole is well-known phenomenon in Indian Ocean, an Atmosphere-Ocean coupling phenomenon indicated by cool SST anomaly in eastern part of Indian Ocean and warm SST anomaly in western Indian Ocean (Saji et al., 1999; Webster et al., 1999). These SST anomalies are accompanied by anomalous zonal wind precipitation. IOD is phase locked with the boreal summer and fall seasons. Positive (negative) IOD is characterized by cool (warm) SST anomalies off Java and Sumatra and warm (cool) SST anomalies in western part of Indian Ocean. Positive IOD event usually brings heavy rainfall in eastern Africa and drought in Indonesia (Qu et al., 2005). The SST anomalies are accompanied with thermocline and surface wind anomalies. Positive (negative) phase of IOD is associated with deep (shallow) thermocline in WIO (EIO) and strong (weak) southeasterly winds in EIO (Figure 1.11 and 1.12). IOD is seasonally phase locked which usually develops in June and reaches its peaks in October (Saji et al., 1999).

The climatological winds in SEIO are southeasterly from April to October, which peaks in boreal summer monsoon. The southeasterly winds induce upwelling and shoaling of thermocline along Sumatra-Java coast. It cools the SST in EIO through Bjerkness feedback. Then the positive Bjerkness feedback continues, the cool SST anomalies further enhanced the easterly wind anomalies, inducing upwelling and shoaling the thermocline. In early boreal winter, the northwest monsoon wind weakens the southeasterly wind (Tokinaga and Tanimoto, 2004). As a result, the upwelling and evaporation are suppressed and terminates the IOD.

The importance of ocean dynamics in development and termination of IOD involves propagation of Kelvin and Rossby waves. The easterly anomalous wind generates off-equatorial Rossby waves that travel westward which deepens the thermocline and warms the SST in the WIO (Webster et al., 1999; Feng and Meyers, 2003). This is typical of positive IOD phase, where positive (negative) SST anomalies present in WIO (EIO). The westward downwelling Rossby waves are reflected as downwelling eastward Kelvin waves that terminate the positive IOD by deepening the thermocline in EIO. This condition is also the preconditioning of negative IOD phase in the following years (Rao et al., 2002; Feng and Meyers, 2003).

There is a controversy whether IOD is an independent phenomenon or initiated by ENSO. In some years the IOD presents during development phase of ENSO e.g. 1997, yet the IOD also presents during weak ENSO year in 1994 and non-ENSO year in in 1961 (Saji and Yamagata, 2003; Meyers et al., 2007; Schott et al., 2009). Shinoda et al. (2004) showed independent-IOD could be attributed to subsurface variability while ENSO-dependent-IOD is more caused by surface heat flux variations. In general, IOD could be initiated by ENSO or by internal variability in Indian Ocean independent to ENSO (Schott et al., 2009).

1.3 Coupled general circulation models

Coupled general circulation models (CGCMs) (Figure 1.13) are advance tool to represent the physical process in the atmosphere, ocean, cryosphere and land surface and to simulate the response of global climate system to the increase of greenhouse gas concentration (http://www.ipcc-data.org/). CGCMs are based on governing equation namely conservation laws of physics, which represent the continuous fields of temperature, pressure, velocity etc. in the atmosphere and the ocean. These continuous

fields are approximated by finite number of discrete values by discretization. The discretization divides the fluid into a number of grid cells and approximates the continuous fields by the average value or the value at the center of the grid cell. There are many techniques to discretize the equation of motion of a continuous fluid i.e. spectral method, finite-differences, and finite element.

CGCMs treat the continuous fields explicitly by transport and force among the grid cells. However, explicit approach cannot be utilized to represent physical processes smaller than grid cell. In CGCMs, this smaller-scale problem is solved through parameterization. The convective and radiative are local which depend only on the column, not on horizontally adjacent column grids. Convective and radiative processes are sub-grid scale process considered as challenging works and considered as source of uncertainty in climate simulation. Cloud feedback is also one of challenging problem to represent in CGCMs for three reasons (Neelin, 2011). First, clouds are small-scale motions compared with the grid size of climate models. Their average effects at the grid size must be parameterized. Second, clouds have opposing effects in infrared and solar contributions to the energy budget. Third, cloud properties affect radiative process i.e. cloud fraction, cloud height, cloud depth and cloud water and ice content.

1.4 Coupled Model Intercomparison Project

The objective of the Coupled Model Intercomparison Project (CMIP) is to better understand past, present and future climate changes arising from natural, unforced variability or in response to changes in radiative forcing in a multi-model context (www.wcrp-climate.org). This project includes assessments of model performance for historical future projections, an idealized experiment to understand responses of model, investigating the predictability of the climate system on various time and spatial scales. CMIP provide the multi-model output publically available in a standardized format. CMIP began in 1995, supervised by Working Group on Coupled Modelling (WGCM). It begun with experiment by comparing the model response to an idealized forcing - a constant rate of increase which was accomplished using a CO2 increase of 1% per year compounded. Later on, the experiments are forced with estimates of the changes in the historical radiative forcings as well as estimates of the future changes.

Recent CMIP experiment called CMIP phase five (CMIP5) was designed to advance our knowledge in climate variability and climate change. The CMIP5

experiment design focuses on two-time scales: one, the long-term, spanning from the mid-nineteenth century through the twenty-first century and beyond, the nearer term out to 2035. The long-term experiments include historical runs, which cover much of the industrial period, sometimes referred to as "twentieth century" simulations (Taylor et al., 2012). Within the core set of runs, there are also two future projection simulations forced with specified concentrations (referred to as "representative concentration pathways" (RCPs)), consistent with a high emissions scenario (RCP8.5) and a midrange mitigation emissions scenario (RCP4.5). The near-term decadal prediction experiments are addition to CMIP, initialized from observed states of the climate system to explore climate predictability and prediction on decadal to multidecadal time scales. The near-term predictive skill will not only depend on the skill of the models but also on model initialization method and the quality and coverage of the ocean observations.

Figure 1.14 displays schematic summary of CMIP5 long-term experiments with tier 1 and tier 2 experiments organized around central of the core. The core experiments (located in the innermost circle and shaded pink in Figure 1.14) are critical for evaluating the models, and they provide high-interest information about future climate change and aim to identify the reasons for differences in the projections. The tier 1 integrations (surrounding the core and shaded yellow) examine specific aspects of climate model forcing, response, and processes, and tier 2 integrations (shaded green) go deeper into those aspects (Taylor et al., 2012). Thus, proceeding from core to tier 1 to tier 2 can be seen as a progression from basic to more specialized simulations, exploring multiple aspects of climate system projections and responses.

1.4.1 CMIP models bias

Recently, the state-of-the-art of CGCMs models still show systematic biases, (bias is defined as deviation from the observation) that cause uncertainty and is a challenge on reliability of climate prediction. In coupled model simulation, the bias can be propagated since the atmosphere and ocean are closely coupled. The bias can be strengthened or weakened through climate feedback i.e. Bjerkness feedback (Cai et al., 2013), shortwave-SST feedback (Llyold et al., 2009; Belenger et al., 2014) and wind-evaporation feedback (Liu et al.,2011 and 2013). This subchapter will briefly discuss previous study about bias in CMIP models starting from global bias in ENSO

simulation over equatorial Pacific and bias over Indian Ocean. Thereafter, we focus on bias in summer monsoon over tropical Indian Ocean.

The major cause of biases is misinterpretation of physical process, which is amplified by feedbacks among climate components, especially in the tropics (Wang et al., 2014). Much effort has gone into improving better representation of physical process. Wang et al. (2014) documented CMIP5 models show biases that is independent of the season, but the bias of amplitude can vary with season i.e. cool SST bias in the Northern Hemisphere, in the equatorial and tropical southwestern Pacific. Warm SST bias tropical southeastern Pacific and Atlantic.

Li and Xie (2012) generalized the SST bias in CMIP5 models that can be classified into two types (Figure 1.15). First, SST bias with broad meridional structure and of the same sign across all basins that is highly correlated with the tropical mean which is ascribed to bias in representation of cloud cover; model with greater total cloud fraction has cool SST bias. Second, the SST bias with large inter-model variability in the cold tongues of the equatorial Pacific and Atlantic, which is caused in diversity of models in representing thermocline depth. Models with a deep thermocline tend to simulate warm cold tongue on the equator.

In addition, evaluation of annual and seasonal wind stress in CMIP3 and CMIP5 models compared to wind stress data derived from QuickSCAT satellite and reanalysis products revealed that CMIP5 models have systematic bias in representing wind stress in equatorial regions (Lee et al., 2014). In equatorial Pacific, CMIP zonal wind stresses are too weak in the central Pacific and too strong in the western Pacific. In equatorial Indian Ocean, the wind stress is too weak, which affects west-east slope of sea surface height. Implication of wind stress bias is shown in unrealistic simulation of summer monsoon, ENSO and IOD.

1.4.2 CMIP5 bias in ENSO simulation

In equatorial Pacific, realistic simulation of cold tongue and intertropical convergence zone (ITCZ) are the main issue of CGCMs simulation in two decades. Most CGCMs experience a cool SST bias and excessive westward extension of the cold tongue (Li and Xie, 2014) that can be caused by negative bias of precipitation and surface easterly wind biases in the western half of the basin. These arise from the interaction with the ocean via Bjerknes feedback. Meanwhile, bias in double ITCZ can

be traced back to atmospheric model simulations of cloud during austral spring and summer. Cold tongue and ITCZ biases produce unrealistic ENSO and its teleconnection.

Detailed analysis on CMIP3 models (Lloyd et al., 2009) showed positive Bjerknes feedback and the heat flux negative feedback atmospheric components play important role in ENSO simulation. However, CMIP3 models underestimate both feedbacks, in particular the heat flux feedback due to variation of shortwave radiation feedbacks. Errors in shortwave feedbacks give rise to unrealistic simulation of ENSO amplitude. This bias is still present in the next phase of CMIP version. Bellenger et al., (2013) showed that there is only slight improvement from CMIP3 to CMIP5. Both CMIP5 and CMIP3 unrealistically simulate precipitation anomaly in central equatorial Pacific, underestimating wind-SST and shortwave-SST feedbacks.

1.4.3 CMIP5 bias in Indian Ocean

Simulation of realistic variability of Indian Ocean could be influenced by ENSO simulation and/or local phenomena that are independent to ENSO. Saji et al. (2006) investigated CMIP3 models to represent the variability in Indian Ocean. They showed that CGCMs are partially successful in simulating the rich spectrum of SST variability in the Indian Ocean. Most of models successfully capture the basinwide-warming response over Indian Ocean a few months after ENSO peaks in the Pacific. Majority of CMIP3 models succeeded in capturing IOD variability reasonably well. They highlighted that representation of realistic thermocline in the equatorial region; in particular the eastern equatorial Indian Ocean is important factor in simulating the IOD. However, ENSO's oceanic teleconnection into Indian Ocean, by coastal waves through the Indonesian archipelago and by induced Rossby waves over Southwestern Indian Ocean, are poorly simulated in CMIP3 models.

In CMIP5 models, better representation of Indian Ocean basin warming is shown. Most of models successfully reproduce downwelling oceanic Rossby waves in the southern tropical Indian Ocean that precedes the development of basin warming (Du et al., 2013). This is probably resulted from the improvement of ENSO simulation and its teleconnection (Bellenger et al., 2013). Nevertheless, Li et al., (2015b) found that common equatorial easterly wind bias in CMIP5 models causes too deep thermocline depth over Southwestern Indian Ocean (SWIO). In the observation, shallow thermocline dome in SWIO is ascribed to interaction between southeasterly

trade winds and equatorial westerly wind (Xie et al., 2002). The shallow thermocline helps to sustain ENSO induced Indian Ocean basin warming. Too deep thermocline weakens the influence of thermocline on SST (via thermocline-feedback) in SWIO. This condition causes weak Indian Ocean basin variation amplitude and reduces the predictability of Indian Ocean basin warming.

Dependencies of climate feedback to mean-state of coupled models has been reported by Liu et al. (2011). The Bjerknes and thermodynamic feedback strength in IOD simulation are related to the mean state features namely the equatorial mean of thermocline, vertical gradient of subsurface temperature, and the mean vertical upwelling velocity. Liu et al. (2011) found that half of models failed to capture positive feedback on wind-evaporation-SST feedback due to bias in both the surface wind speed and the sea-air specific humidity difference. There is improvement in the CMIP5 models (Liu et al., 2013) on realistic wind-evaporation-SST feedback. However, Bjerknes feedback is unrealistically simulated and no remarkable improvement compared to CMIP3. Cai and Cowan (2013) had reported similar findings. They highlighted unrealistic IOD simulation in CMIP3 and CMIP5 models are mainly caused by too strong Bjerkness feedback in the equatorial Indian Ocean. Cai and Cowan (2013) highlighted that too strong Bjerkness feedback is attributed to: 1) unrealistic west-east thermocline slope tilted toward EIO, accompanied by 2) strong easterly wind and 3) too strong west-east SST gradient. The horizontal pattern of bias in Indian Ocean is similar to IOD SST variability during summer and autumn (Li et al., 2015a).

1.4.4 Summer monsoon bias in Indian Ocean

An IOD-like bias during boreal summer and autumn presents in tropical Indian Ocean accompanied by easterly wind bias, strong west-east SST gradient and unrealistic west-east thermocline slope tilted towards EIO (Cai and Cowan 2013, Li et al., 2015a and 2015b). Li et al. (2015a) found that the IOD-like bias can be traced back to weak southwest monsoon in summer (June, July and August) over the Arabian sea accompanied by insufficient summer precipitation in South Asian regions. Weak southwesterly monsoon wind in multi model ensemble mean (MME) of CMIP5 models generates warm SST and positive precipitation bias in WIO (Figure 1.16). These biases are strengthened and maintained by Bjerknes feedback which then develops to IOD-like bias with strong easterly wind bias, accompanied by warm (cool) SST and

positive (negative) precipitation bias in WIO (EIO) until boreal autumn. More detailed analysis by utilizing ocean heat budget over WIO (Yang et al., 2015) highlighted that warm SST bias, which forms IOD-like bias, develops during June-November. Warm SST bias in WIO significantly increases precipitation over eastern Africa, which can be attributed to unrealistic west-east gradient of thermocline. IOD-like bias is accompanied with dry Indian summer monsoon. This indicates weak summer monsoon circulation, which suppressed upwelling and evaporation cooling over WIO. This in turn maintains the warm SST bias in WIO. Ocean heat budget analysis (Yang et al., 2015) shows that the differences between surface heat flux between CMIP5 and Atmospheric Model Intercomparison Project (AMIP) simulation from single model cannot explain the cause of warm SST bias. The possible cause is attributed to insufficient cooling by ocean component of coupled models and latent heat flux. The anomalous atmospheric forcing is more considered as part of feedback rather than the cause of SST bias.

1.5 Problem statement and motivation

Previous studies suggested that IOD-like biases represented in strong horizontal SST gradient, unrealistic west-east thermocline slope and easterly over the WIO can be linked to a weaker southwesterly summer monsoon (Levine et al., 2013; Li et al., 2015a). Weakened southwest monsoon circulation generates warm SST bias in WIO which then strengthened by Bjerkness feedback hence the bias can sustain until boreal fall and develops become IOD-like bias. Yang et al. (2015) argued that insufficient ocean dynamical cooling and latent heat flux is more responsible for warm bias in summer and boreal autumn. This important finding showed that unrealistic simulation of ocean component of CMIP5 models could cause bias propagation to atmospheric bias. However, how the ocean advection process initiates the IOD-like bias remains unclear.

The first motivation of the dissertation is to reveal the role of ocean advection in ocean reanalysis models as proxy of observation. This preliminary analysis is important in order to obtain general description of ocean advection process before we continue to investigate advection role in initiating warm SST bias in CMIP5 models. The second motivation is to reveal the role of ocean process in CMIP5 models in initiating the warm SST bias in WIO. This problem remains unclear and, hence, the

novelty of the dissertation is stressed on the second motivation. This study will reveal that ocean advection plays important role in initiating SST bias in WIO.

1.6 Research Objective and Scopes

The objective of this study is to answers following questions:

- The role of ocean advection in ocean reanalysis models in initiating SST anomaly over WIO during weak-strong southwest monsoon can be revealed. This is considered as initial information prior to CMIP5 bias analysis.
- To investigate how ocean advection is represented and to reveal how the ocean advection initiate SST bias during summer over WIO in CMIP5 models.

We limit our area investigation over tropical Indian Ocean on 40-110°E and -30-30°N focusing on western Indian Ocean 40-70°E and 20°S-20°N. The period for ocean reanalysis models and CMIP5 models are 1982-2012 (31 years) and 1985-2004 (20 years) respectively. The evaluation of ocean reanalysis models will be performed in boreal summer monsoon.

1.7 Research Contribution

The result of this study gives important knowledge on ocean dynamics role in the WIO. Our results will show the importance of ocean current in forming summer development of SST bias in WIO in CMIP5 models.

1.8 Organization of Thesis

The thesis is organized as follows. The first chapter describes background, motivation, objectivity and contribution of study. The second chapter describes the data and methodology used in the thesis. The third chapter discuss about the role of advection on SST anomaly in boreal summer over WIO in ocean reanalysis models. The fourth chapter evaluates the role of ocean advection of CMIP5 models on SST bias in WIO. The fifth chapter concludes this study.

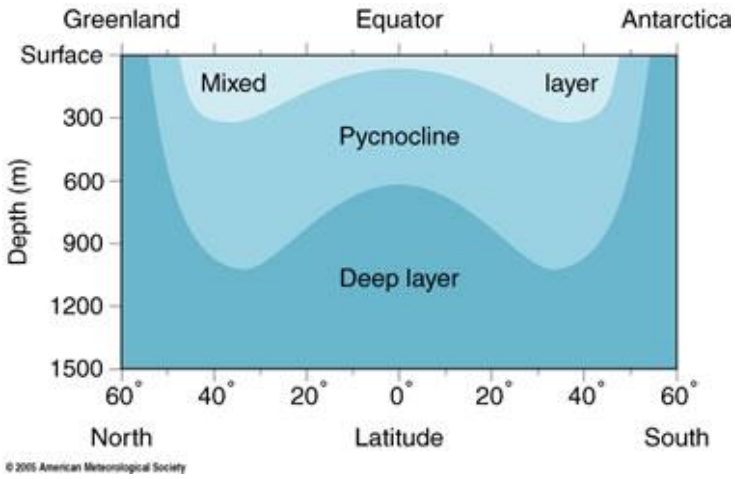

Figure 1.1. The latitude and depth plot for vertical structure of ocean (from http://oceanmotion.org/html/background/ocean-vertical-structure.htm.

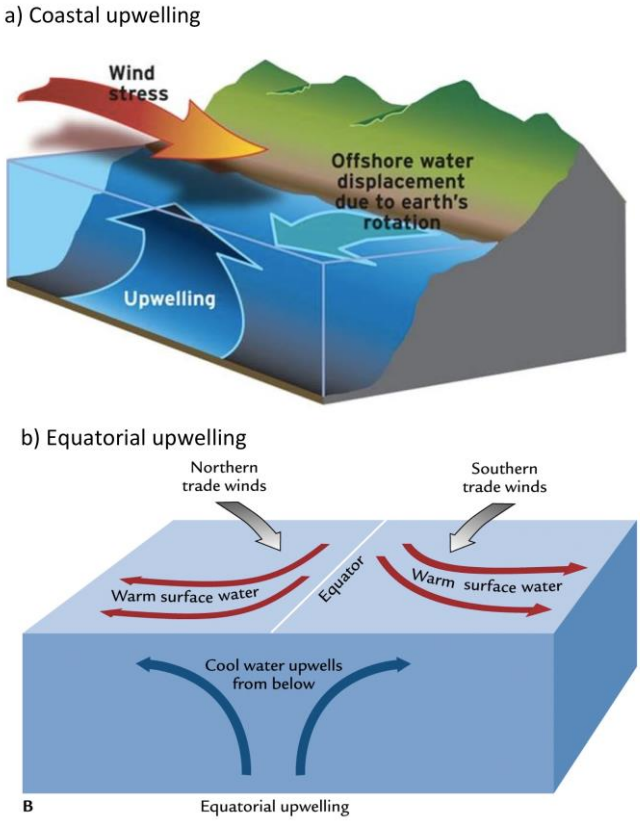

Figure 1.2 Schematic of a) coastal and b) equatorial upwelling mechanism (from https://www.nwfsc.noaa.gov/research/divisions/fe/estuarine/oeip/db-coastal-upwelling-index.cfm and http://web.sonoma.edu/users/f/freidel/global/372lec2images.htm respectively).

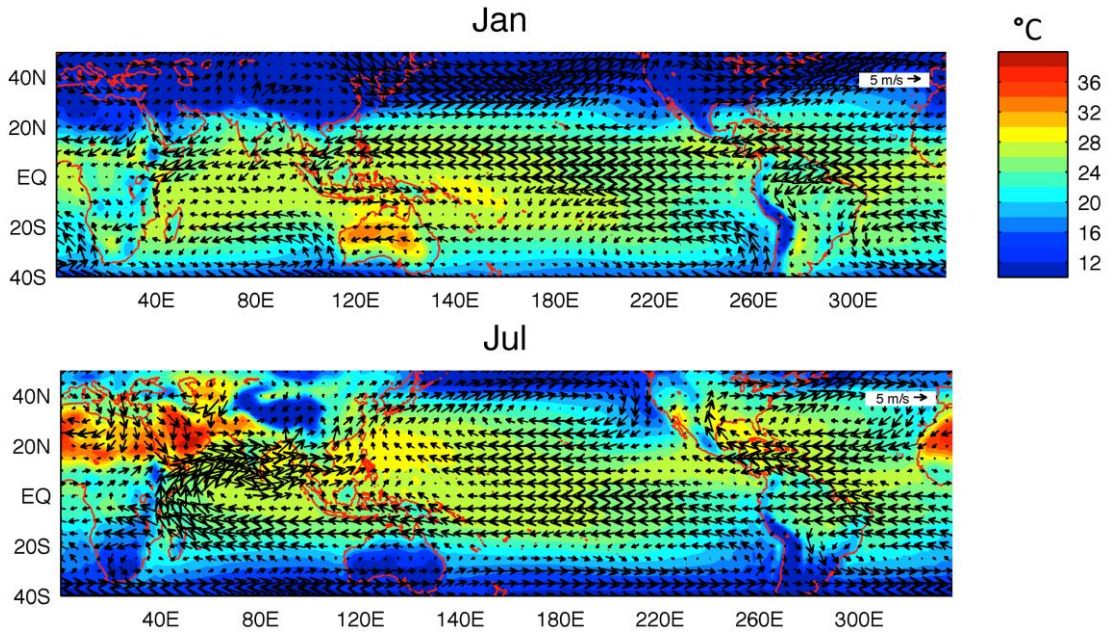

Figure 1.3 Climatology of surface temperature (°C, shaded) and wind (m s^{-1}) at 850 hPa for January and July. Surface temperature and wind data (Kalnay et al., 1996) obtained from NCEP Reanalysis data provided by the NOAA/OAR/ESRL PSD, Boulder, Colorado, USA, from their Web site at https://www.esrl.noaa.gov/psd/.

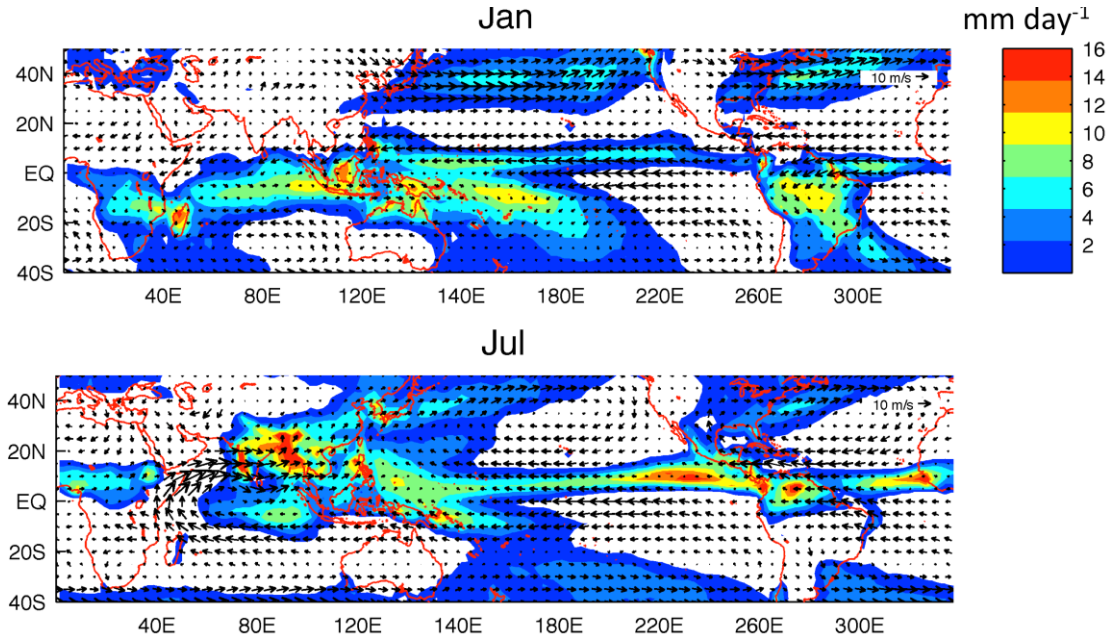

Figure 1.4 Climatology of precipitation (mm day^{-1}, shaded) and wind (m s^{-1}) at 850 hPa for January and July. GPCP precipitation data (Adler et al., 2003) and wind data (Kalnay et al., 1996) obtained from NCEP Reanalysis data provided by the NOAA/OAR/ESRL PSD, Boulder, Colorado, USA, from their Web site at https://www.esrl.noaa.gov/psd/.

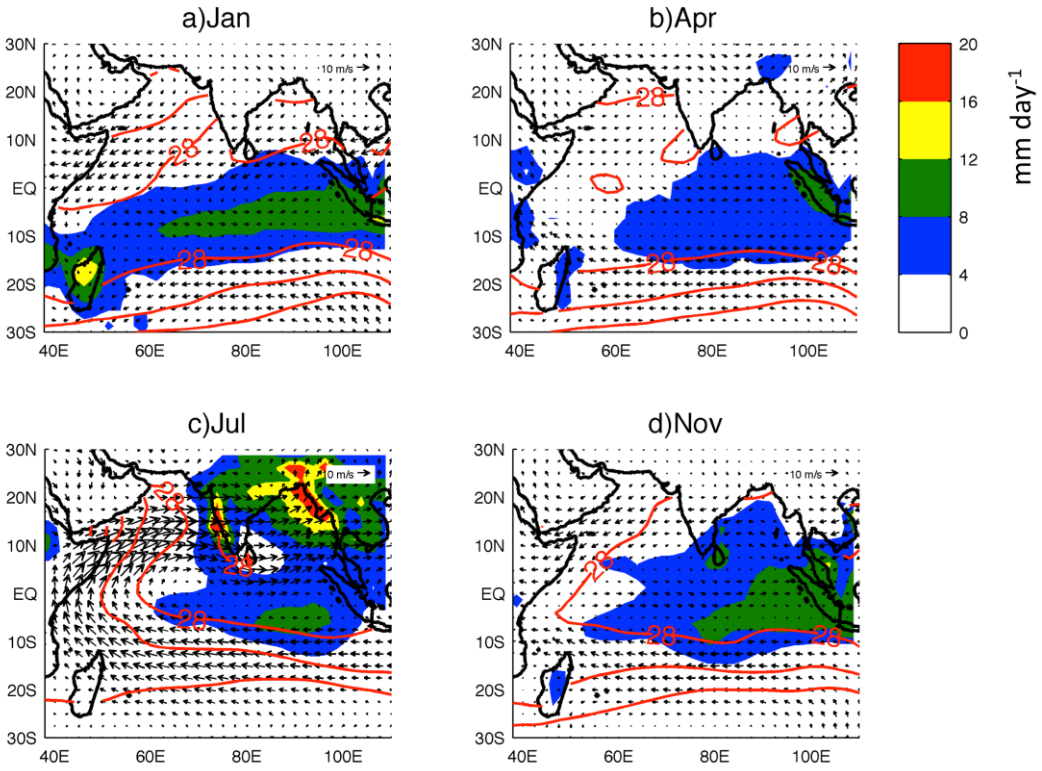

Figure 1.5 Climatology of precipitation (mm day^{-1}, shaded), SST (°C, red line contour), and wind at 850 hPa (m s^{-1}, vectors) for a) January, b) April, c) July and d) November. GPCP precipitation data (Adler et al., 2003), NOAA Extended Reconstructed SST V5 data (Huang et al., 2017) and wind data (Kalnay et al., 1996) provided by the NOAA/OAR/ESRL PSD, Boulder, Colorado, USA, from their Web site at https://www.esrl.noaa.gov/psd/.

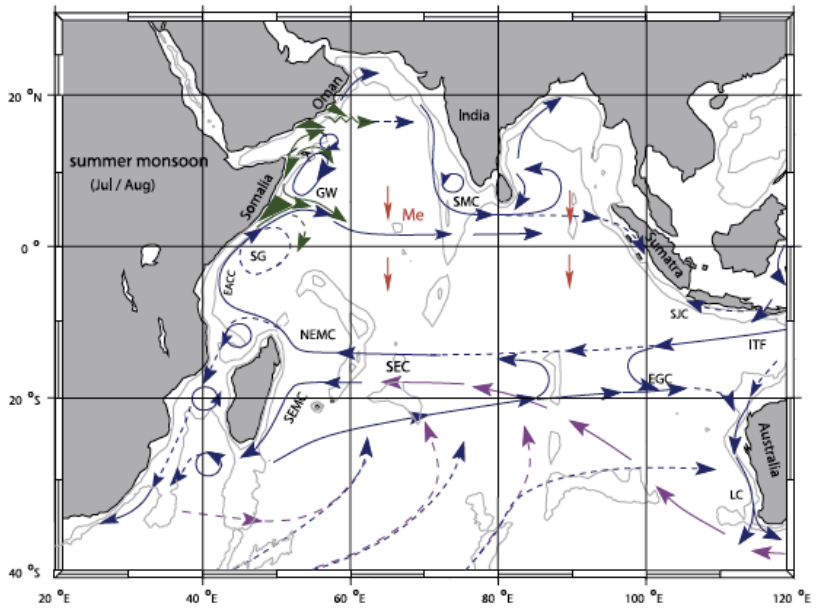

Figure 1.6 Schematic representation of identified current branches during the summer (southwest) monsoon (From Schott et al., 2009). Current branches indicated are the South Equatorial Current (SEC), South Equatorial Countercurrent (SECC), Northeast and Southeast Madagascar Current (NEMC and SEMC), East African Coastal Current (EACC), Somali Current (SC), Southern Gyre (SG) and Great Whirl (GW) and associated upwelling wedges (green shades), Southwest and Northeast Monsoon Currents (SMC and NMC), South Java Current (SJC), East Gyral Current (EGC), and Leeuwin Current (LC). The subsurface return flow of the supergyre is shown in magenta. Depth contours shown are for 1000 m and 3000 m (grey); red vectors (Me) show directions of meridional Ekman transports. ITF indicates Indonesian Throughflow.

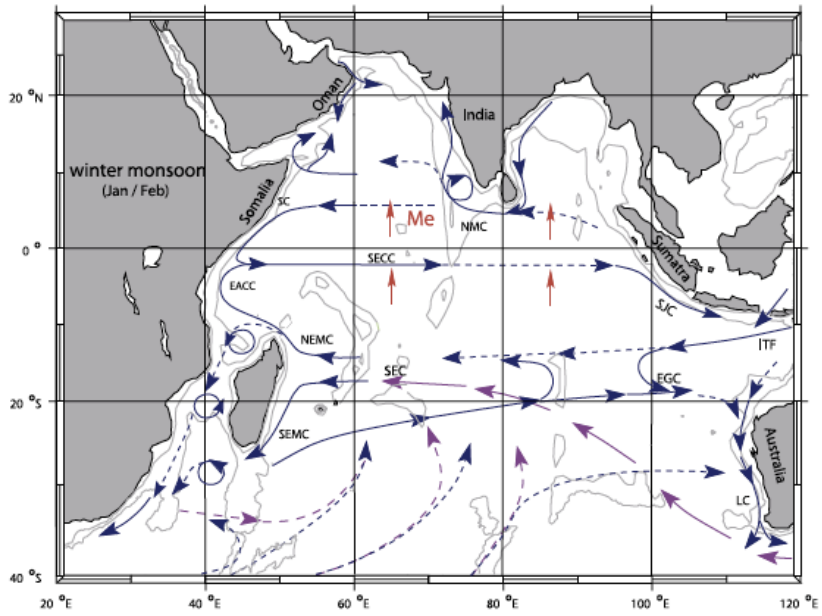

Figure 1.7 Similar to Figure 1.6 but for winter (from Schott et al., 2009).

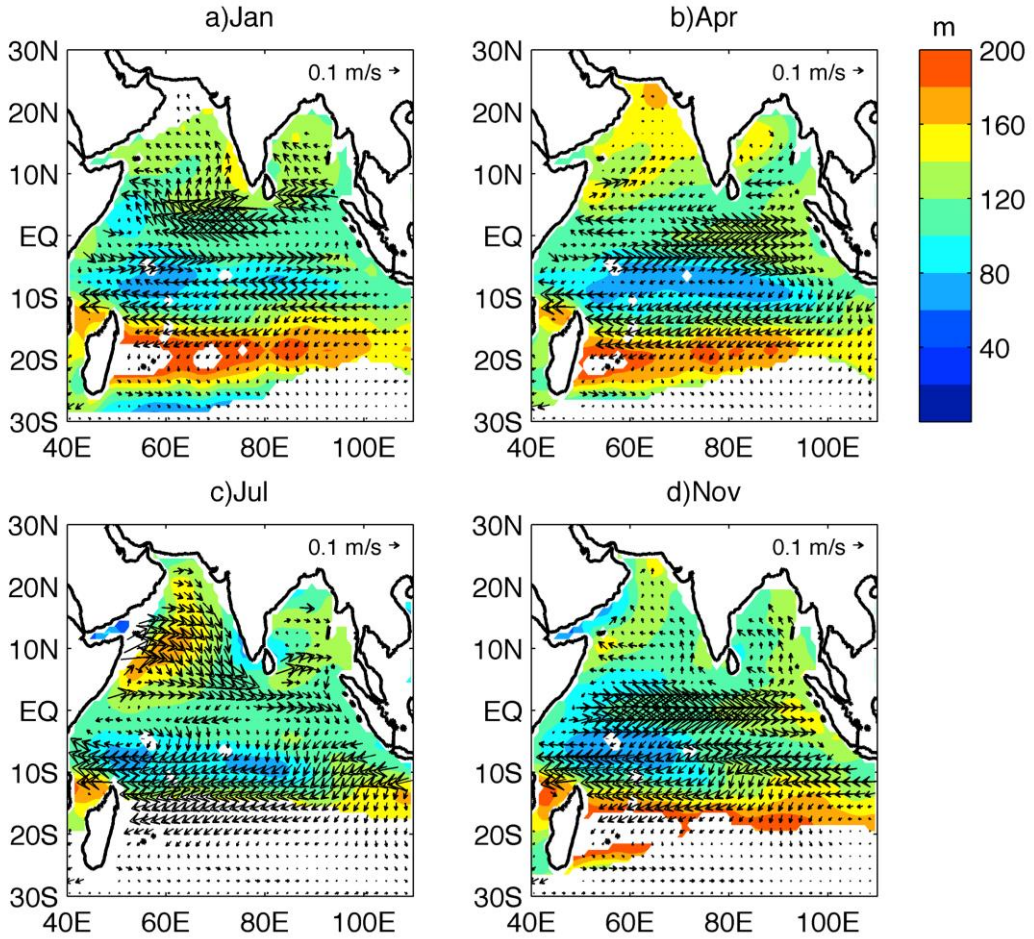

Figure 1.8 Seasonal variations of thermocline (meters, shaded) derived from ISAS13 dataset and surface ocean current (m s^{-1}) from OSCAR.

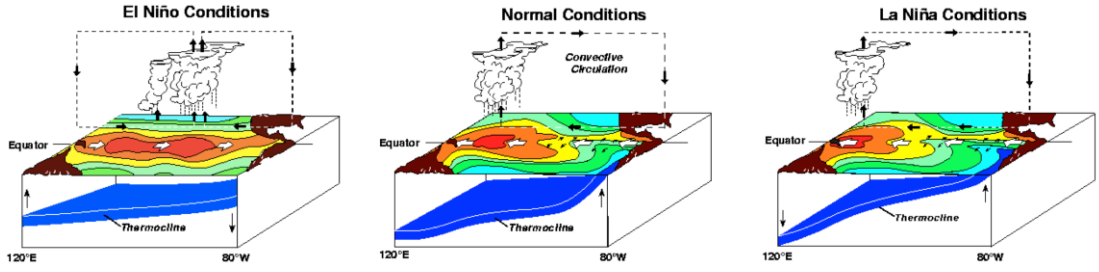

Figure 1.9 Schematic diagrams of a) El Niño, b) Normal and c) La Niña conditions (from https://www.pmel.noaa.gov/elnino/schematic-diagrams).

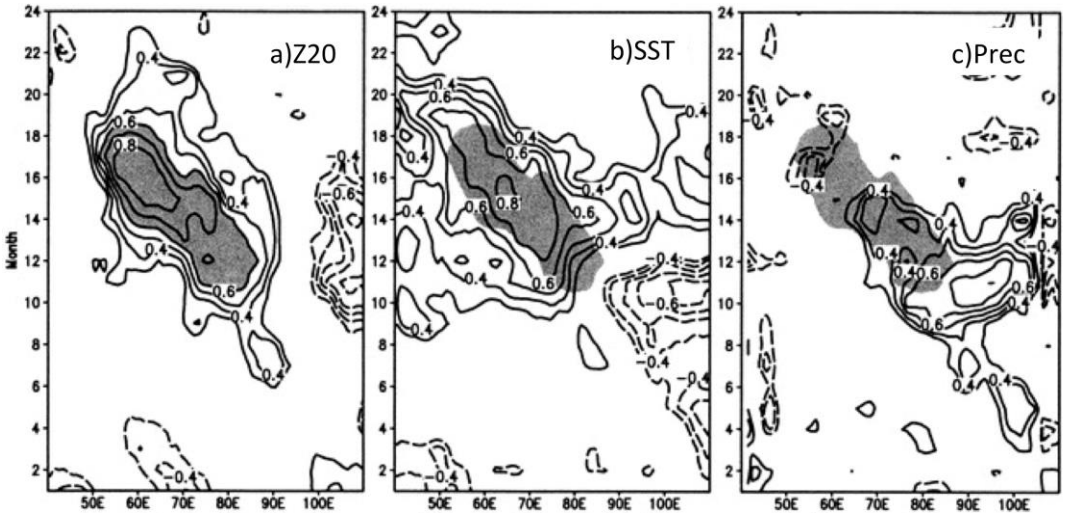

Figure 1.10 Lagged correlations of (a) depth of 20°C isothermal surface (Z20), (b) SST, and (c) Ekman pumping velocity (downward positive), averaged in 8°–12°S, with the ENSO index as a function of longitude and calendar month (From Xie et al., 2002). The *Z*20 correlation is replotted in (b) and (c) and shaded ($r > 0.6$).

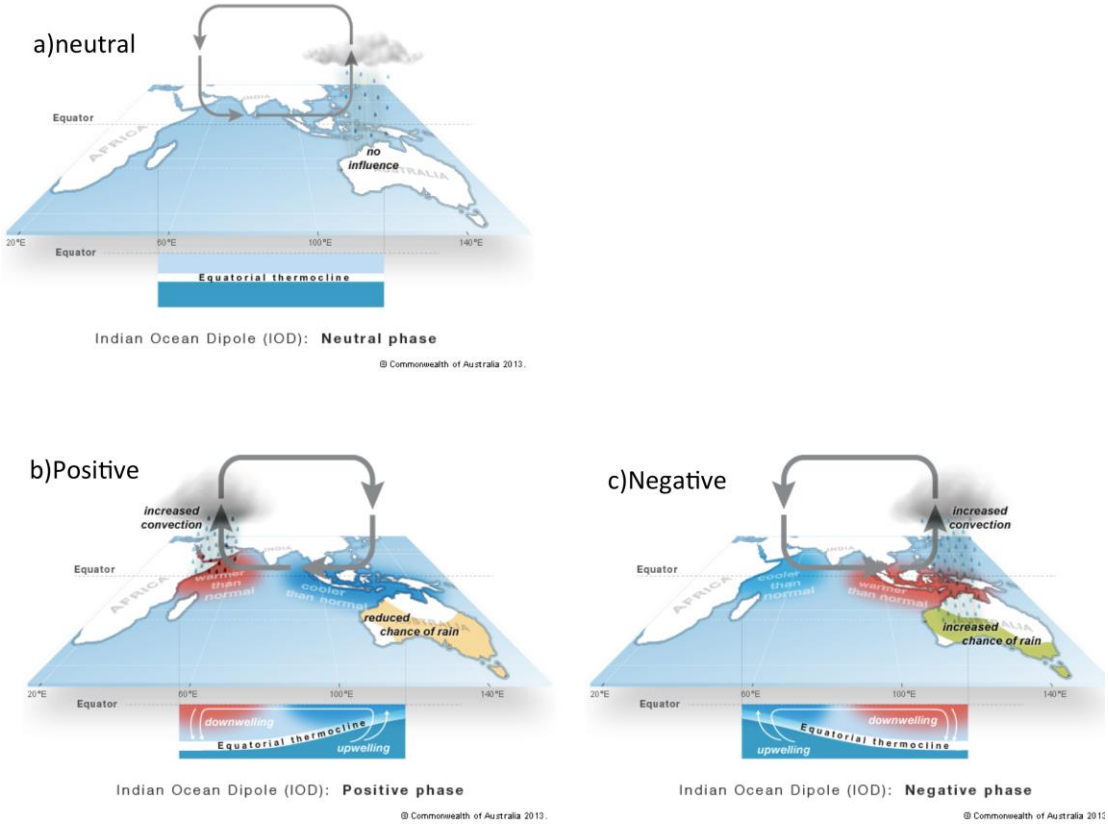

Figure 1.11 Schematic of Indian Ocean dipole for a) neutral phase, b) positive phase and c) negative phase (from http://www.bom.gov.au/climate/iod/).

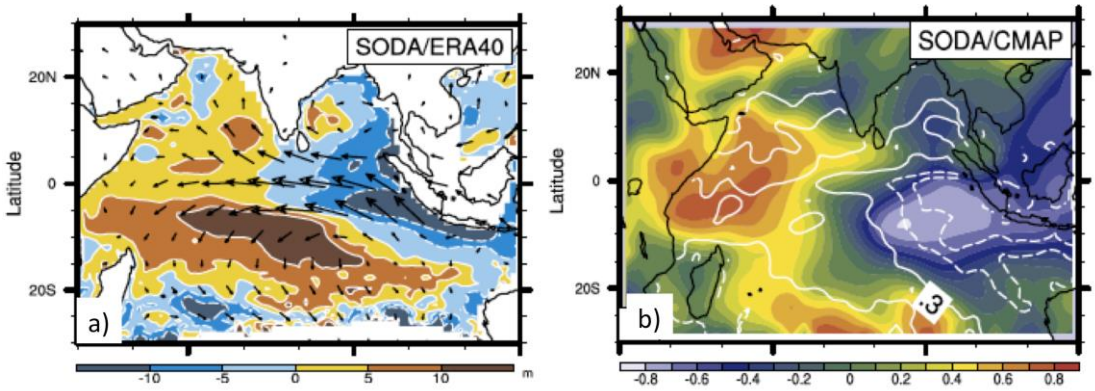

Figure 1.12 IOD pattern in September-November. a) Regression of Z20 (shaded contour) and surface wind velocity upon the first principal component of Z20 and b) correlation of precipitation (shaded contour) and SST upon the first principal component of Z20 (from Schott et al., 2009).

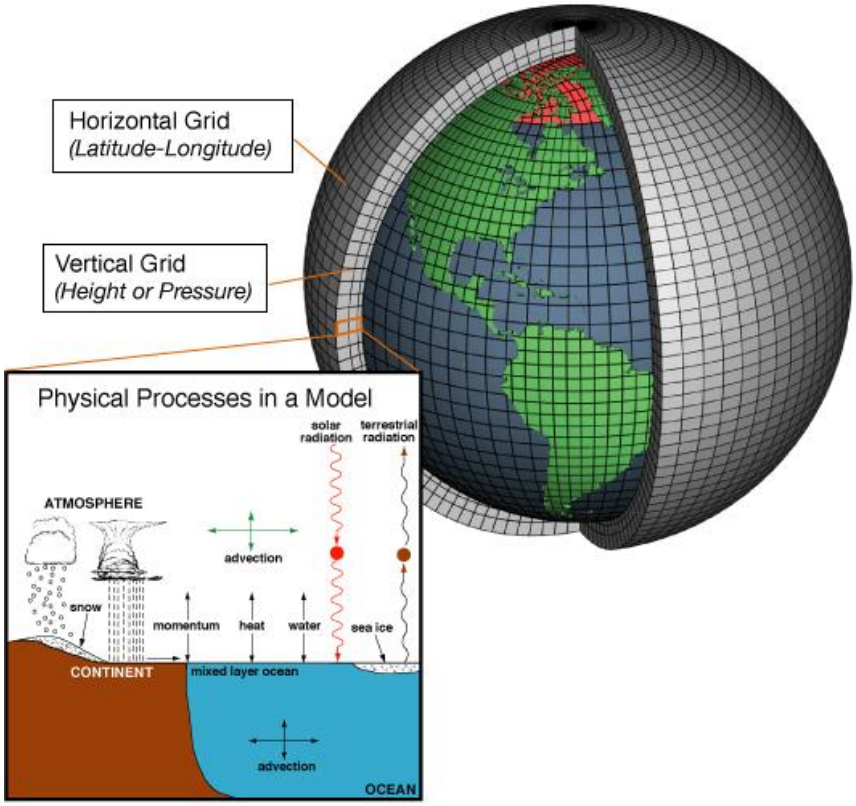

Figure 1.13 Climate models are systems of differential equations based on the basic laws of physics, fluid motion, and chemistry (from https://celebrating200years.noaa.gov/breakthroughs/climate_model/modeling_schematic.html). Scientists discretize the planet into a 3-dimensional grid, apply the basic equations, and evaluate the results. It calculates winds, heat transfer, radiation, relative humidity, and surface hydrology within each grid and evaluates interactions with neighboring points.

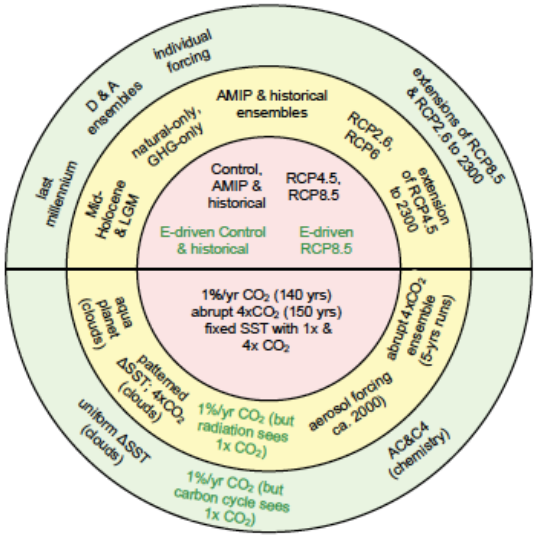

Figure 1.14 Schematic summary of CMIP5 long-term experiment with tier 1 and tier 2 experiments organized around a central core (from Taylor et al., 2012).

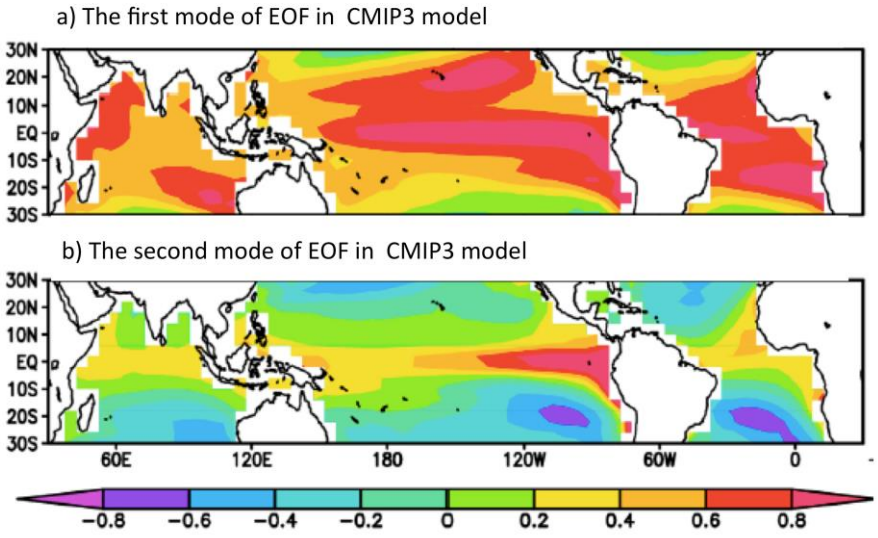

Figure 1.15 The SST bias pattern identified by Li and Xie (2012). The (a) first and (b) second inter-model EOF patterns of annual mean SST climatology over tropical oceans in 22 CMIP3 models.

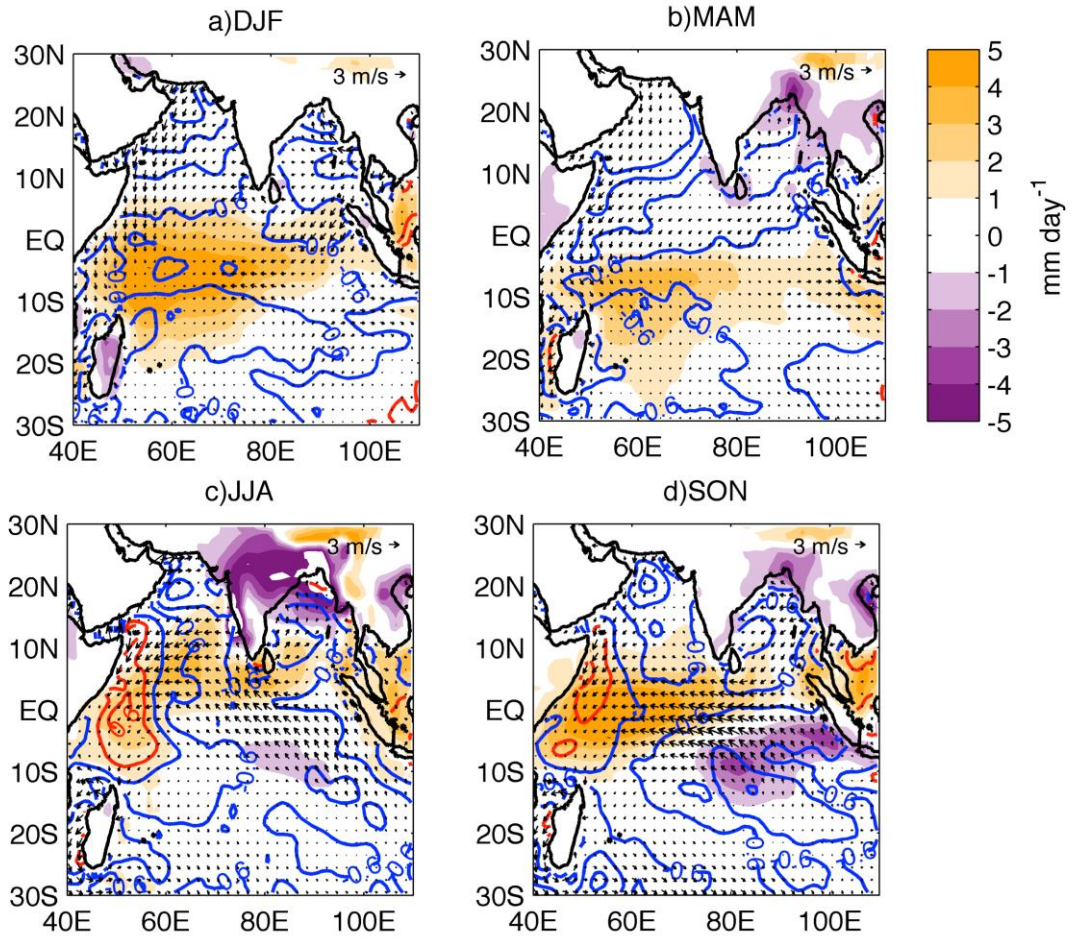

Figure 1.16 Seasonal MME CMIP5 model bias in SST (ºC, red and blue line contours), precipitation (mm day^{-1}, shaded) and surface wind (m s^{-1}, vectors). Contour interval of SST bias is 0.4 °C.

2 Data and Methods

2.1 Data for analysis of ocean reanalysis models

We utilized the monthly mean outputs from ocean reanalysis models i.e. GECCO2, SODA3, ORAS4 and GODAS, to analyze the SST anomaly in WIO. The outputs include the subsurface temperature and ocean current. The brief description of ocean reanalysis models is shown below.

2.1.1 German contribution of the Estimating the Circulation and Climate of the Ocean 2 (GECCO2)

GECCO2 ocean synthesis product is developed by the German contribution of the Estimating the Circulation and Climate of the Ocean project (GECCO, www.ecco-group.org). The adjoint method for the synthesis to adjust the initial temperature and salinity in 1948 together with the air temperature, humidity, precipitation, and zonal and meridional wind every 10 days to bring the model into consistency with the data, which is derived from the EN3v2 data base AVISO along track sea level anomalies, combination of GOCE data with complementary gravity field information (GOCO) mean dynamic topography, Hadley Centre Sea Ice and Sea Surface Temperature (HadISST), the Advanced Microwave Scanning Radiometer (AMSRE) SST, and the World Ocean Atlas 2009 (WOA09) climatology. The global model is based on the MITgcm model. The model comprises higher horizontal and vertical resolution, which consist of has 50 levels with longitudinal grid of 1 degree and varying higher resolution of meridional latitudinal grid (Kohl, 2015 and https://icdc.cen.uni-hamburg.de/1/daten/reanalysis-ocean/gecco2.html). GECCO2 uses background atmospheric from the 6 hourly NCEP/NCAR Reanalysis 1.

2.1.2 Simple Ocean Data Assimilation 3 (SODA3)

SODA Ocean model is based on Parallel Ocean Program (POP) numeric with a horizontal resolution ~0.4°x0.25° and 40 vertical levels (Carton and Giese, 2008; Giese and Ray, 2011). SODA uses 20th Century Reanalysis version 2.0 (20CRv2) dataset for

atmospheric forcing; surface wind stress is used for the surface momentum fluxes. In order to compute heat and freshwater flux, SODA uses solar radiation, specific humidity, cloud cover, 2m air temperature, and precipitation and 10 m wind speed.

2.1.3 Ocean reanalysis system 4 (ORAS4)

ORAS4 is ocean models that is developed by European Centre for Medium-Range Weather Forecasts (ECMWF) that employ ocean models to give as estimate of history and latest conditions of oceans (Balmaseda et al., 2013). Ocean initial condition for ORAS4 is forced with daily surface fluxes from ECMWF Reanalysis (ERA) of the global atmosphere and surface conditions for 45-years (ERA40) and ERA-interim reanalysis product. A variational data assimilation system for the Nucleus for European Modelling of the Ocean (NEMO) ocean model (NEMOVAR) ocean data assimilation is used to assimilate temperature and salinity profiles. The ocean model horizontal resolution is approximately 1° to 1/3° at the equator. It consists of 42 vertical levels with higher resolution near the surface from 10 m to 300 m at the bottom.

2.1.4 NCEP Global Ocean Data Assimilation System (GODAS)

The Global Ocean Data Assimilation System (GODAS) data is published by the NOAA's National Centre for Environmental System (NCEP) (Behringer and Xue, 2004). The model is based on the Modular Ocean Model version 3 (MOM3) developed at Geophysical Fluid Dynamics Laboratory (GFDL), NOAA, USA with three-dimensional variation data assimilation. This model is externally forced by momentum flux (wind forcing) estimated by satellite measurements and heat and fresh water flux obtained from NCEP–Department of Energy (DOE) Reanalysis 2. The model domain is from 75°S to 65°N and the meridional spatial resolution is 1˚ and it increases to 1/3˚ within 10˚of the equator. There are 40 vertical levels and the resolution is 10m in the upper 200m (Nishida et al., 2011).

In chapter 3, the monsoon index (Kawamura, 1998) was derived from geoptential data obtained from NCEP-DOE Reanalysis 2 dataset (Kanamitsu et al., 2002). To identify anomaly during weak and strong monsoon years (see Figure 3.5), this study used Optimum interpolation SST version 2 (OISSTv2, Reynolds et al., 2002), Climate Prediction Center (CPC) Merged Analysis of Precipitation (CMAP)

precipitation (Xie and Arkin et al., 1997) and wind data obtained from NCEP / National Center for Atmospheric Research (NCAR) reanalysis I (Kalnay et al., 1996).

For analysis of ocean reanalysis model, we used data from 1982 to 2012 (31 years). Radiation flux data that includes latent heat flux, shortwave radiation flux, longwave radiation flux, latent heat flux and sensible heat flux were obtained from NCEP/NCAR Reanalysis I (Kalnay et al., 1996). Because not all models provide surface heat flux data, as alternative we used surface radiation flux from NCEP/NCAR Reanalysis 1 for all models. NCEP Reanalysis data provided by the NOAA/OAR/ESRL PSD, Boulder, Colorado, USA, from their Web site at https://www.esrl.noaa.gov/psd/. Subsurface temperature was obtained from Research Moored Array for African-Asian-Australian Monsoon Analysis and Prediction (RAMA) (McPhaden et al., 2009), Subsurface Temperature and Salinity Analyses by Ishii et al. (2006), In Situ Data Analysis System 13 (ISAS13) (Gaillard et al., 2009, 2015 and 2016) were used for validation. For surface current, RAMA dataset and The NOAA Ocean Surface Current Analyses - Real Time (OSCAR) satellite-derived sea surface currents (Johnson et al., 2007) were used for comparison.

2.2 Data for analysis of CMIP5 models

We examined the dataset of the historical run of the CMIP5 that is referred to as the 20th century simulation or historical runs covering much of the industrial period from the mid-nineteenth century to near present (Taylor et al., 2012). Table 2.1 shows a list of the 21 CMIP5 models used in this study. Further information on each model is available online at http://www-pcmdi.llnl.gov.

In the present study, monthly mean outputs from 20-year CMIP5 simulations (1985–2004) were used, including ocean temperature and currents, atmospheric wind at the 1000-hPa pressure level as a proxy of the surface wind, precipitation, and surface heat fluxes. A similar averaging period has often been used in previous studies of the mixed layer depth (MLD) (e.g., Huang et al., 2014), which have documented that the simulated MLD shows weak decadal (and longer) variability. Therefore, this averaging period was considered sufficient for analysis of the mean seasonal cycle of SST in the tropical Indian Ocean. To calculate the MME, the outputs of the CMIP5 models were interpolated horizontally onto a 1° × 1° uniform horizontal grid, and interpolated vertically onto a 5-m uniform vertical grid (from the ocean surface down to 100 m) and

a 25-m uniform vertical grid (below 100 m), using linear interpolation. Note that the temperature at 5 m was used as the SST in the present study because the first vertical ocean level is set at nearly 5 m in most of the models.

To analyze the biases in the models, we used the ISAS13 monthly mean ocean temperature on a 0.5° grid with vertical resolution of 152 levels from 0 to 2000 m. Most of the data have been acquired by ARGO floats, which provide temperature and salinity measurements of the upper 2000 m. They have been merged with other observations such as those obtained using expendable bathythermograph, expendable conductivity–temperature–depth and conductivity–temperature–depth instruments, and moorings, averaged over the period 2004–2012. The optimal interpolation method was used to construct ocean temperature and salinity on grid-points; the estimated quantity was the anomaly in depth level relative to a reference monthly climatology. The analyzed temperature and salinity fields were obtained by adding the estimated anomaly to the reference climatology. The reference fields were based on the World Ocean Atlas 05 monthly fields interpolated on the ISAS13 grid. Near-surface winds at the 1000-hPa levels were obtained from the ERA-Interim product (Dee et al., 2011) averaged over the period 1985–2004. These data were also interpolated horizontally onto a 1° × 1° uniform horizontal grid.

2.3 Methods

2.3.1 Monsoon index

Monsoon index introduced by (Kawamura, 1998) was utilized to distinguish weak and strong monsoon during boreal summer. This monsoon index was defined as meridional differences in area-averaged upper tropospheric (200-500 hPa) thickness between Tibetan Plateau region (20-40°N) and northern Indian Ocean (0-20°N and 50-100°E) averaged in June, July and August (JJA). The positive (negative) index was considered as strong (weak) monsoon (Figure 2.1). In this study, we only considered strong-weak years whose value greater than 0.5 of standard deviations. Kawamura (1998) showed that this index correlate well with Webster and Yang's monsoon index (1992).

2.3.2 Ocean heat budget equation

In chapter 3 and 4, we examined the ocean heat budget for ocean reanalysis and CMIP5 models by using Eq (2.1). The heat budget used mixed layer temperature (MLT) over 50m as proxy of SST. The heat budget of the upper-50-m employed in this study was similar to Ng et al. (2015), i.e.:

$$\frac{\partial T}{\partial t} = -u\frac{\partial T}{\partial x} - v\frac{\partial T}{\partial y} - w\frac{\partial T}{\partial z} + \frac{Q}{\rho_0 C_p H} + \mathrm{Re}\,sidual\,, \qquad (2.1)$$

where T and u, v, and w represent the climatological monthly means of potential temperature and zonal, meridional, and vertical ocean current velocities, respectively, Q represents the surface heat flux into the ocean, H is a thickness of the water column, and C_p and ρ_0 denote the specific heat of seawater at constant pressure (set to 3994 J $kg^{-1}K^{-1}$) and a reference density of seawater (set to 1025 kg m^{-3}), respectively. All the terms were averaged over the upper 50 m in this study. In this study, fixed depth of mixed layer, 50 m depth, was utilized both in heat budget calculation for ocean reanalysis and CMIP5 models. The use of fixed mixed layer depth in CMIP5 models is intended to avoid complications associated with an MME such as variations in the MLD amongst the models (Ng et al., 2015; Fathrio et al., 2017a and 2017b*).*

Several studies have estimated the heat budget with consideration of the variation of the MLD (e.g., Kim et al., 2006). However, they often estimated the heat budget using outputs with a sampling interval shorter than a few days. Actually, Nagura et al. (2015) used outputs at three-day intervals to compute the heat budget with variable MLDs. Because the monthly mean CMIP5 model outputs were used in this study, it was difficult to estimate the exact form of heat budget. The different parameters in the short wave penetration rate below the MLD among the CMIP5 models also make it difficult to estimate the surface heat fluxes in heat budgets with variable MLDs.

2.3.3 Decomposition of ocean heat budget equation

To investigate further the role of advection on the formation of SST bias of CMIP5 models in chapter four, each variable in the heat budget was decomposed into

the MME and its deviation. The time tendency of the upper-50-m temperature deviation in each model of the MME can be written as follows:

$$\begin{aligned}\frac{\partial T'}{\partial t} = &-\left[u_M \frac{\partial T'}{\partial x} + v_M \frac{\partial T'}{\partial y} + w_M \frac{\partial T'}{\partial z}\right] \\ &-\left[u' \frac{\partial T_M}{\partial x} + v' \frac{\partial T_M}{\partial y} + w' \frac{\partial T_M}{\partial z}\right] \\ &-\left[u' \frac{\partial T'}{\partial x} + v' \frac{\partial T'}{\partial y} + w' \frac{\partial T'}{\partial z}\right] \\ &+ \frac{Q'}{\rho_0 C_p H} + \mathrm{Re}\,sidual\end{aligned} \quad , \tag{2.2}$$

, where subscript *M* denotes the MME of a quantity and the prime indicates its deviation from the MME. The first bracket represents the advection of temperature deviation by the MME currents, the second bracket is the advection of the MME temperature by the current deviation, and the third bracket is the advection of the temperature deviation by the current deviation, which is called the nonlinear dynamical heating (e.g., Ng et al., 2015).

2.3.4 Modified boundary flux formulation for advection

In order to consider the external heat source and sink controlling the formation of SST bias, the advection processes in equation (2.1) was represented in modified boundary flux formulation introduced by Lee et al. (2004). It is represented as the advection of interfacial temperature relative to the spatially averaged temperature of the domain by inflow normal to the interface. It gives a total advection of temperature that is identical to the spatial integration of local temperature advection. More importantly, it expresses external processes that control a domain's heat content (Lee et al., 2004). By considering the heat budget equation in chapter 2, the advection term becomes

$$-\nabla \cdot (\nabla T) = -\left\{u \frac{\partial T}{\partial x} + v \frac{\partial T}{\partial y} + w \frac{\partial T}{\partial z}\right\} \tag{2.3}.$$

By using Gauss theorem, volume integral of the divergence of ∇T is equal to surface integral of ∇T.

$$-\iiint_D \nabla \cdot \nabla T = -\int_S (\nabla \cdot \mathrm{n}) T dS \tag{2.4}$$

In order to quantify the effect external heat sources, Lee et al. (2004) argued that the reference temperature $\bar{T}$ should be considered calculated as volume-averaged temperature of the box.

$$-\iiint_D \nabla \cdot \nabla T = ADV = -\int_S (\nabla \cdot \mathrm{n})(T - \bar{T}) dS \tag{2.5}$$

By considering surface integral over the boundary of the box, the advection term can be written as follows.

$$\begin{aligned} \frac{\partial T}{\partial t} &= \frac{1}{V}\iint_{A_W} u(T-\bar{T})dydz - \frac{1}{V}\iint_{A_E} u(T-\bar{T})dydz \\ &+ \frac{1}{V}\iint_{A_S} v(T-\bar{T})dxdz - \frac{1}{V}\iint_{A_N} v(T-\bar{T})dxdz \ , \\ &+ \frac{1}{V}\iint_{A_B} w(T-\bar{T})dxdy + \frac{Q}{\rho_0 C_p H} + \mathrm{Re}\,sidual \end{aligned} \tag{2.6}$$

, where A_E, A_W, A_N, A_S, and A_B denote the eastern, western, northern, southern, and bottom faces of the southwestern equatorial Indian Ocean box, respectively, V is the volume of the box, and $\bar{T}$ is the volume-averaged temperature of the box:

$$\bar{T} = \frac{1}{V}\iiint T dxdydz \ . \tag{2.7}$$

Figure 2.2 displays the schematic plot for heat budget analysis for advection in terms of flux form.

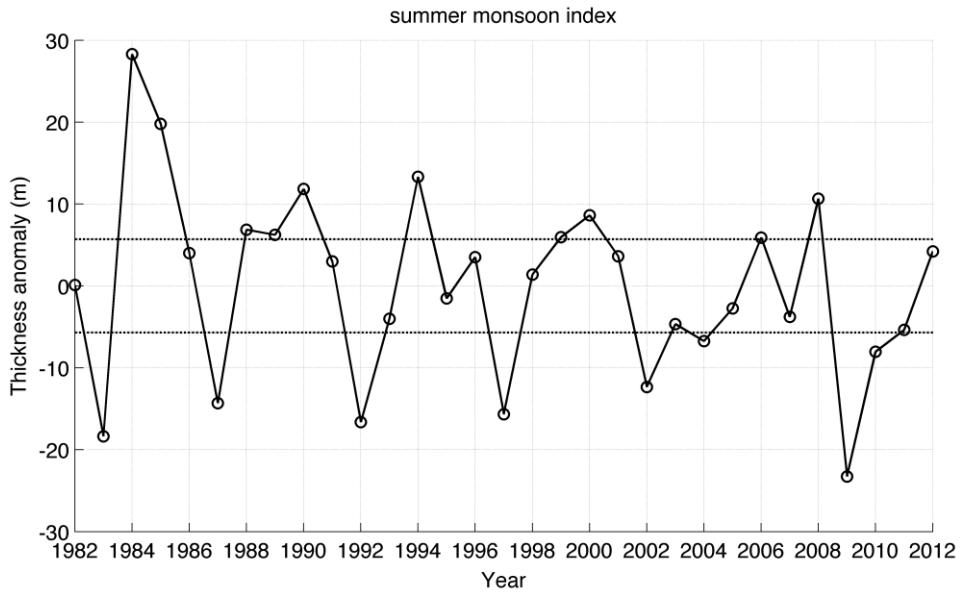

Figure 2.1 Time series of summer monsoon index (meter, bl) for JJA defined by Kawamura (1998). The dashed line shows 0.5 of standard deviation value.

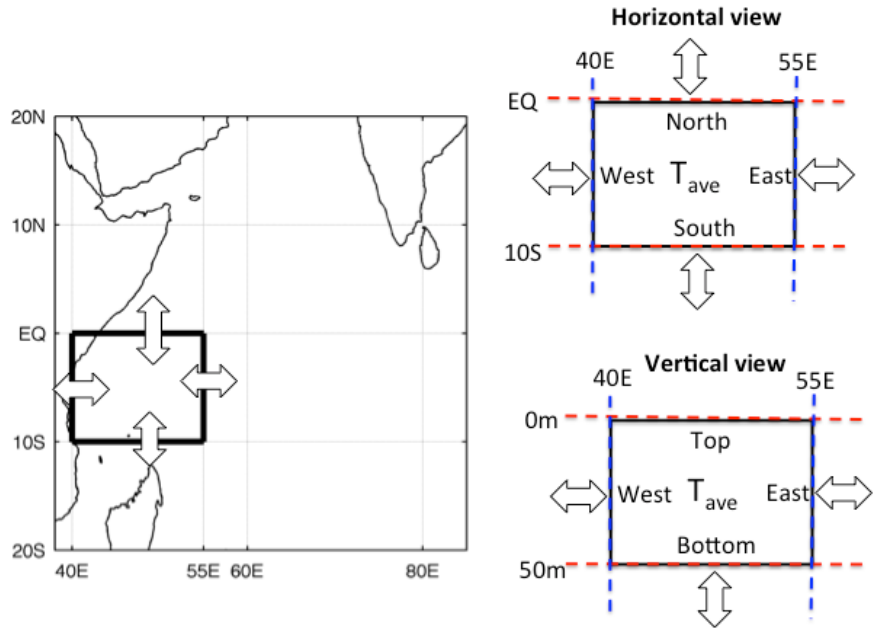

Figure 2.2 Schematic plot for heat advection in terms of flux form. The box denotes southwestern equatorial Indian Ocean (40°-55°E; 5°S-Eq).

Table 2.1 List of the 21 CMIP5 models used in this study.

Model Name	Institution	Horizontal resolution	Grids	Number of vertical ocean layer (number of layer above 100m)	Label	Reference
MRI-CGCM3	Meteorological Research Institute (Japan)	1/2°-1°	360x368	50(10)	M01	Yukimoto et al. (2012)
CMCC-CM	The Centro Euro-Mediterraneo sui Cambiamenti Climatici Climate Model (Italy)	1/2°-2°	182x149	31(10)	M02	Fogli et al. (2009)
MRI-ESM1	Meteorological Research Institute (Japan)	1/2°-1°	360x368	50(10)	M03	Yukimoto et al. (2012)
BCC-CSM1-1	The Beijing Climate Center Climate Model (China)	1/3°-1°	360x232	40(10)	M04	Xin et al. (2013)
HADGEM2-ES	Met Office Hadley Centre (UK)	1/3°-1°	360x216	40(10)	M05	HadGEM2 Development Team (2011)
IPSL-CM5B	Institut Pierre-Simon Laplace (France)	1/2°-2°	182x149	31(10)	M06	Dufresne et al.(2013)
CNRM-CM5-2	Centre National de Recherches Meteorologiques/Centre Europeen de Recherche et Formation Avancees en Calcul Scientifique (France)	1/3°-1°	362x292	42(10)	M07	Voldoire et al.(2013)
ACCESS1.3	CSIRO-BOM (Australia)	1/3°-1°	360x300	50(10)	M08	Bi et al. (2013)
CNRM-CM5	Centre National de Recherches Meteorologiques/Centre Europeen de Recherche et Formation Avancees en Calcul Scientifique (France)	1/3°-1°	362x292	42(10)	M09	Voldoire et al.(2013)
NorESM1-M	Norwegian Climate Centre (Norway)	1.125°	320x384	53(14)	M10	Bentsen et al. (2013)
GFDL-CM3	Geophysical Fluid Dynamic Laboratory (USA)	1/3°-1°	360x200	50(14)	M11	Griffies et al. (2011)
IPSL-CM5A-LR	Institut Pierre-Simon Laplace (France)	1/2°-2°	182x149	31(11)	M12	Dufresne et al.(2013)
MIROC-ESM	Atmosphere and Ocean Research Institute (The University of Tokyo), National Institute for Environmental Studies, and Japan Agency for Marine-Earth Science and Technology	1/2°-1.4°	256x192	44(13)	M13	Watanabe et al. (2011)
GISS-E2-R	NASA Goddard Institute for Space Studies (USA)	1°-1.25°	288x180	32(4)	M14	Schmidth et al. (2014)
CanESM2	Canadian Centre for Climate Modeling and Analysis (CCCMA)	0.94°-1.4°	256x192	40(9)	M15	Chylek et al. (2011)
MPI-ESM-LR	Max Planck Institute for Meteorology (Germany)	1.5°	256x220	40(9)	M16	Jungclaus et al. (2013)
GFDL-CM 2.1	Geophysical Fluid Dynamic Laboratory (USA)	1/3°-1°	360x200	50(10)	M17	Griffies et al. (2011)
MPI-ESM-P	Max Planck Institute for Meteorology (Germany)	1.5°	256x220	40(9)	M18	Jungclaus et al. (2013)
CSIRO	CSIRO Atmospheric Research (Australia)	0.9°-1.8°	192x189	31(6)	M19	Rotstayn et al. (2012)
GFDL-ESM2G	Geophysical Fluid Dynamic Laboratory (USA)	1/3°-1°	360x210	50(10)	M20	Dunne et al. (2013)
MIROC5	Atmosphere and Ocean Research Institute (The University of Tokyo), National Institute for Environmental Studies, and Japan Agency for Marine-Earth Science and Technology (Japan)	1/2°-1.4°	256x224	50(11)	M21	Watanabe et al. (2010)

3 The role of advection on SST anomaly in boreal summer over western Indian Ocean in ocean reanalysis models

3.1 Introduction

Variations of sea surface temperature (SST) in the WIO influence local weather in neighborhood countries and remote regions (Slingo et al., 2004). It was documented that increased precipitation in east of Africa in 1997-1998 countries that brings flooding in east of Africa was connected to warm SST anomaly in WIO. The SST anomaly was generated during strong positive ENSO and positive IOD phase. Later on, it was shown that IOD is more responsible for generating warm SST anomaly (Latief et al., 1999; Goddard and Graham, 1999; Behera et al., 2005).

Seasonal SST variations in the WIO display strong seasonal than other regions in Indian Ocean. SST over northern Indian Ocean reaches warmest point in boreal spring when clear sky and light wind conditions are favorable for radiation heating warms the ocean. When southwest monsoon wind established, the strong southwesterly wind, called Somali/Findlater Jet, induces the coastal upwelling in Somali-Oman coast. SST recovers during boreal autumn when the southwesterly wind retreats (Slingo et al., 2004). During winter, strong and dry northeasterly wind from the Asian continent induces cooling / latent heat loss.

There exists relation between SST anomaly in WIO and precipitation over WIO. Early numerical simulation (Shukla, 1975) found that colder SST anomalies in western Arabian Sea are responsible for reduced monsoon precipitation over Indian and adjoining areas. This is accompanied with the increase in the moisture flux convergence and precipitation over south of the equator. Izumo et al. (2008) showed there is close relation between SST anomaly near Somali-Oman and precipitation in west coast of India. They highlighted variations of ocean upwelling in boreal spring generate SST anomaly in Somali-Oman coast. Warming (cooling) of SST could increase (decreases) evaporation, which results in greater (less) moisture transport towards Indian continent. Yang et al. (2010) also reported that warm Indian Ocean basin could increase evaporative moisture that is transported to South Asia by the climatological summer monsoon, leading to a significant increase in summer monsoon precipitation

Izumo et al. (2008) argued that suppressed upwelling could be caused by weak

southwesterly monsoon wind generated by warm SST anomaly in the SWIO. Modulation of thermocline depth by ENSO is the possible candidate to initiate SST anomaly in SWIO (Xie et al., 2002; Rao and Behera 2005, Vialard et al., 2008; Izumo et al., 2008). These findings also corroborate previous studies by Kawamura (1998) that showed remote effect of El Niño (La Niña) could reduce (increase) warming over central Asia to the northwest Indian subcontinent and increase warming (cooling) in tropical Indian Ocean in late boreal spring. This condition develops weak (strong) land-sea thermal contrast between Asian continent and WIO, resulting in weak (strong) Asian summer monsoon. These results suggest the importance of SST anomaly in SWIO, which influences initiation of Indian summer monsoon.

Recent intensive ocean observation known as RAMA project over Indian Ocean supported development of ocean reanalysis models by ocean data assimilation technique. It is expected that better understanding of ocean internal process over Indian Ocean can be achieved. Previous ocean heat budget studies (Shaji et al., 2003) revealed that seasonal SST variation in WIO could be explained by variation of surface heat flux and oceanic process. However, the role of internal ocean process to initiate boreal summer SST anomalies in WIO was not fully discussed yet. Hence, this study aims to portray the ocean advection role to initiate strong-weak summer monsoon related SST anomaly over WIO.

3.2 Validation of Ocean reanalysis data

Figure 3.1 compares subsurface temperature and horizontal ocean surface current at 10m depths at RAMA buoy location in Southwestern Indian Ocean (55°E and 8°S) and central equatorial Indian Ocean (80.5°E and Eq). Unfortunately, RAMA buoys observation only cover the data after 2008. At 55°E and 8°S, all models simulate subsurface temperature that is well correlated with the observation, except GODAS showing cool bias in 2009-2011 (Figure 3.1a). Variations of zonal and meridional surface current are well represented by all models with comparable magnitudes. At the equator (Figure 3.1b), subsurface temperature and zonal current are well simulated. However, models underestimate the magnitude of meridional current in 2009-2011 at the equator. OSCAR also overestimates the magnitude of meridional current.

Semiannual variations of zonal surface current are well represented by all models (Figure 3.2). At the equator, during inter-monsoon transition (April-May and

Oct-Nov) the zonal current is eastward associated with eastward Yoshida-Wyrtki Jet, while the strongest eastward current is located in 60°-80°E. Westward current presents during boreal winter in 40°-80°E and summer in 50°-70°E. Meanwhile, the eastward current is present during summer in 40°-50°E, probably related to Ekman transport induced by southwesterly monsoon wind. Semiannual variation of thermocline is well represented by all models (Figure 3.3). Thermocline is deeper during May and September and is shallower during boreal winter and summer. ORAS4 and GODAS simulate comparable depth of thermocline, while GECCO2 and soda2 simulate deeper thermocline during boreal winter.

Spatial distribution of seasonal SST and surface current are displayed in Figure 3.4. In general, all models successfully simulate general features of seasonal variations of SST and surface current. During winter, cool SST present in Arabian Sea, while SWIO experiences warming. The northeast monsoon current at the north of equator flows westward towards the WEIO box. The Somali current to the east of Somalia coast flows southwestward. The Somali current meets northwestward flow EACC and they flow eastward as SECC to the south of equator (2°-4°S). The warmest SST presents during boreal spring (April) and there exist eastward Yoshida-Wyrtki Jet at the equator. When the southwest monsoon emerges, cool SST presents along near Somali-Oman coast due to coastal upwelling induced by southwesterly monsoon wind. Warm SST extends longitudinally in 60°-90°E at the equator. EACC flows northeastward and part of it flows northwestward as Somalia current while the other part turn eastward. During autumn, when the southwest monsoon retreats, the Arabian Sea experiences warming. The northeastward flow Somalia current weakens and the Yoshida-Wyrtki Jet again flows eastward for the second time in a year.

3.3 Results and Analysis

Monsoon index introduced by (Kawamura, 1998) was utilized to distinguish weak and strong monsoon during boreal summer. The differences between weak and strong composite of summer monsoon years in SST and surface wind are displayed in Figure 3.5. It shows that warmer SST anomaly is initiated in southern Indian Ocean, accompanied by greater precipitation. Then, the SST anomaly progresses northward to western Arabian Sea accompanied by northeasterly (northwesterly) wind anomaly in north (south) of equator. In summer (June and July), the precipitation anomaly presents

in Arabian Sea and west coast of India. Meanwhile, the center of Indian continent experiences negative anomaly of precipitation. The anomaly patterns agree well with results of Izumo et al. (2008). Based on the SST anomaly distribution in WIO, we divided WIO into three study regions, namely western Arabian Sea (WAS) (50°-65°E, 13-23°N), WEIO (45°-60°E, 10°S-10°N) and SWIO (50°-65°E, 5°-15°S).

3.3.1 Western Arabian Sea

Figure 3.6 displays climatological time series of heat budget in WAS (50°-65°E, 13°-23°N). MLT (black) experiences semiannual variations with two maxima in May-June and October-November. The former is warmer than the latter one. The maximum temperature in May-June is preceded by warmest MLT tendency (yellow) in boreal spring (March-April). The main contributor for warming in boreal spring is the surface heat flux (red), which peaks in April. Solar heat flux is maximum due to clear-sky conditions and penetrative solar radiation is also maximum during this period due to the thin mixed layer (Montegut et al., 2007).

During boreal summer, the MLT tendency becomes negative accompanied by cooling of MLT. Warming of surface heat flux is suppressed in boreal summer, probably due to evaporation cooling. Ocean process contributes to summer cooling by vertical advection (blue) through wind-induced-upwelling and zonal advection (green). Montegut et al. (2007) noted that coastal upwelling zone in WAS dominates the cooling of SST during summer. Residual term (purple) also cools the MLT from May to September. In September-October, MLT start to warm again supported by warming of surface heat flux and suppressed cooling by vertical and meridional advection. After MLT reaches the second maxima in October-November, it slowly cools until reach the minimum point in January-February. This is mainly caused by cooling of surface heat flux (Montegut et al., 2007).

Figure 3.7 displays time series difference between weak and strong summer monsoon composite. All models show that the largest positive MLT differences (black) present in July, preceded by largest positive MLT tendency differences (yellow) in May-June. To confirm this relation, scatter analysis was conducted. Figure 3.8 shows scatter plot between MLT monthly anomaly in June and MLT tendency in May displays good correlation greater than 0.5 in all models. This robust relation explains that MLT monthly anomaly in July could be initiated by variation of heat budget components in May. Weak composite (blue dots) and strong composite (red dots) can be distinguished,

except some outliers (blue dots) are caused due to unknown reason. This indicates that warm (cool) MLT anomalies in WAS tend to occur during weak (strong) summer monsoon years. Figure 3.9 displays that MLT monthly anomaly is well correlated with vertical advection, surface heat flux and zonal advection. Highest correlation is shown by vertical advection in three models, except GECCO2. Our results support Montegut et al. (2007) study. They highlighted that processes associated with upwelling regions dominate the interannual heat budget variations. The second contributor is surface heat flux shown in three models, except SODA3. Zonal advection is another possible contributor process in GECCO2 and GODAS.

3.3.2 Western Equatorial Indian Ocean

In WEIO (45°-60°E, 10°S-10°N), MLT experiences annual variations with the warmest MLT presents in April-May (Figure 3.10). The surface heat flux is the dominant cause of spring warming that peaks in March. In summer, cooling of MLT is caused by cooling of surface heat flux, vertical, zonal advection and residual term. Cooling in WEIO presents earlier than in WAS since the southwesterly monsoon wind was established first in WEIO. MLT recovers in autumn due to warming by meridional advection during June to August and surface heat flux in August to September. In contrast, vertical advection is against warming. It cools the MLT during boreal autumn.

Differences between weak and strong composite is shown in figure 3.11. All models show that peak of positive MLT difference presents in June. This is preceded by positive MLT tendency difference in May. Scatterplot shows that MLT tendency in May and MLT anomaly in June are well correlated (Figure 3.12). It suggests that the ocean process in May could contribute to initiate the MLT anomaly in June. Similar to WAS case, we can clearly distinguish weak (blue dots) and strong (red dots) summer monsoon years. This implies that warm (cool) MLT anomalies in WEIO tend to occur during weak (strong) summer monsoon condition. In WEIO, the anomaly of MLT in June is well correlated with zonal advection process in May (Figure 3.13). This relation is significant in all models. ORAS4 and GODAS showed that variation of vertical advection and meridional advection respectively could affect MLT anomaly. The zonal advection could be related to eastward transport of cold water from Omani and Somali upwelling regions (Shankar et al., 2002; Montegut et al., 2007). In addition, only GODAS that shows significant contribution of surface heat flux to MLT anomaly in

June.

3.3.3 Southwestern Indian Ocean

In Southwestern Indian Ocean (50°-65°E, 15°-5°S), MLT displays annual variations that reaches maximum around March-April (Figure 3.14). This is mainly attributed to warming by surface heat flux that occurs from October to March. In this season, radiation warming reaches maximum since the sun is located in the southern hemisphere. MLT reaches the coolest point during boreal summer, preceded by cooling of surface heat flux contribution in boreal spring to summer. The vertical advection is against the surface heat flux. It tends to cool the MLT during boreal winter to spring. The meridional advection tendency contributes to warm the MLT in the late of summer. This owes to the southward Ekman heat transport associated strong meridional SST gradient and easterly wind stress associated with the Indian summer monsoon (Yokoi et al., 2008)

Figure 3.15 displays that the largest MLT difference presents in March-April, preceded by positive MLT tendency difference in March. Figure 3.16 confirms that these two variables are well correlated. The MLT anomaly in April could be initiated by atmospheric and/or oceanic process in March. Warm (cool) MLT anomalies also tend to present during weak (strong) summer monsoon years. Figure 3.17 displays correlation between MLT anomaly in April and heat budget terms in March. Note that all models show significant contribution of vertical advection in March to initiate MLT anomaly in April, while the second contributor is surface heat flux. Our result is consistent with Yokoi et al. (2010) which found that vertical advection process is responsible for warm MLT anomaly on interannual time scale. Other possible contributor is residual term (res) that only shown in GECCO2 and SODA3.

3.4 Summary and Discussion

Our results portrayed that the vertical advections are the most important process in WAS and SWIO and the zonal advection is the dominant process in WEIO to initiate MLT anomaly during boreal summer monsoon. It is interesting to note that unlike vertical advection in other two regions, zonal advection is more dominant in WEIO.

In contrast to boreal winter, zonal advection becomes less important than the

vertical advection. Table 3.1 displays the correlation between MLT anomaly averaged in December to January and heat budget terms averaged in September to November over WEIO. It shows that vertical advection displays significant correlation in all models. It could be understood since during winter, climatologically, the thermocline is shallower than summer. As a result, the upwelling is easily affects the MLT/SST. During winter monsoon, the possible cause of thermocline variations is not only strong northeasterly wind. IOD or ENSO could modulate the thermocline variation. The strongest impact may present when the IOD and ENSO co-occurred as in 1997 case.

Ocean heat budget analysis has been applied to analyze the SST/MLT anomaly during weak-strong southwest monsoon over WIO. The analysis was applied on four ocean reanalysis models: GECCO2, SODA3, ORAS4 and GODAS. This study shows that during weak summer monsoon, the MLT anomalies tend to be warmer than usual, vice versa. In addition, it is shown that ocean process plays more important role than atmospheric process to initiate the MLT anomaly during extreme weak/strong summer monsoon conditions.

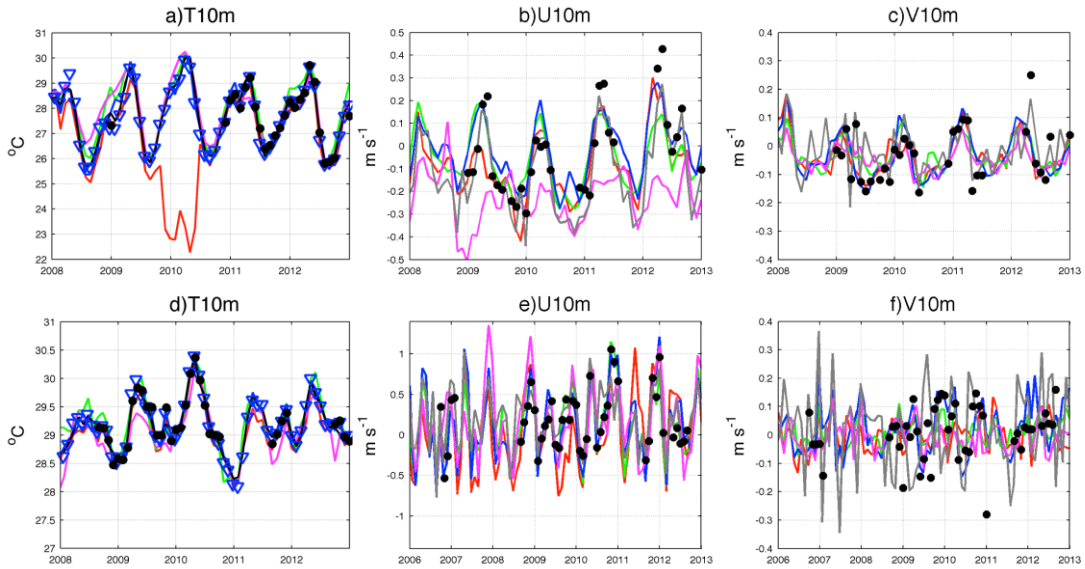

Figure 3.1 Time series for subsurface temperature (T10m in °C), zonal current (U10m in m s^{-1}) and meridional current (V10m in m s^{-1}) at 10m depths at 55°E and 8°S (a, b, and c) and 80.5°E and Eq (d, e, and f). Green, magenta, blue, and red solid lines indicate GECCO2, SODA3, ORAS4 and GODAS. For subsurface temperature, black solid line and triangle marker indicates ishii dataset and ISAS13. Black dots indicate RAMA buoy observation. Gray solid line indicates OSCAR surface current.

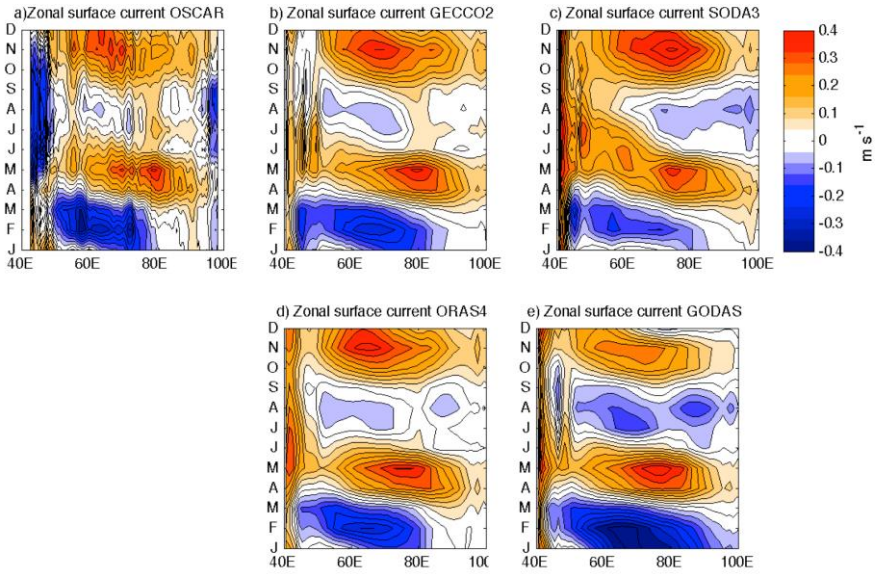

Figure 3.2 Longitude time horizontal plot for ocean surface current (m s^{-1}) averaged over 5°S-5°N for a) OSCAR, b) GECCO2, c) SODA3, c) ORAS4 and d) GODAS.

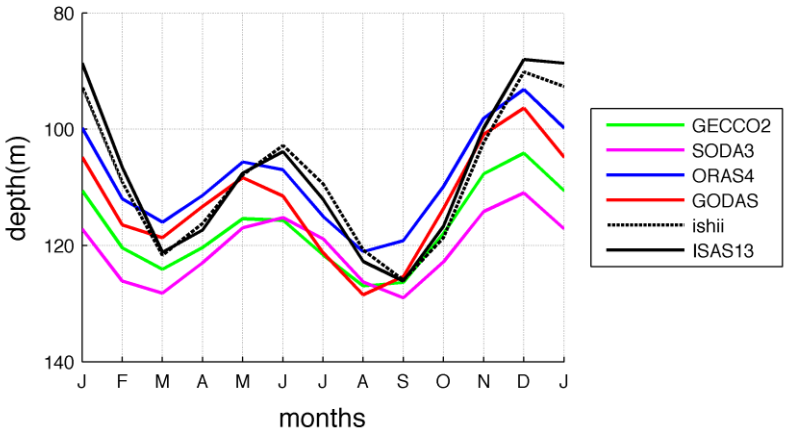

Figure 3.3 Seasonal time series of thermocline (meter) averaged over 45°-60°E and 10°S-10°N for GODAS (red), GECCO2 (green), ORAS4 (blue), SODA3 (magenta), ishii dataset (black dashed line) and ISAS13 (black solid line).

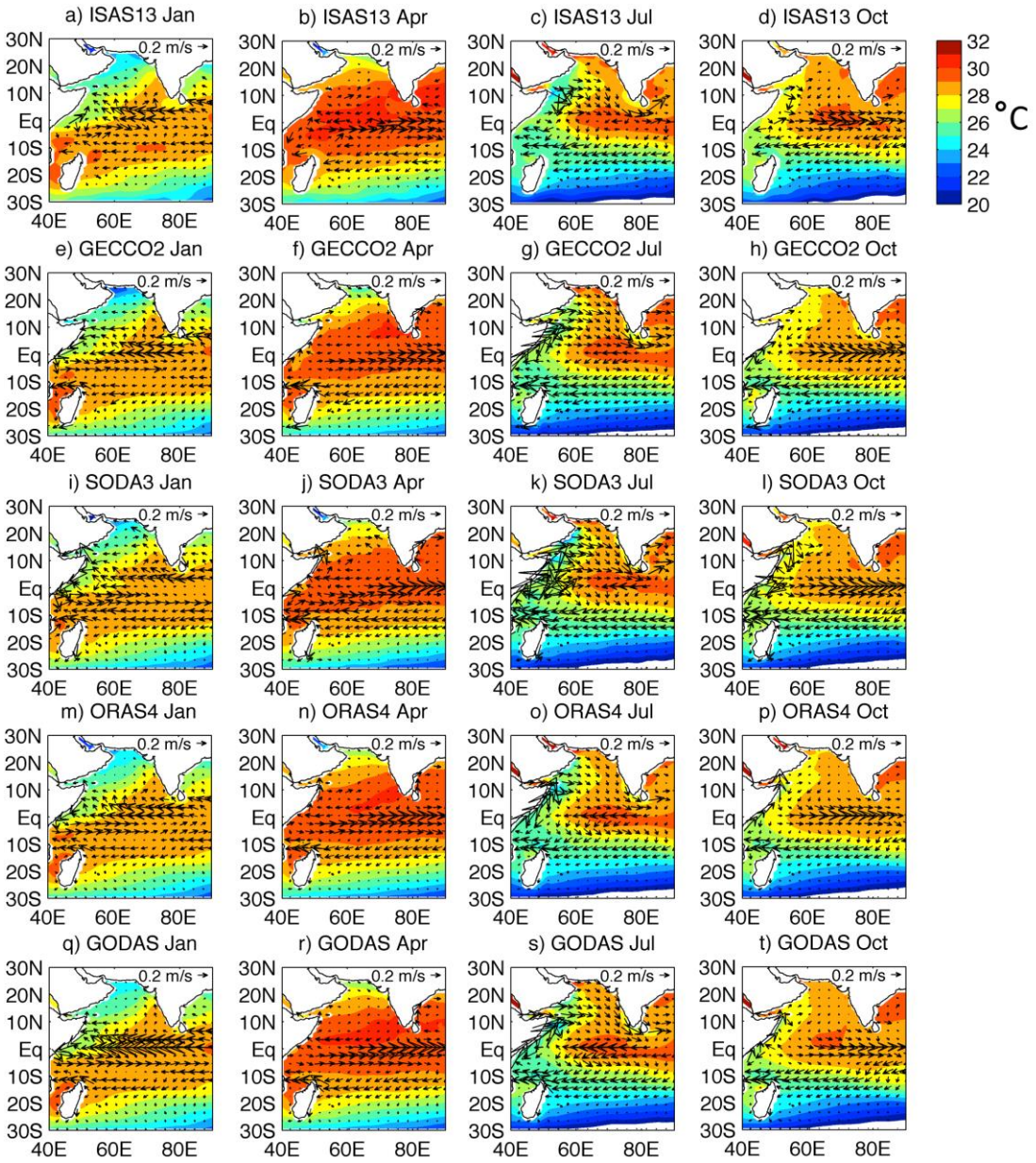

Figure 3.4 Horizontal map for seasonal SST (°C, shaded) and ocean surface current (m s^{-1}, vectors) for observation (ISAS13), GECCO2, SODA3, ORAS4 and GODAS.

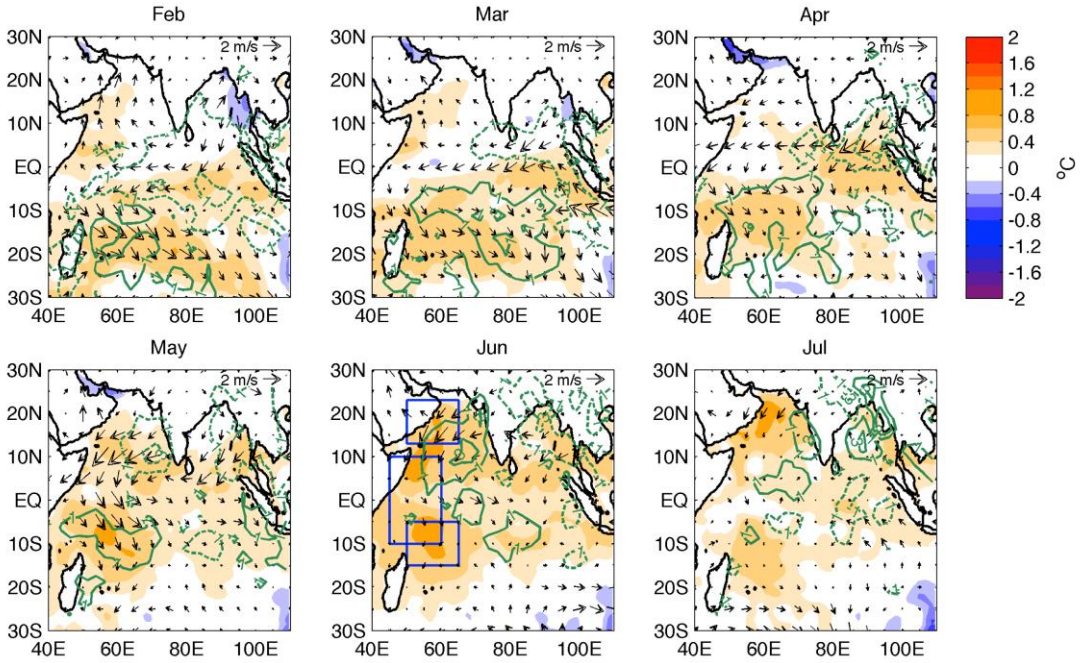

Figure 3.5 Composite of weak summer monsoon years minus composite of strong summer monsoon years for SST (°C, shaded), surface wind (m s^{-1}, vectors) and precipitation (mm day^{-1}, green contour) in February to July. Contour interval is 2 mm day^{-1}. The SST, surface wind and precipitation data were obtained from OISSTv2, NCEP NCAR Reanalysis I and CMAP dataset respectively. Blue rectangles show region of study namely, western Arabian Sea (50°-65°E, 13-23°N), western equatorial Indian Ocean (45°-60°E, 10°S-10°N) and southwestern Indian Ocean (50°-65°E, 5°-15°S).

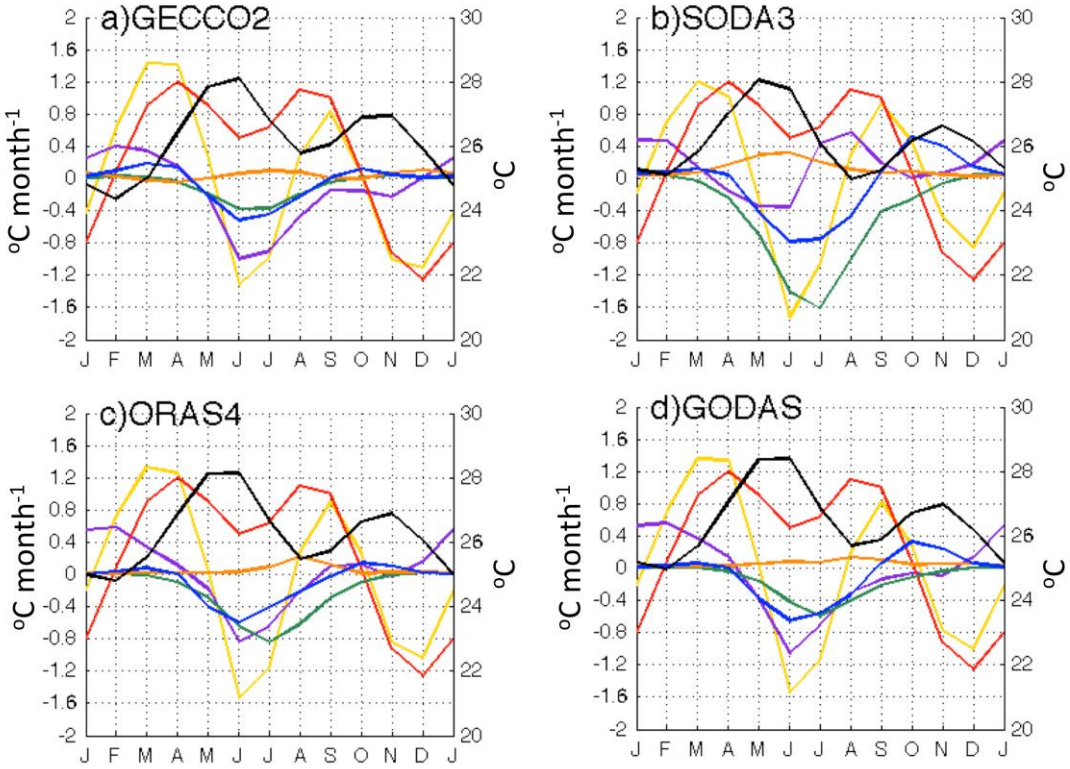

Figure 3.6 Time series of area averaged heat budget over western Arabian Sea (50°-65°E, 13°-23°N) for a) GECCO2, b) SODA3, c) ORAS4 and d) GODAS. Mixed layer temperature, mixed layer tendency, surface heat fluxes are denoted by black, yellow and red colors respectively. Vertical, zonal and meridional heat advections are denoted by blue, green and orange colors respectively. Residual term is denoted by purple color. In each panel, the left y-axis is for heat budget components (°C month^{-1}) and the right y-axis is for mixed layer temperature (°C).

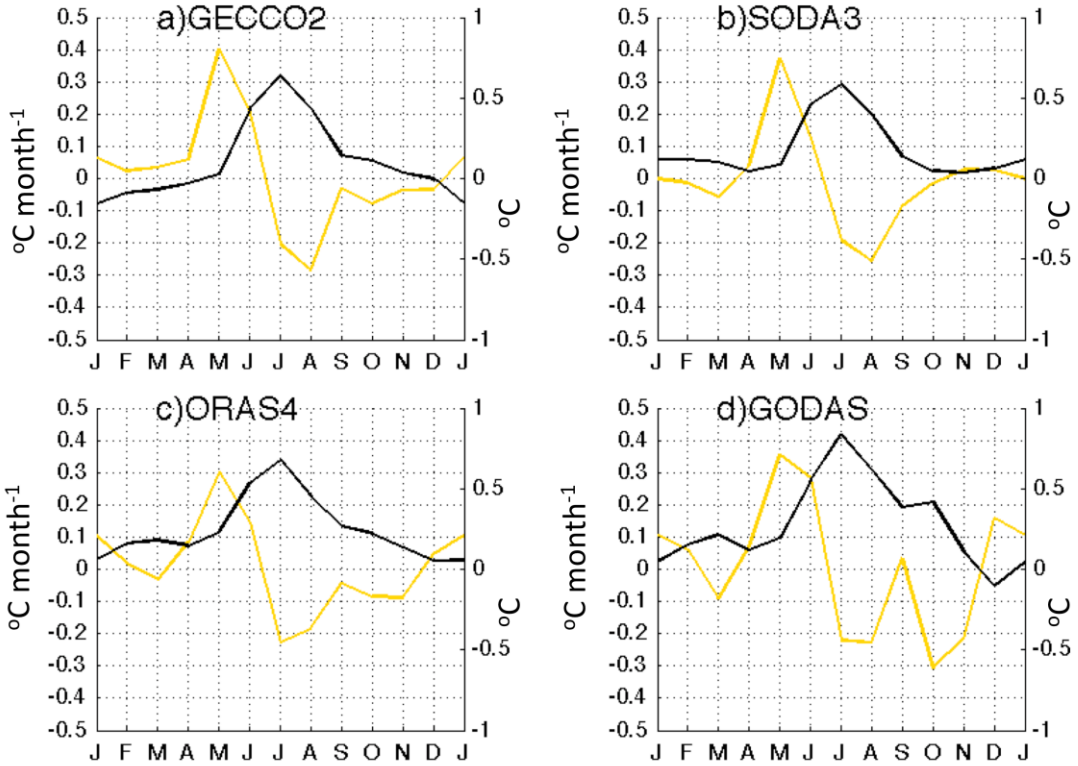

Figure 3.7 Time series difference between composite of weak monsoon years and composite of strong monsoon years for mixed layer temperature (black) and mixed layer temperature tendency (yellow) over western Arabian Sea (50°-65°E, 13°-23°N) for a) GECCO2, b) SODA3, c) ORAS4, d) GODAS. In each panel, the left y-axis is for mixed layer temperature tendency difference (°C month^{-1}) and the right y-axis is for mixed layer temperature difference (°C).

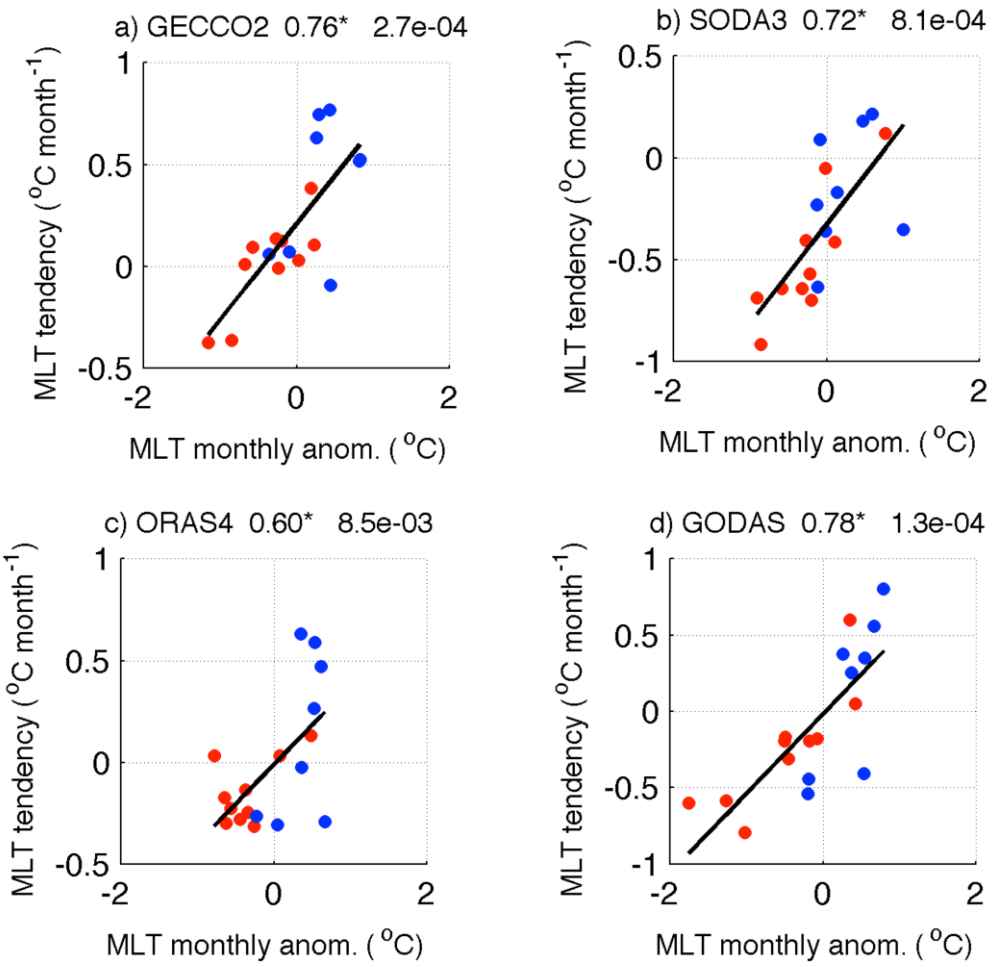

Figure 3.8 Scatterplot between mixed layer temperature monthly anomaly (x-axis) in July and mixed layer tendency (y-axis) in May for western Arabian Sea (50°-65°E, 13°-23°N). Blue and red dots indicate weak and strong summer monsoon years respectively. The title in each panel, from left to right, indicate model's name, Pearson correlation coefficient and p-value respectively. Student t-test is used to determine p-value of Pearson correlations coefficient that is statistically significant at 5% level (p-value < 0.05) denoted by asterisk. Black solid lines indicate linear trend line.

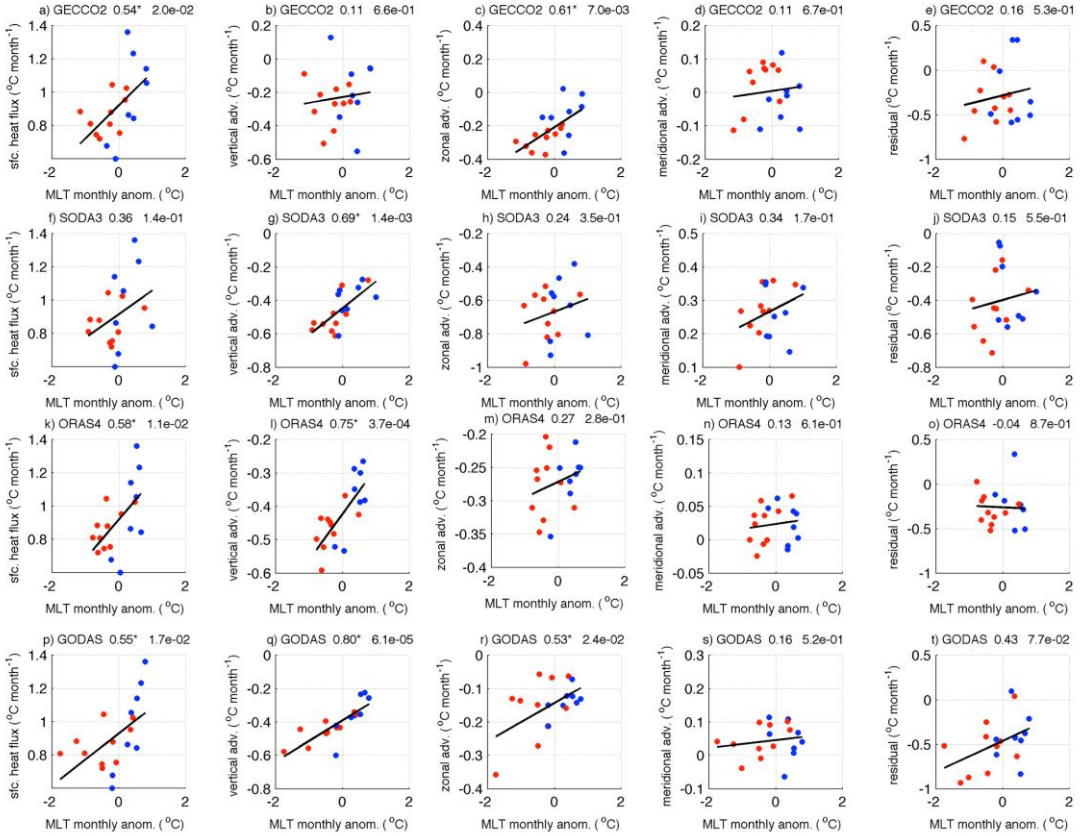

Figure 3.9 Scatter plot between heat budget components (°C month^{-1}) in May and mixed layer temperature monthly anomaly (°C) in July for western Arabian Sea (50°-65°E, 13°-23°N). Blue and red dots indicate weak and strong summer monsoon years respectively. The title in each panel, from left to right, indicates model's name, Pearson correlation coefficient and p-value respectively. Student t-test is used to determine p-value of correlations coefficient that is statistically significant at 5% level (p-value < 0.05) denoted by asterisk. Black solid lines indicate linear trend line.

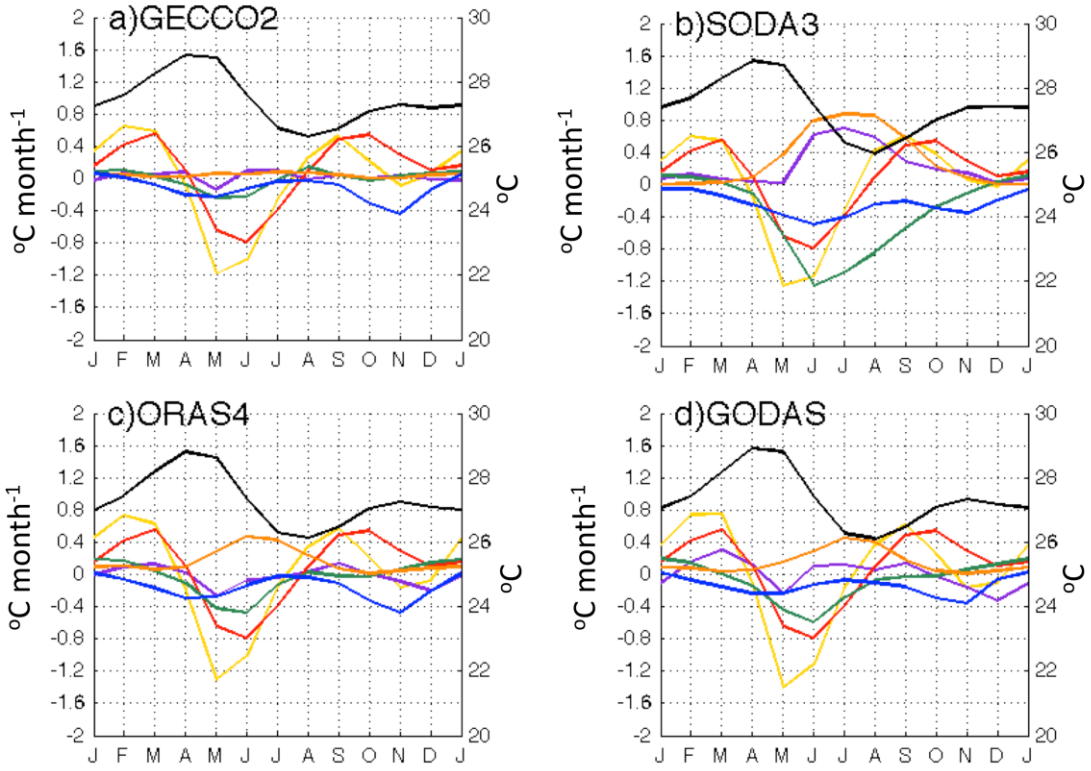

Figure 3.10 Time series of area averaged heat budget over western equatorial Indian Ocean (45°-60°E, 10°S-10°N) for a) GECCO2, b) SODA3, c) ORAS4 and d) GODAS. Mixed layer temperature, mixed layer tendency, surface heat fluxes are denoted by black, yellow and red colors respectively. Vertical, zonal and meridional heat advections are denoted by blue, green and orange colors respectively. Residual term is denoted by purple color. In each panel, the left y-axis is for heat budget components (°C month^{-1}) and the right y-axis is for mixed layer temperature (°C).

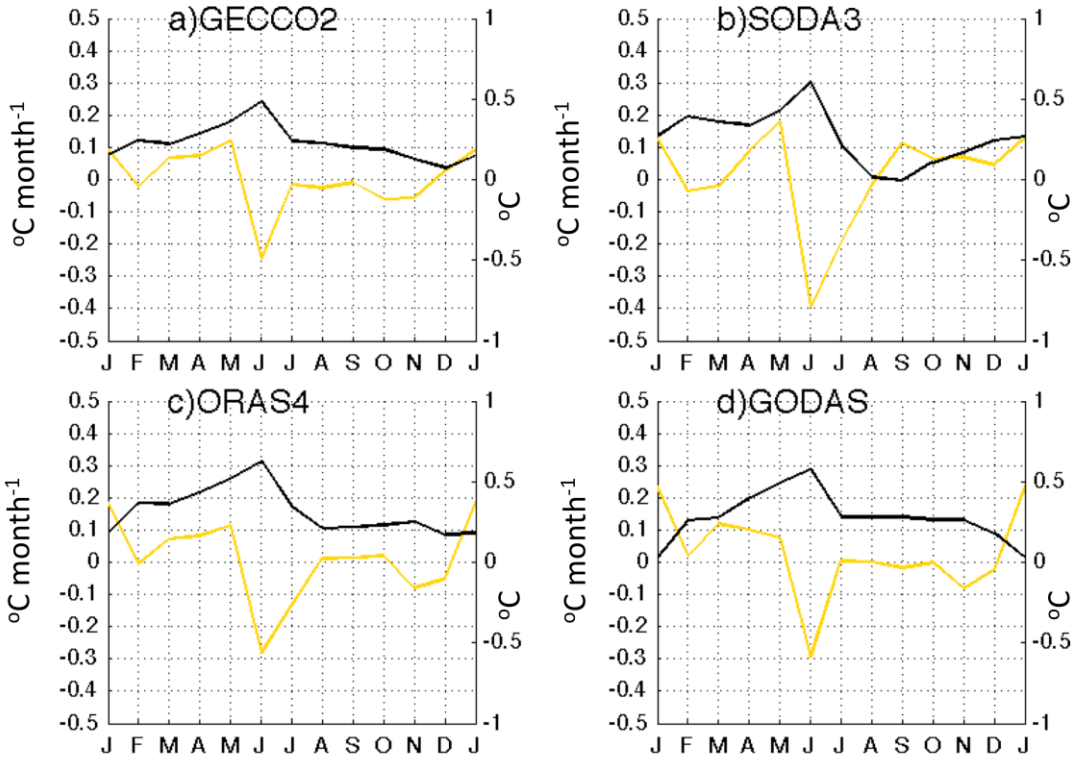

Figure 3.11 Time series for difference between composite of weak monsoon years and composite of strong monsoon years for mixed layer temperature (black) and mixed layer temperature tendency (yellow) over western equatorial Indian Ocean (45°-60°E, 10°S-10°N) for a) GECCO2, b) SODA3, c) ORAS4, d) GODAS. In each panel, the left y-axis is for mixed layer temperature tendency difference (°C month^{-1}) and the right y-axis is for mixed layer temperature difference (°C).

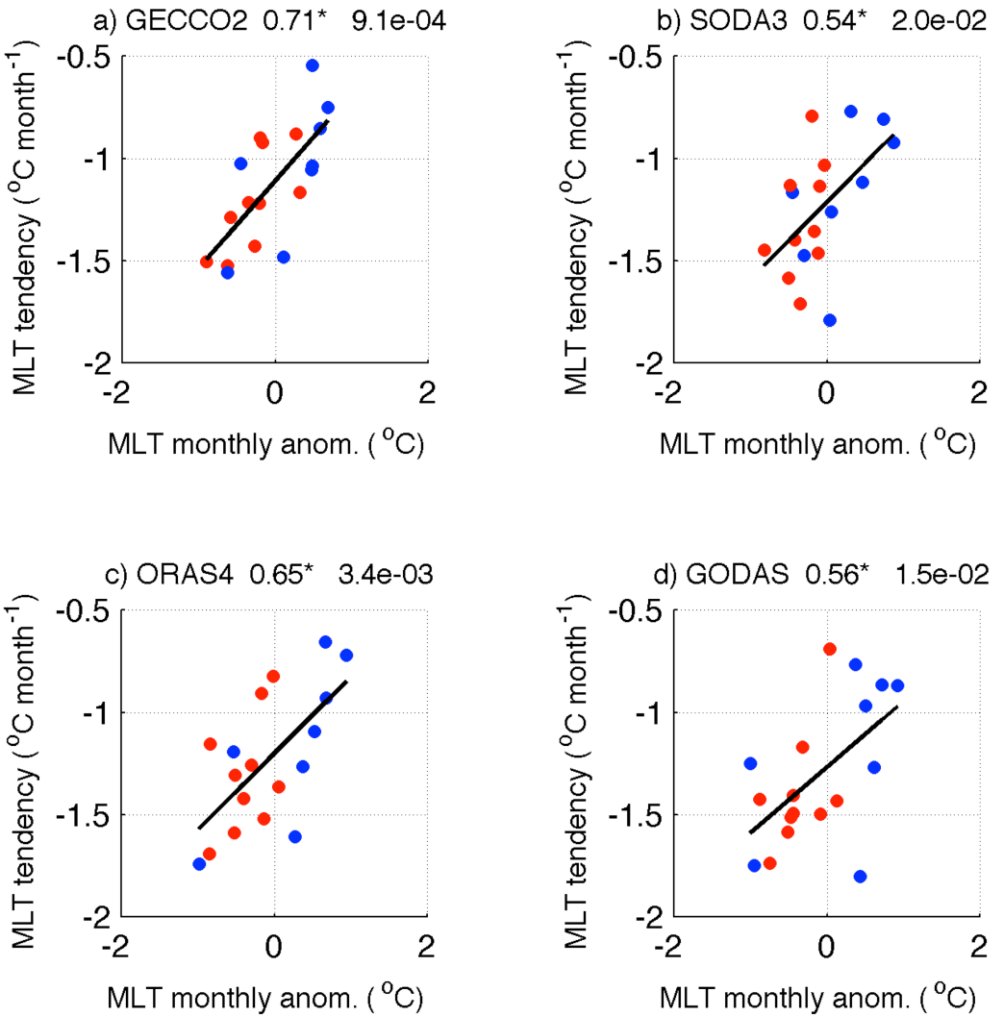

Figure 3.12 Scatterplot between mixed layer temperature monthly anomaly (x-axis) in June and mixed layer tendency (y-axis) in May for western equatorial Indian Ocean (45°-60°E, 10°S-10°N). Blue and red dots indicate weak and strong summer monsoon years respectively. The title in each panel, from left to right, indicate model's name, Pearson correlation coefficient and p-value respectively Student t-test is used to determine p-value of correlations coefficient that is statistically significant at 5% level (p-value < 0.05) denoted by asterisk. Black solid lines indicate linear trend line.

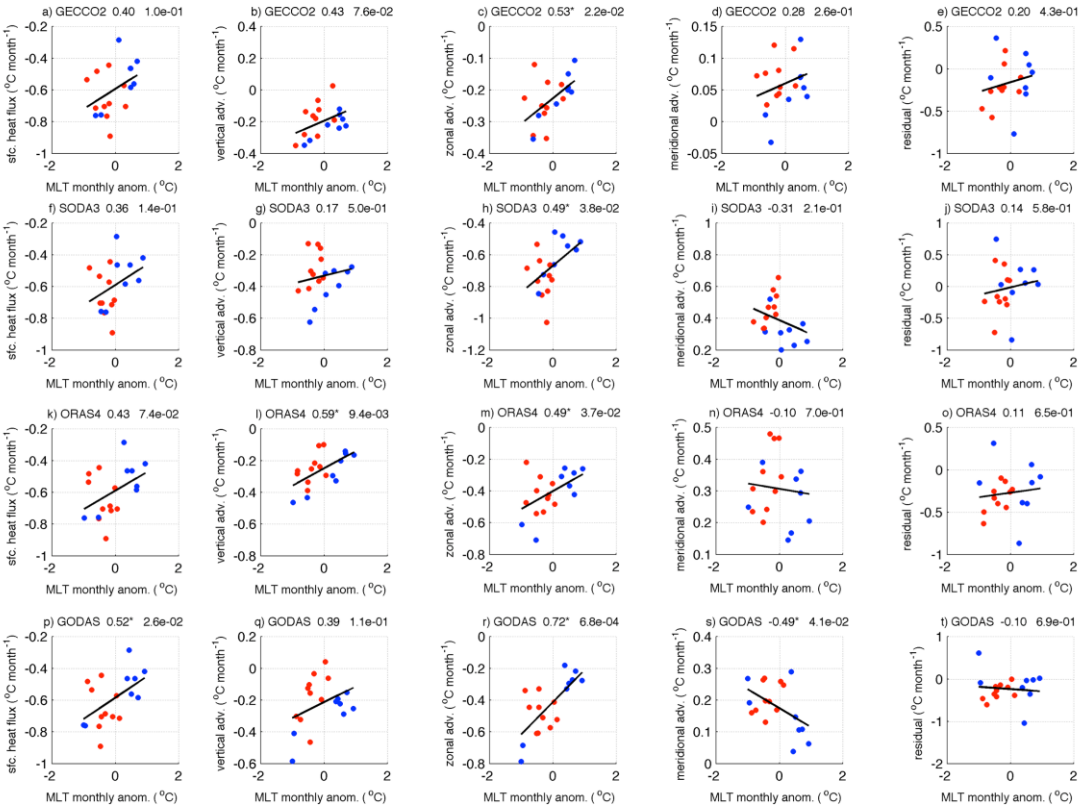

Figure 3.13 Scatter plot between heat budget terms (°C month^{-1}) in May and mixed layer temperature monthly anomaly (°C) in June for western equatorial Indian Ocean (45°-60°E, 10°S-10°N). The title in each panel, from left to right, indicate model's name, Pearson correlation coefficient and p-value respectively. Student t-test is used to determine p-value of correlations coefficient that is statistically significant at 5% level (p-value < 0.05) denoted by asterisk. Black solid lines indicate linear trend line.

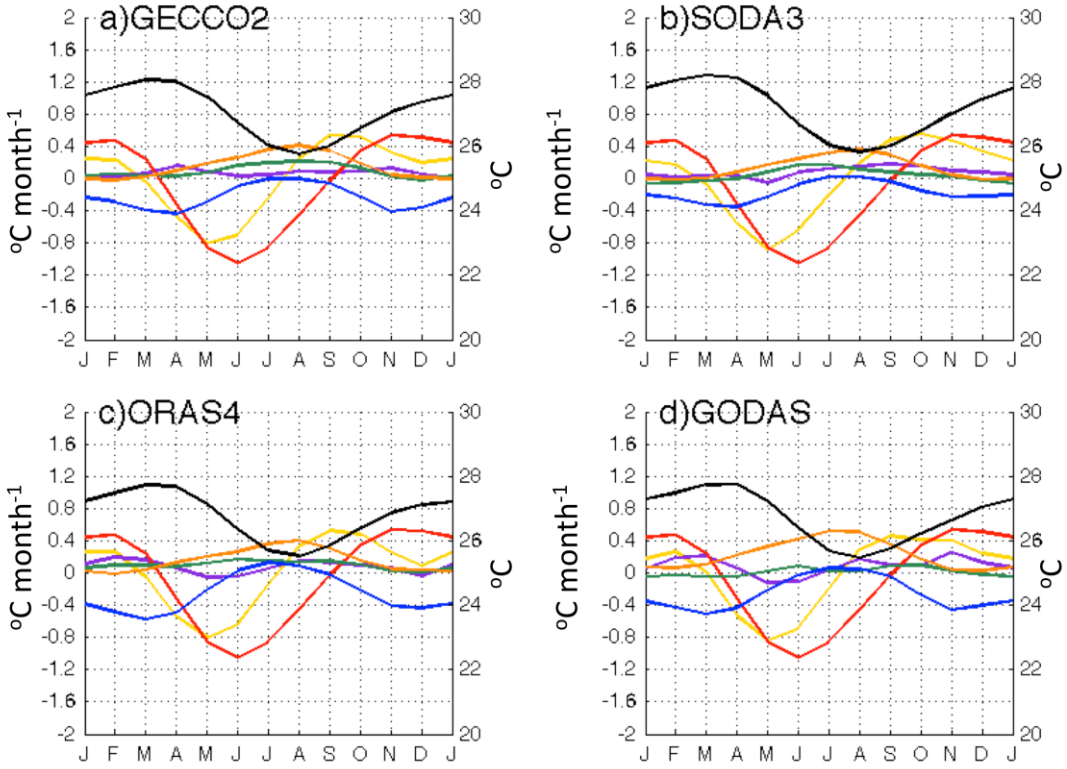

Figure 3.14 Time series of area averaged heat budget over southwestern Indian Ocean (50°-65°E, 15°S-5°S) for a) GECCO2, b) SODA3, c) ORAS4 and d) GODAS. Mixed layer temperature, mixed layer tendency, surface heat fluxes are denoted by black, yellow and red colors respectively. Vertical, zonal and meridional heat advections are denoted by blue, green and orange colors respectively. Residual term is denoted by purple color. In each panel, the left y-axis is for heat budget components (°C month^{-1}) and the right y-axis is for mixed layer temperature (°C).

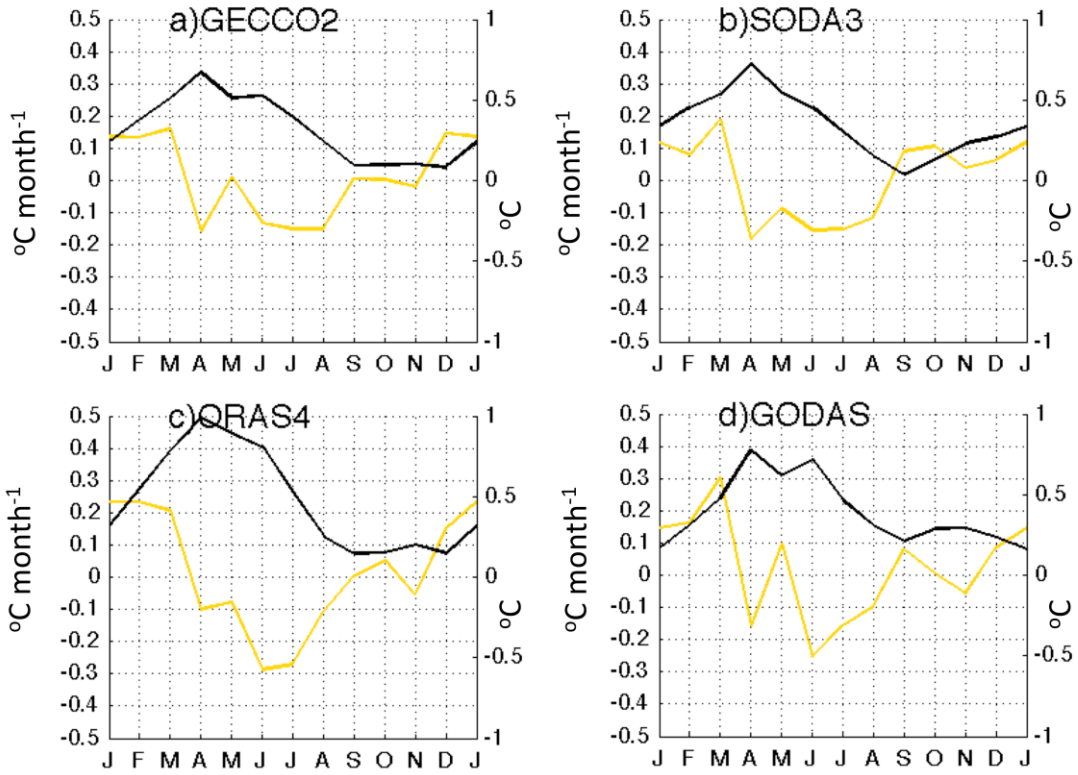

Figure 3.15 Time series for difference between composite of weak monsoon years and composite of strong monsoon years for mixed layer temperature (black) and mixed layer temperature tendency (yellow) over southwestern Indian Ocean (50°-65°E, 15°S-5°S) for a) GECCO2, b) SODA3, c) ORAS4, d) GODAS. In each panel, the left y-axis is for mixed layer temperature tendency difference (°C month^{-1}) and the right y-axis is for mixed layer temperature difference (°C).

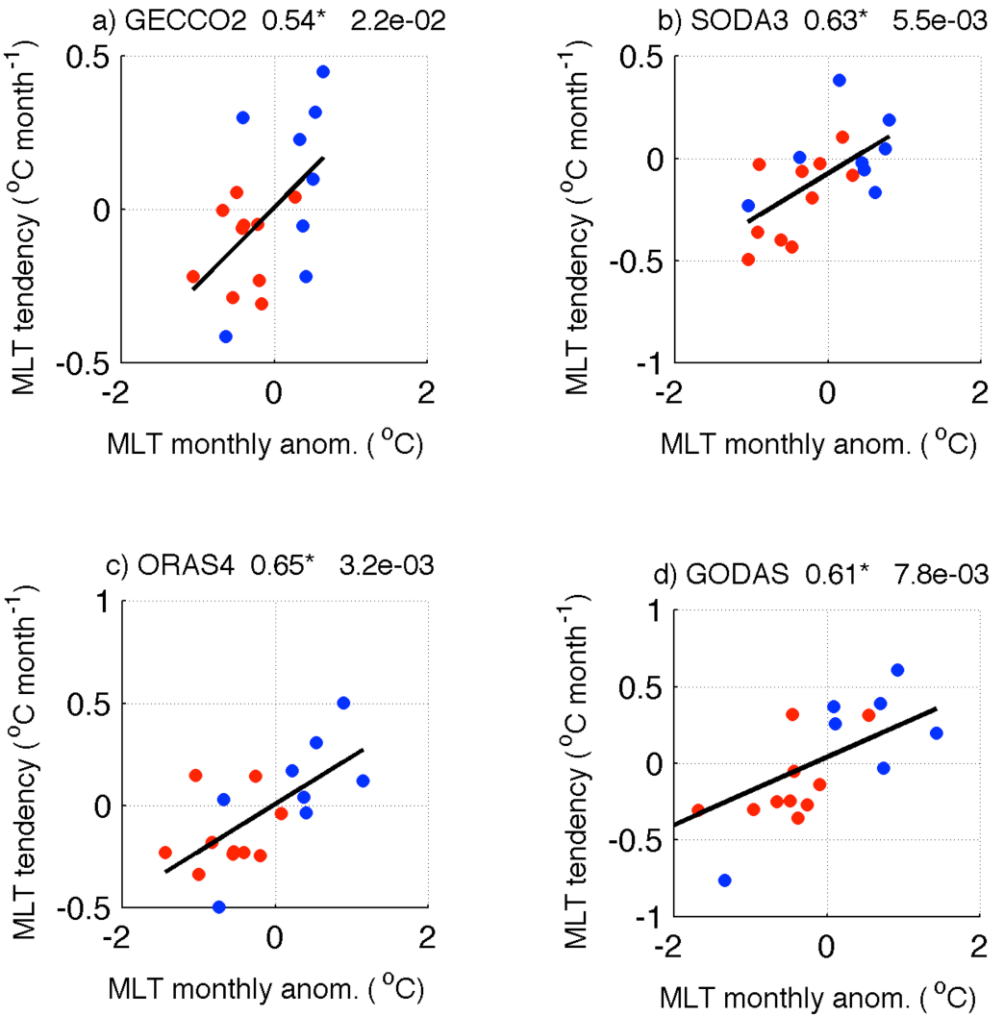

Figure 3.16 Scatterplot between mixed layer temperature monthly anomaly (x-axis) in April and mixed layer tendency (y-axis) in March for Southwestern equatorial Indian Ocean (55°-65°E, 15°S-5°S). Blue and red dots indicate weak and strong summer monsoon years respectively. The title in each panel, from left to right, indicate model's name, Pearson correlation coefficient and p-value respectively. Student t-test is used to determine p-value of correlations coefficient that is statistically significant at 5% level (p-value < 0.05) denoted by asterisk. Black solid lines indicate linear trend line.

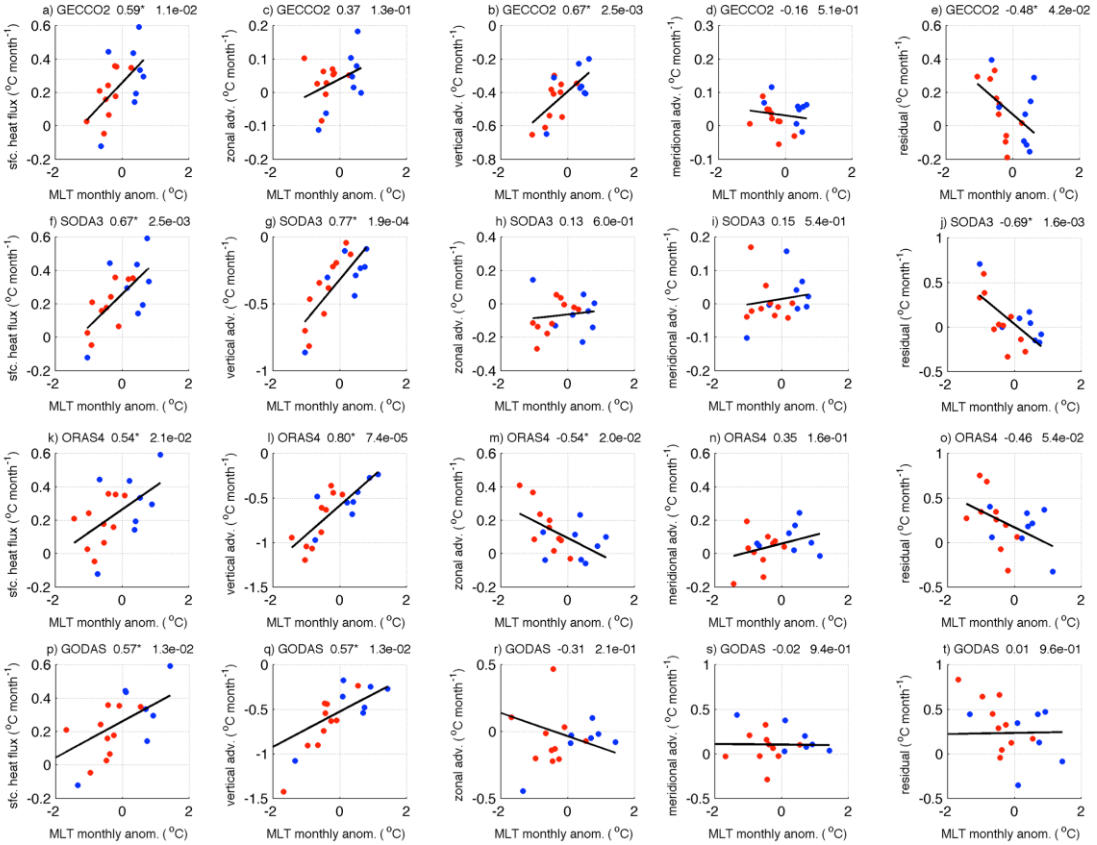

Figure 3.17 Scatter plot between heat budget terms (°C month^{-1}) in March and mixed layer temperature monthly anomaly (°C) in April for Southwestern Indian Ocean (55°-65°E, 15°S-5°S). The title in each panel, from left to right, indicate model's name, Pearson correlation coefficient and p-value respectively. Student t-test is used to determine p-value of correlations coefficient that is statistically significant at 5% level (P-value < 0.05) denoted by asterisk. Black solid lines indicate linear trend line.

Table 3.1 Pearson correlation coefficient between heat budget terms averaged in September, October, November and mixed layer temperature anomaly averaged in December, January and February for all models over WEIO. Statistically significant correlation coefficients with p-value < 0.05 are denoted by bold font.

Heat Budget term	GECCO2	SODA3	ORAS4	GODAS
mixed layer tendency	**0.78**	**0.48**	**0.80**	**0.60**
surface heat flux	**0.70**	0.16	-0.04	-0.10
zonal adv	0.13	**0.48**	0.38	0.23
meridional adv	**0.70**	-0.25	**0.76**	0.35
vertical adv	**0.48**	**0.52**	**0.69**	**0.80**
residual	-0.02	-0.43	-0.02	-0.13

4 Evaluation of ocean advection role of CMIP5 models in generating SST bias in western Indian Ocean

4.1 Introduction

Climatologically, winds over the equatorial Indian Ocean are westerly throughout the year, which results in a lack of equatorial upwelling in eastern parts. Seasonally, the prevailing southwesterly winds during the summer monsoon season (June–September) generate offshore Ekman transport near the sea surface, which produces upwelling in the western Arabian Sea. This upwelling has pronounced effect on the transport of moisture toward the west coast of India and on precipitation during the summer monsoon season (Izumo et al., 2008). During the winter monsoon season (November–April), in conjunction with seasonally reduced insolation, northeasterly monsoon winds bring dry air from the Asian continent, cooling the SST in the North Indian Ocean via surface heat loss. Consequently, climatological SSTs are cooler in the western tropical Indian Ocean and warmer in the east. Hence, atmospheric convection is suppressed over western regions, whereas in eastern and central parts, characterized by warm SSTs >26 °C, conditions are highly conducive for enhanced atmospheric convection. This contrasts with the other two tropical oceans, the climatological SSTs of which are warmer in western parts than in the east (Schott et al., 2009).

On interannual time scales, the Indian Ocean exhibits basinwide SST warming in boreal winter that peaks in the following spring after the mature phase of ENSO. This is driven by an increase in surface heat fluxes linked to variations in cloud cover and evaporation associated with changes in atmospheric circulation (Klein et al., 1999). Murtugudde and Busalacchi (1999) documented that surface heat flux is the major mechanism for ENSO-induced warming in the northern Indian Ocean. However, the southwestern tropical Indian Ocean SST warming is forced also by thermocline variability (Xie et al., 2002, 2009). Additionally, SSTs in the western tropical Indian Ocean become occasionally warmer than normal, accompanied by cooler SSTs in the southeastern equatorial Indian Ocean. A number of studies have investigated the heat budget of the SST variability of IOD (Saji et al., 1999), using ocean models (Murtugudde et al., 2000; Vinayachandran et al., 2002; Li et al., 2002) and CGCMs (Iizuka et al., 2000). They demonstrated that the anomalous warming in the western

tropical Indian Ocean associated with IOD events is mainly caused by anomalous horizontal and vertical temperature advection. Murtugudde et al. (2000) further documented that the western equatorial region underwent surface warming from May 1997 onward, with peak SST anomalies of nearly 2°C in February 1998. They found that a weaker southwesterly monsoon resulted in initial warming because of anomalous meridional advection and reduced entrainment cooling. Furthermore, Izumo et al. (2008) described that an anomalous increase in SST along the Somalia–Oman coasts during summer is caused by reductions in upwelling accompanied by anomalously weak southwesterly winds in late spring over the Arabian Sea that are due to warm SST/increased precipitation anomalies over the thermocline ridge of the southwestern tropical Indian Ocean. The latter SST/precipitation anomalies are often related to El Niño conditions and the strength of the Indonesian–Australian monsoon during the previous winter.

The CMIP3 and CMIP5 models provide the opportunity to investigate the influence of SST on past and projected future climates (Meehl et al., 2007; Taylor et al., 2012). However, tropical SST biases of state-of-the-art CGCMs are comparable to or larger in magnitude than the observed interannual variability and projected change in the 21st century, which can be traced back to the biases in cloud cover and ocean thermocline depth (Li and Xie, 2012). Annual mean equatorial easterly wind biases over the tropical Indian Ocean in CMIP5 models are coupled with an unrealistic mean slope of the equatorial thermocline that is tilted toward the eastern Indian Ocean (Cai and Cowan, 2013). These biases are accompanied by SST biases with a pattern similar to the IOD SST variability during summer and fall (Li et al., 2015a).

Previous studies have suggested that SST biases over the western Indian Ocean are linked to a weaker southwesterly summer monsoon (Levin et al., 2013; Li et al., 2015a). In addition, Yang et al. (2015) compared the differences in surface heat fluxes between the CMIP5 and the Atmospheric Model Intercomparison Project (AMIP) simulations of a single model. As mentioned in chapter 1, that Yang et al. (2015) highlighted that warm SST biases over the WEIO could be explained by both insufficient ocean dynamical cooling and latent heat flux, whereas the cool SST bias in spring could be mostly explained by insufficient shortwave radiation and excess latent heat flux. However, previous works (Li et al., 2015a; Yang et al., 2015) had not answered what process that initiate the warm SST biases over the WEIO yet, which lead to the development of the IOD-like biases in fall.

In the present study, we examined the intermodel SST biases over the Indian Ocean simulated in CMIP5 historical runs by analyzing the heat budget. In particular, we focused on the SST biases over the western Indian Ocean. It was found that the multi-model ensemble-mean (MME) SST biases over the WEIO are warmer than the observations during the summer monsoon season. However, about half the models show the positive SST biases whereas negative ones in the other half. Our analysis revealed the importance of ocean currents in forming the early summer development of SST biases over the WEIO, which has not been examined fully in previous studies. Indian Ocean SST is one of the important factors that affect regional and global climate (Xie et al., 2002, 2009; Schott et al., 2009) and hence, the evaluation of intermodel SST bias is an important step in the drive toward reducing bias in future climate model development/improvement.

4.2 Data and methods

Data and methods used in this chapter have been described in chapter 2 in more detail. Ocean heat budget equation was utilized to investigate the underlying cause of SST bias in 19 CMIP5 models over western Indian Ocean. For analyzing purposes, the horizontal and vertical grids both observation and CMIP5 models were set into similar uniform grids with help of linear interpolation. The horizontal grids were set to 1° × 1° uniform grid, while vertical ocean grids was set to 25 level.

4.3 Results and Analysis

4.3.1 Features of Indian Ocean SST bias

Figure 4.1 shows the MME biases of SST and surface winds of the CMIP5 models relative to observations. Warm SST biases become prominent over the WEIO during summer (Figure 4.1c), and they are accompanied by weaker southwest monsoonal winds over the Arabian Sea and equatorial southeasterly wind biases (Figure 4.1g). These warm SST biases are sustained until boreal fall (Figure 4.1d), accompanied by the development of equatorial easterly wind biases (Figure 4.1h) (Li et al., 2015a), and then they disappear in winter (Figure 4.1a). Another notable feature of the CMIP5 models is cold SST biases over the northern Arabian Sea during the pre-monsoon season (Figure 4.1b), although cold SST biases are observed over most of the

tropical Indian Ocean throughout the year (Figure 4.1a–d). Previous studies have documented that anomalous advection of cold air masses from the south Asia landmass during boreal winter contributes to the cold SST biases over the Arabian Sea (Marathayil, et al., 2013; Sandeep and Ajayamohan, 2014). These cold SST biases over the Arabian Sea weaken in boreal summer and fall (Figure 4.1c and d).

Subsurface temperature is another important factor that controls SST, particularly over equatorial oceans. Thus, we present the MME biases of subsurface ocean temperature at the depth of 75 m (Figure 4.1e–h). It is apparent that there are the colder (warmer) subsurface temperature biases in the eastern (western) equatorial Indian Ocean from summer through winter. In boreal spring, warm biases are observed over the southwestern tropical Indian Ocean from 5°–10°S (Figure 4.1f). These warm biases are related to equatorial easterly wind biases (Cai and Cowan, 2013; Nagura et al., 2013; Li et al., 2015a, b). Other biases of subsurface temperature are found along the southern and western coasts of India during summer and fall. Shankar et al. (2002) reported that local winds are favorable for generating upwelling coastal Kelvin waves during summer. The MME surface winds around southern Indian have southeasterly biases (Figure 4.1g), which are favorable for generating coastal downwelling Kelvin waves. Thus, it is implied that the local monsoon wind biases cause warm subsurface temperature biases.

4.3.2 SST bias over the Arabian Sea

Figure 4.2 shows the seasonal cycle of SST over the Arabian Sea (55°–75°E, 15°–25°N) for the various CMIP5 models together with observations. The observed annual cycle of SST over the Arabian Sea exhibits a bimodal distribution with the primary maximum during May–June and the secondary maximum in October. The SST is cooled during summer because of upwelling and offshore advection near the Oman coast, and because of latent heat loss caused by strong southwesterly monsoon winds. The SST cooling over the Arabian Sea is stronger during winter, which is particularly related to latent heat loss caused by cool dry air blowing off the Asian Continent (Schott et al., 2009). The seasonal cycle of SST in the CMIP5 models also shows a bimodal distribution, except for model M14. However, the SSTs in all the models (except M14) are colder than the observations during the winter monsoon season. Furthermore, the MME fails to simulate the primary maximum during May–June. The coldest SST biases

between the MME and observations are found in April.

Figure 4.3a shows the heat budget of the uppr-50-m temperature over the Arabian Sea for the MME. The heat budget equation employed in this study was similar to Ng et al. (2015) as shown in Eq. (2.1). It is noted that the use of a different constant MLD, based on its seasonal minimum and maximum (4.3d), has little effect on the advection terms in the heat budget (Figure 4.3a), whereas the contributions of the surface heat flux and residual terms are influenced by differences in the MLD during winter (see Appendix). As is shown later, however, this does not change the present results for the difference in heat budget among the CMIP5 models.

The cooling in June–July is attributed partly to three components (Figure 4.3a): vertical advection such as upwelling along the Oman coast, zonal advection that indicates offshore Ekman transport near the sea surface of cold water due to upwelling, and the residual term that includes vertical mixing processes as well as unresolved high-frequency variability. Conversely, the cooling from October to January is mainly attributable to surface heat fluxes, while the residual term contributes partly to the warming that modulates the surface cooling. Although vertical mixing processes and unresolved high-frequency variability are included in the residual term, it could be interpreted that the residual term contributing to the warming in winter results rather from a convective adjustment process associated with strong surface cooling (see Appendix).

To examine the intermodel diversity of SST biases, the heat budget averaged for four models (i.e., M21, M13, M16, and M17) as the warmest April SST and that for four models (i.e., M1, M3, M6, and M8) as the coldest April SST is shown in Figure 4.3b and 4.3c, respectively. The SSTs for the warmest four models show the primary maximum during May–June, as in the observations, whereas the SSTs for the coldest four models show the primary maximum in October and the secondary maximum in July. The cold biases of temperature extend much deeper in the coldest models than in the warmest models during fall–spring (Figure 4.3e and f). The seasonal evolution of SST during fall and winter for both composites is controlled mainly by surface heat fluxes, and the contributions of the advection terms are much smaller. The cooling due to surface heat fluxes during fall and winter is larger in the coldest models than in the warmest model (Figure 4.3b and c).

Figure 4.4a shows the relationship between surface heat flux during fall–winter and the April SST biases among the CMIP5 models. A close relationship between the

two variables can be found (Figure 4.4a). The cooling that causes the April SST biases is attributable to the latent heat flux and sensible heat flux during winter (Figure 4.4d and e), whereas there is no significant relationship between shortwave radiation and cold SST biases (Figure 4.4b). The relation with longwave radiation shows the negative correlation (Figure 4.4c), indicating that the models with the colder SST biases have lower air temperatures (Figure 4.4f). Note that the lower correlation of the latent heat fluxes compared with the sensible heat fluxes might result from the SST-dependency of latent heat fluxes. Previous studies have suggested that cold SST biases over the northern Arabian Sea during the pre-monsoon season result from anomalous advection of cold air masses from the south Asian landmass during boreal winter (Marathayil et al., 2013; Sandeep and Ajayamohan, 2014). The results of the present study corroborate these earlier findings.

4.3.3 SST bias over the western equatorial Indian Ocean

Figure 4.5 shows the seasonal cycle of SST over the WEIO (45°–60°E, 10°S–10°N) among the CMIP5 models together with observations. The observed annual cycle of SST over the WEIO also exhibits a bimodal distribution with the primary and secondary maxima during April and November, respectively, and the primary and secondary minima in August and January, respectively. All the CMIP5 models reproduce the bimodal distribution of the seasonal cycle of SSTs. However, the SSTs in most of the models are colder than the observations during winter and spring. Conversely, both positive and negative SST biases are found in summer and fall, and the MME SST biases are warmer than the observations.

To examine the intermodel diversity of SST biases, the seasonal cycle of SST biases for four models (i.e., M8, M14, M6, and M2) as the warmest July SST over the WEIO, and that for four models (i.e., M19, M18, M13, and M20) as the coldest July SST is shown in Figure 4.6. The SST biases over the WEIO for the warm composite are much warmer than the cold composite in July. These are accompanied by a weaker summer monsoon over the WEIO during summer and the development of easterly wind biases over the equatorial Indian Ocean during fall (Figure 4.6c and g) (Li et al., 2015a). For the cold composite, the SST biases over the WEIO during summer are smaller than for the warm composite. In addition, cold SST biases are prominent over the entire tropical Indian Ocean throughout the year (Figure 4.6e–h). The wind biases over the

equatorial Indian Ocean are southeasterly for the cold composite during summer and fall (Figure 4.6g and h). Northeasterly wind biases are found along the Somali and Oman coasts in the cold composite during winter (Figure 4.6e), whereas there are northerly wind biases in the warm composite during spring (Figure 4.6b). The difference in the wind biases between the warm and cold composites induces the subsurface temperature biases (Figure 4.7). The warmer subsurface temperature biases that are coupled to the equatorial zonal wind biases (Li et al., 2015b) and a deeper thermocline, are remarkable in the southwestern tropical Indian Ocean for the warmer composite.

Figure 4.8a shows the heat budget of the upper-50-m temperature over the WEIO for the MME. Cooling occurs from May to July because of both ocean processes and surface heat fluxes. The latter is related to latent heat loss caused by the strong southwesterly monsoon winds. Figure 4.8b and 4.8c shows the heat budget averaged for the warm and cold composites, respectively. A prominent difference in the SST between the warm and cold composites is found in the annual mean, although both composites show a bimodal distribution of the seasonal cycle of SST. The difference in annual mean temperature between the composites can be seen in the subsurface (Figure 4.8e and f). The thermocline depth is deeper in the warm composite than in the cold composite, which leads to a relatively weaker cooling due to vertical advection in the warm composite throughout the year (cf. Figure 4.8b and c). Conversely, the temperature biases of the cold composite during winter are confined to the mixed layer (Figure 4.8f). Although there is a difference in the annual mean SST between the warm and cold composites, intermodel diversity of the SST biases appears in June and it is sustained until fall (Figure 4.7). It is considered that the difference in SST biases between the composites in summer is caused by the difference in the cooling tendency in May, which is the period of transition from the winter monsoon to the summer monsoon. In fact, the largest difference in the cooling tendency of the upper-50-m temperature between the warm and cold composites is observed in May (cf. Figure 4.8b and c).

Figure 4.9 shows the relationship of the July SST biases over the WEIO with each term of the upper-50-m heat budget in May. Among each term, the strongest correlation is found in the relation with the zonal advection term (Figure 4.9b). The vertical advection and residual term, including the vertical mixing processes as well as the unresolved high-frequency variability, also appears to contribute to the warm SST

biases in July (Figure 4.9c and d). However, there is no clear relationship between the surface heat fluxes in May and the July SST biases (Figure 4.9a).

To elucidate further the role of advection on the formation of SST bias in July, Eq. (2.2) was used which decomposed the variable in heat budget equation into the MME and its deviation from MME. The strongest correlation of the zonal advection term (Figure 4.9b) comes from both the zonal advection of the temperature deviation by the MME currents (Figure 4.10a) and the zonal advection term of the MME temperature by the current deviation (Figure 4.10b). Figure 4.11 presents the seasonal evolution of SST, surface wind, and surface ocean currents deviations among the CMIP5 models from the MME regressed on the July SST biases over the WEIO. It is suggested that the warm SST biases over the WEIO in July can be initiated by the advection of warm SST over the central equatorial Indian Ocean by the anomalous westward surface currents (Figure 4.11k) at around 5°N, in response to the relatively weaker monsoon wind biases (Figure 4.11c), and vice versa. In other words, model with relatively weaker (stronger) monsoon wind biases weaken (strengthen) the SST cooling through offshore Ekman transport near the sea surface, resulting in warm (cold) SST bias over the WEIO. Another process that could possibly cause warm (cold) SST biases over the WEIO in July is the zonal advection of relatively warm (cold) SST biases over the southwestern equatorial Indian Ocean (10°S–Eq., 40°–55°E) by the northeastward-flowing East African Coastal Current (EACC) (Schott and McCreary, 2001) (Figure 4.11g). Note that part of the EACC transports relatively warm (cold) SST biases toward the Arabian Sea, leading to negative correlation in the meridional advection of the temperature deviation by the MME currents (Figure 4.10d). The contributions from the nonlinear dynamical heating (Figure 4.10c, f, and i) and the advection of the MME temperature by the meridional current deviation (Figure 4.10e) are smaller than from the other terms.

To elucidate the external heat source and sink controlling the formation of SST bias over the southwestern equatorial Indian Ocean in May, the heat budget in the upper 50 m was examined using formulation Eq. (2.6). Figure 4.12 presents the relationship of the July SST biases over the WEIO with each term of the upper-50-m heat budget in March, i.e., two months before the SST bias appear over the southwestern equatorial Indian Ocean in May. Note that no flux condition is imposed on the western face at the eastern African coast. The SST bias over the southwestern equatorial Indian Ocean in May is related to the heat transport through the eastern and southern faces of the box

(Figure 4.12a and b) while the contribution of heat transport through the northern face is negligible (Figure 4.12c). There is no clear relation with the vertical heat transport (Figure 4.12d) and residual term (not shown). The surface heat flux shows negative correlation (not shown), indicating that it acts to damp the SST bias.

The relation with heat transport through the eastern face suggests that models with greater (lesser) outflow of heat through the eastern face tend to cause the relative colder (warmer) SST bias in the southwestern equatorial Indian Ocean in May. This leads to the relatively colder (warmer) SST bias over the WEIO in July through the meridional advection of the temperature deviation by the MME currents (Figure 4.10d). Because the range of difference between the box-averaged temperature and the temperature at the eastern face is small among the CMIP5 models (Figure 4.12e), the difference in heat transport through the eastern face among CMIP5 models can be attributed to that of the South Equatorial Counter Current (SECC) (Figure 4.12g) flowing eastward around 2°–4°S (Schott and McCreary, 2001; Schott et al., 2009) (Figure 4.11e).

The relation in heat transport though the southern face (Figure 4.12b) suggests that models with greater (lesser) inflow of heat through the southern face tend to cause the relatively colder (warmer) SST bias in the southwestern equatorial Indian Ocean in May, which leads to the SST bias over the WEIO in July. This is partly because models with greater (lesser) northward inflow of heat through the southern face are associated with the stronger (weaker) northward flow mostly representing the EACC (Figure 4.12g and h). It is noted that the intensity of the EACC is closely related to the intensity of the SECC (Figure 4.12h) and the South Equatorial Current (not shown) flowing westward south of 10°S (Schott and McCreary, 2001; Schott et al., 2009) (Figure 4.11e). It is reported that a similar relation can be found in observations in association with the IOD events (Palastanga et al., 2006). It seems that a stronger (weaker) EACC is related to the bias in the thermocline depth over the southwestern Indian Ocean (In this case, the southwestern Indian Ocean is the region in WIO around 30°S-Eq) (Figure 4.7b and f). Nagura et al. (2013) documented that the bias of the shallow climatological thermocline in the southwestern tropical Indian Ocean is induced by the biases of wind stress curl.

Another relation in the heat transport though the southern face (Figure 4.12b) is associated with the northward transport of temperature bias through the southern face by MME currents (Figure 4.12f). This suggests that the advection of relatively warm

(cold) SST biases over the southwestern tropical Indian Ocean south of 10°S by the EACC can initiate the warm (cold) SST bias over the southwestern equatorial Indian Ocean in May, leading to the SST bias over the WEIO in July (Figure 4.11e–h).

We also note that a close relation can be found in the vertical advection of the temperature deviation by the MME currents (Figure 4.10g), whereas there is no significant negative correlation in the vertical advection of the MME temperature by the current deviation (Figure 4.10h). This shows that the influence of the vertical advection term on the SST bias (Figure 4.9d) in the WEIO comes mostly from the vertical advection of the subsurface temperature bias, indicating that models with a deeper (shallower) mixed layer have positive (negative) SST bias. This indicates that insufficient (excess) cooling due to upwelling associated with a deeper (shallower) thermocline in the WEIO (Figure 4.8e and f) also helps the development of warm (cold) SST biases in summer. It is noted that the use of a different constant MLD, based on its seasonal minimum and maximum (Figure 4.8d), has little effect on the advection terms in the heat budget (Figure 4.8a). Therefore, it is suggested that the ocean processes mentioned above are responsible for the SST biases over the WEIO during summer among the CMIP5 models.

4.4 Summary and discussion

The present study examined the SST biases over the Indian Ocean in the CMIP5 models. Almost of all the CMIP5 models show prominent cold SST biases over the northern Arabian Sea during the pre-monsoon season. The magnitudes of the biases are mainly attributable to the difference in latent heat flux and sensible heat flux during the winter monsoon season among the CMPI5 models. It was also found that the MME SST biases over the WEIO are warmer than the observations during the summer season, accompanied by equatorial easterly wind biases. However, the biases are positive in about the half models whereas negative in the other half. The models with warmer SST biases exhibit an IOD-like pattern, with strong equatorial easterly wind biases during fall and a deeper thermocline in the WEIO. In the models with cooler SST biases, negative SST biases are observed over the entire tropical Indian Ocean throughout the year and the wind biases over the equatorial Indian Ocean are southeasterly during summer and fall. Heat budget analysis indicated that the early summer development of SST biases over the WEIO is attributable to the surface current biases induced by the

weaker biases of southwesterly monsoon winds. The cooler SST biases over the southwestern Indian Ocean advected by the East African Coastal Currents also contribute to the formation of the SST biases over the WEIO. The SST bias over the southwestern Indian Ocean is induced by biases in the EACC and the SECC associated with biases of thermocline depth in the southwestern Indian Ocean and the SST bias over the southern Indian Ocean south of 10°S among the CMIP5 models during spring. The bias in thermocline depth also helps in the early summer development of SST bias over the WEIO.

In the CMIP5 models with warmer summer SST biases over the WEIO, wind biases prior to the onset of the summer monsoon are northeasterly to the north of the equator and northwesterly to the south of the equator (Figure 4.6). This pattern is accompanied by lower precipitation over the Arabian Sea and warmer SST over the south Indian Ocean (Figure 4.11). These asymmetric patterns are somewhat similar to the observed anomalous atmospheric and oceanic responses to El Niño that affect the early summer monsoon (Kawamura et al., 2001). However, there is a notable difference between the biases among the CMIP5 models and observations. In the observations, the maximum SST warming in response to El Niño tends to appear over the southwestern tropical Indian Ocean north of 12°S via SST–thermocline feedback (Xie et al., 2002, 2009; Izumo et al., 2008). Conversely, large variation of the SST biases among the CMIP5 models is found over the southwestern tropical Indian Ocean south of 10°S. Thus, the biases of the Seychelles–Chagos thermocline ridge over the southwestern Indian Ocean (Li et al., 2015b) are not related to the SST there; instead, surface heat fluxes mainly control the SST (Santoso et al., 2010). Actually, the heat budget analysis showed that the surface heat fluxes induce the diversity of the SST biases among the CMIP5 models over the southern Indian Ocean south of 10°S (not shown). Therefore, the difference in the meridional position of SST anomalies over the southwestern Indian Ocean suggests that the processes causing the SST biases over the WEIO among the CMIP5 models are different from those often observed in response to El Niño.

It might be expected that the cold SST biases over the Arabian Sea during winter and spring induce weaker southerly winds over the WEIO in spring and subsequently, induce the warm SST biases over the WEIO. However, the relationship between the July SST biases over the WEIO and the April SST biases over the Arabia Sea is unclear (Figure 4.9f). Thus, the colder SST biases over the Arabian Sea during winter and

spring are not linked to the SST biases over the WEIO during summer via weak monsoon biases (Figure 4.9f). Therefore, it is suggested that the diversity of the SST biases over the southern Indian Ocean could potentially affect the regional climate over the equatorial and northern Indian Ocean.

The present study illustrated the importance of ocean currents in forming the early summer SST biases over the western tropical Indian Ocean, which has not been examined fully in previous studies. We investigated further whether variation of the horizontal and vertical resolution of CMIP5 models might influence the representation of ocean current, in particular the EACC. These are shown in Table 4.1. Information about number of grids and resolution are shown in Table 2.1. Pearson correlation between number of latitudinal grids and southward ocean water transport at southern face displays is -0.35 with p-value 0.12 which is greater than 0.1 (below 90% of confidence level). Correlation between number of longitudinal grid and eastward water transport at eastern face is not significant with Pearson correlation is -0.02 and p-value greater than 0.1. Relation between number of vertical layers in model and ocean water transport at southern and eastern boundary display low correlation (0.17 and -0.03, respectively) and not significant (0.45 and 0.89, respectively). Pearson correlation was also calculated between the finer latitudinal grid near the equator in every CMIP5 models and ocean water transport at eastern and southern face. We excluded M10, M16 and M18 because the difficulties in determining the finest resolution near the equator. It also shows low correlation and not significant. These may indicate that horizontal and vertical resolutions are not essential factor to represent the western boundary current.

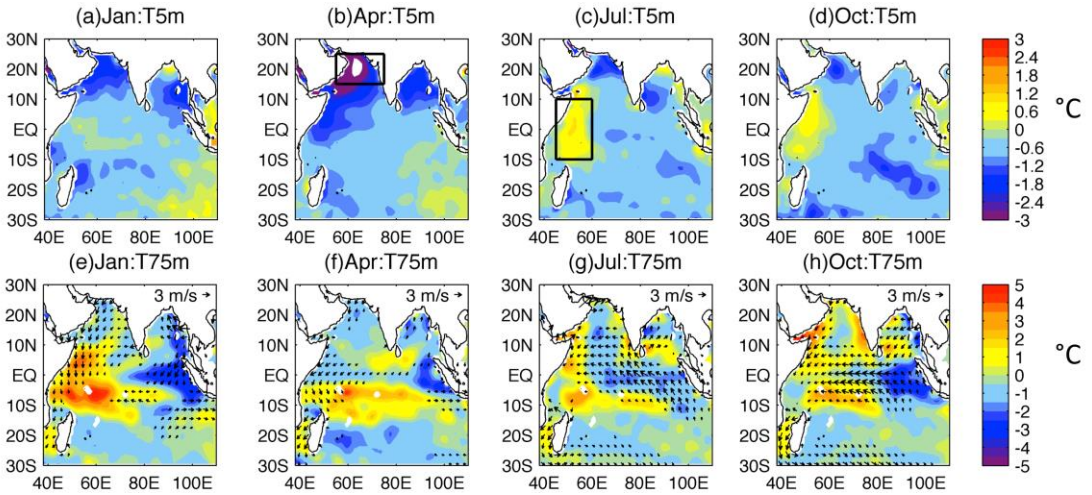

Figure 4.1 Biases of MME SSTs for (a) January, (b) April, (c) July, and (d) October, and biases of MME temperature at 75 m and surface winds for (e) January, (f) April, (g) July, and (h) October. Wind speed biases <1 m s^{-1} have been masked. Regions over the Arabian Sea (55°–70°E, 15°–25°N) and WEIO (45°–60°E, 10°S–10°N) for computing SST bias and heat budget analysis are indicated by boxes.

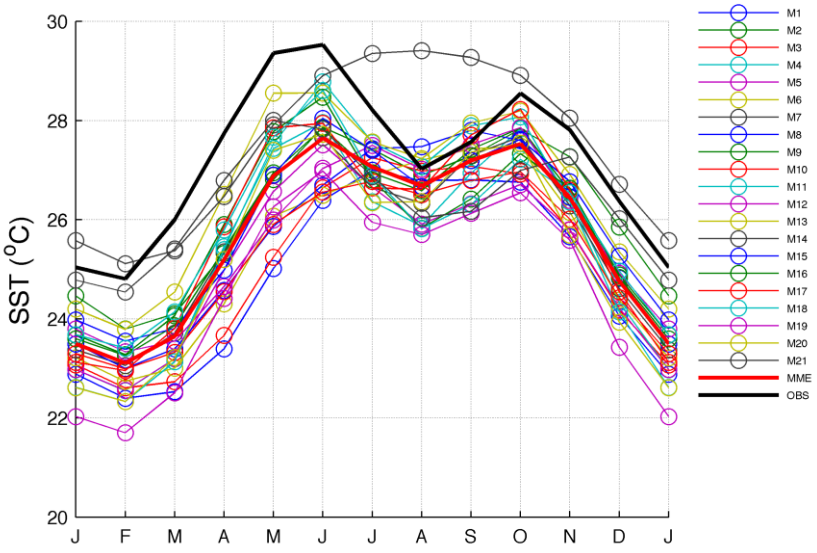

Figure 4.2 Seasonal cycles of SST over the Arabian Sea (55°–70°E, 15°–25°N) for the CMIP5 models. Model labels are referred to Table 2.1.

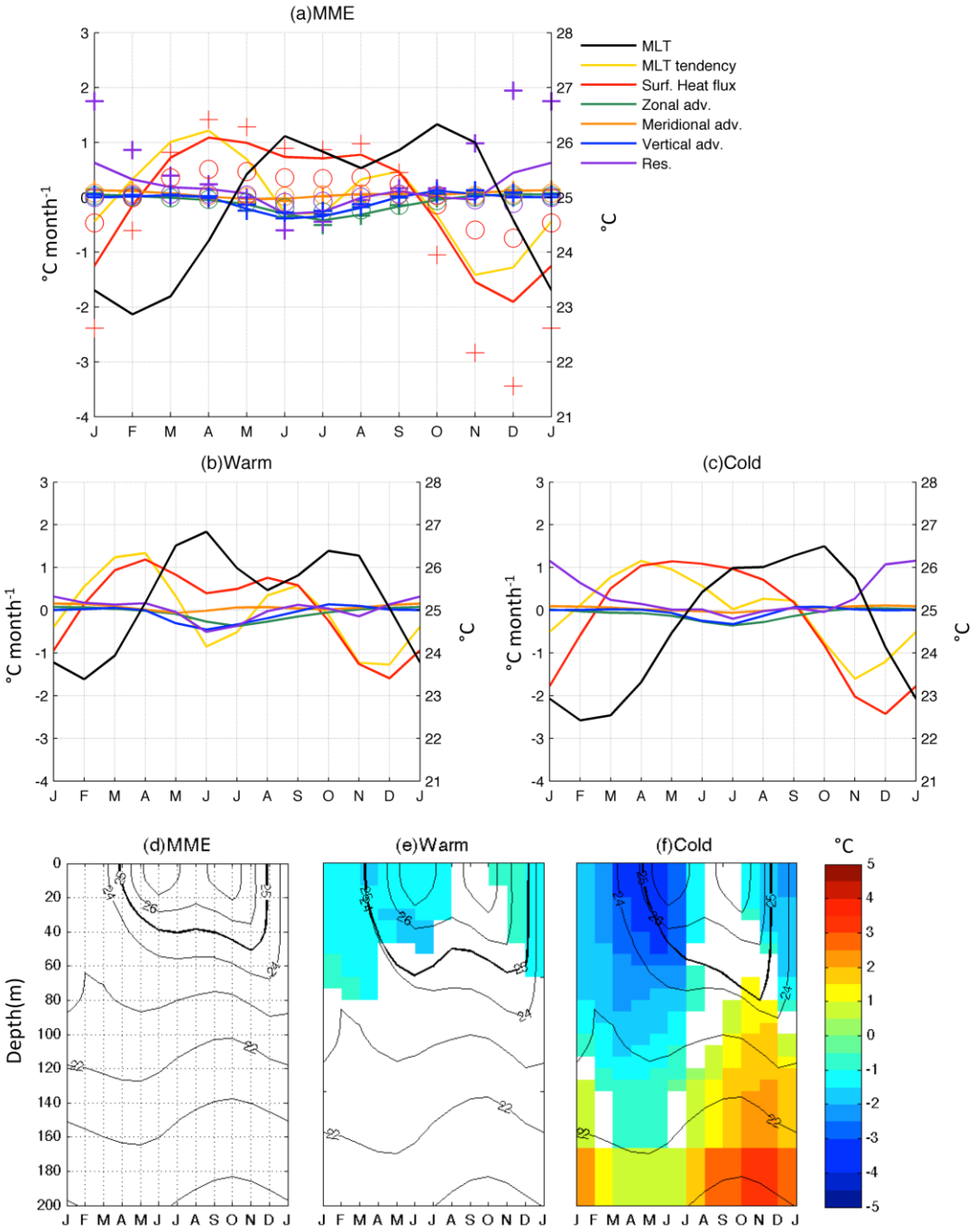

Figure 4.3 Seasonal cycle of upper-50-m ocean heat budget over the Arabian Sea (55°–70°E, 15°–25°N) for (a) MME, (b) four warmest models, and (c) four coldest models. Black lines indicate averaged upper-50-m temperature (°C). Tendencies of the temperature, surface heat fluxes, zonal advection term, meridional advection term, vertical advection term, and residual term are denoted by yellow, red, green, orange, blue, and purple lines, respectively (°C month^{-1}). Seasonal cycles of upper-150-m ocean temperature averaged over the Arabian Sea for (d) observations, (e) three warmest models, and (f) three coldest models. The deviations of temperature from observations with significance at the 95% level using a student *t*–test are shaded by color in (e) and (f). Plus (+) and circle (○) marks indicate each term of the upper ocean heat balance with seasonal minimum (30 m) and maximum (125m) MLD.

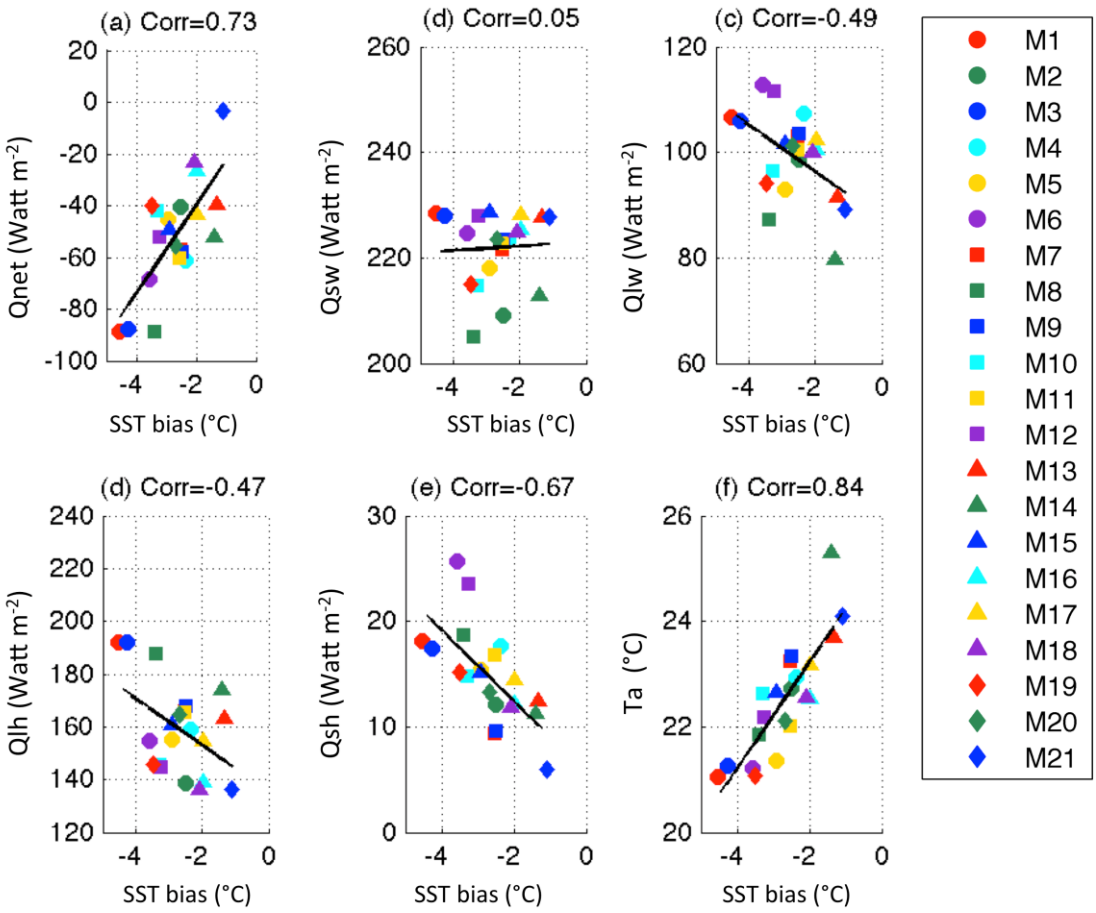

Figure 4.4 Scatterplot of April SST bias (°C) over the Arabian, Sea (55°–70°E, 15°–25°N) vs. (a) surface net heat fluxes (W m^{-2}), (b) shortwave radiation (W m^{-2}), (c) longwave radiation (W m^{-2}), (d) latent heat fluxes (W m^{-2}), (e) sensible heat fluxes (W m^{-2}), and (f) surface air temperature (°C) averaged during October–March among the CMIP5 models. A correlation coefficient falls in 99%, 95%, and 90% confidence level if it exceeds 0.41, 0.48, and 0.61 for a sampling size of 17 CMIP5 models based on a student *t*–test, respectively. Black solid lines denote the trend line. Model labels are referred to Table 2.1.

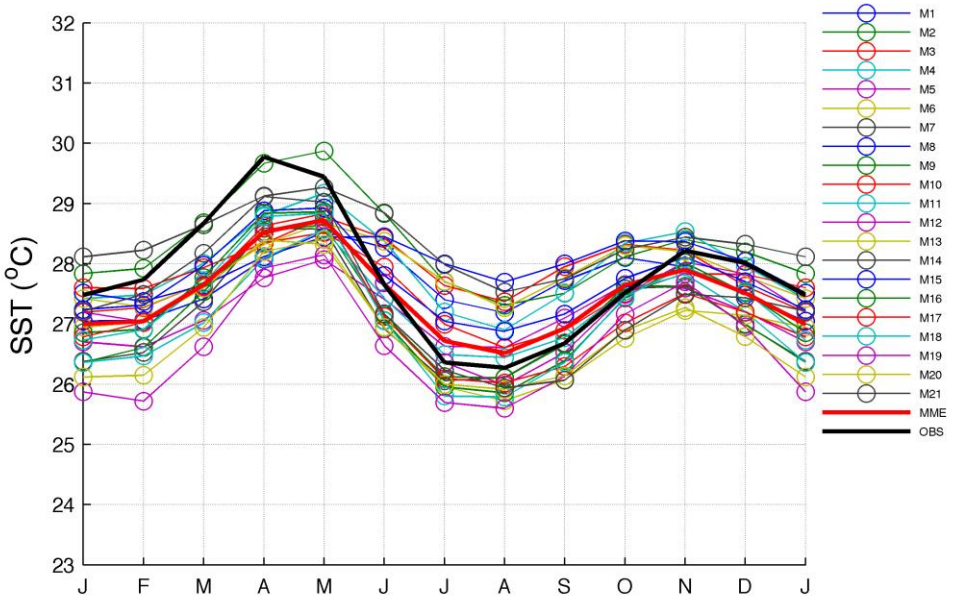

Figure 4.5 Seasonal cycles of SST (°C) over the WEIO (45°–60°E, 10°S–10°N) for the CMIP5 models. Model labels are referred to Table 2.1.

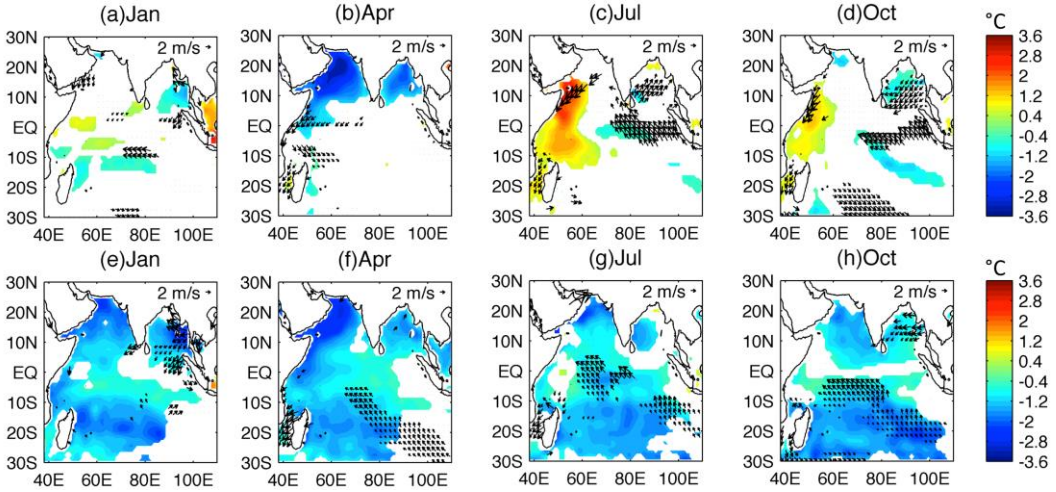

Figure 4.6 Seasonal biases of SST (°C) and surface winds (m s^{-1}) of four warmest models for (a) January, (b) April, (c) July, and (d) October. (e–h) Same as (a–d) but for four coldest models. Values with significance at the 95% level using a student *t*–test are shown.

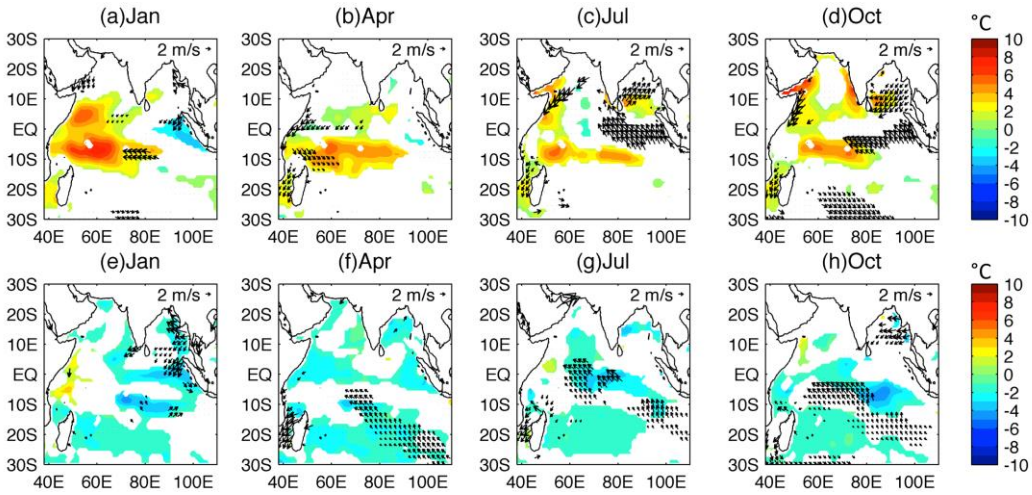

Figure 4.7 Seasonal biases of subsurface temperature (°C) at 75 m and surface winds (m s^{-1}) of four warmest models for (a) January, (b) April, (c) July, and (d) October. (e–h) Same as (a–d) but for four coldest models. Values with significance at the 95% level using a student *t*–test are shown.

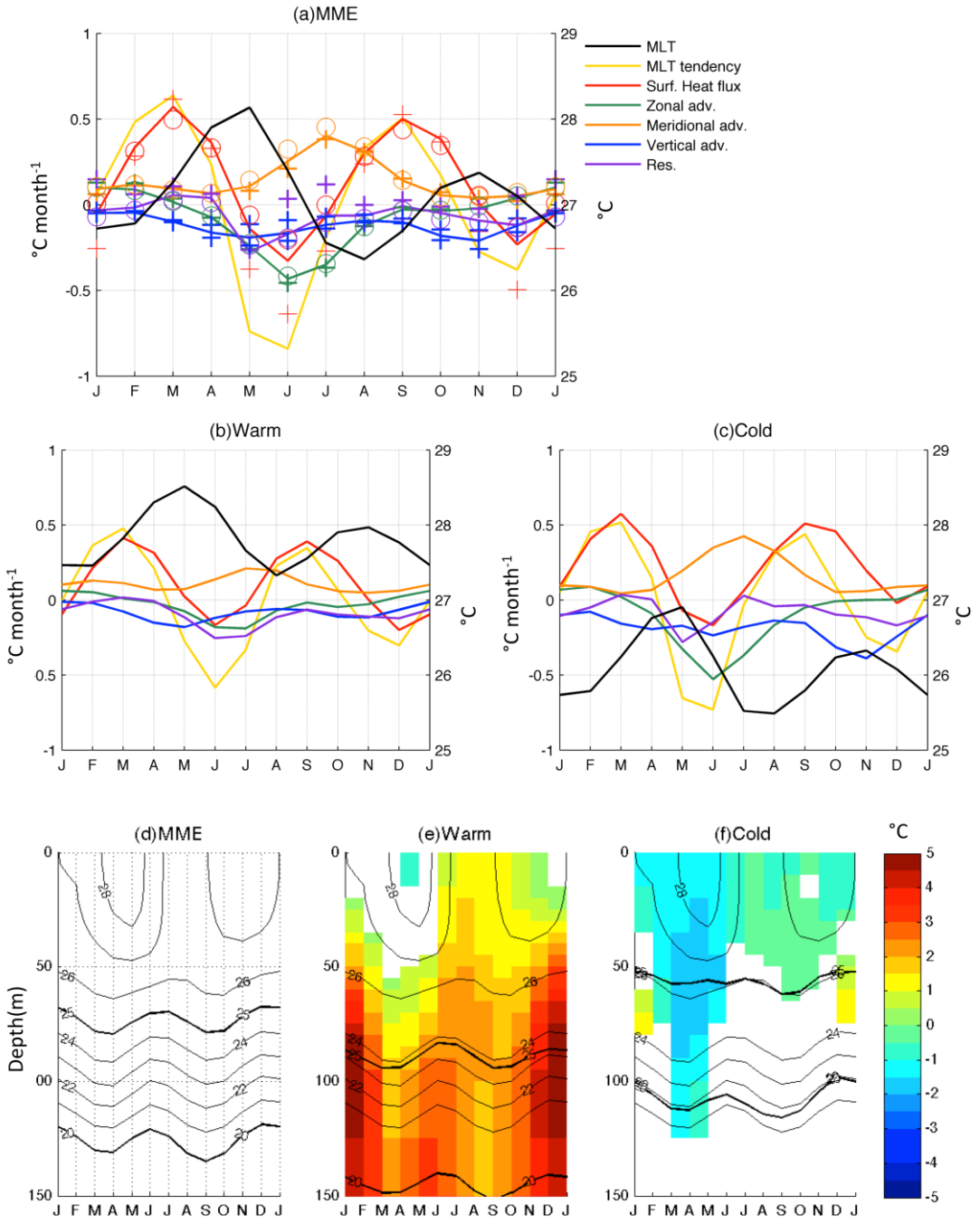

Figure 4.8 Seasonal cycle of upper-50-m ocean heat budget over the WEIO (45°–60°E, 10°S–10°N) for (a) MME, (b) four warmest models, and (c) four coldest models. Black lines indicate the averaged upper-50-m temperature (°C). Tendencies of the temperature, surface heat fluxes, zonal advection term, meridional advection term, vertical advection term, and residual term are denoted by yellow, red, green, orange, blue, and purple lines, respectively (°C month^{-1}). Seasonal cycles of upper-150-m ocean temperature averaged over the WEIO for (d) observations, (e) three warmest models, and (f) three coldest models. The deviations of temperature from observations with significance at the 95% level using a student *t*–test are shaded by color in (e) and (f). Plus (+) and circle (○) marks indicate each term of the upper ocean heat balance with seasonal minimum (35 m) and maximum (65m) MLD.

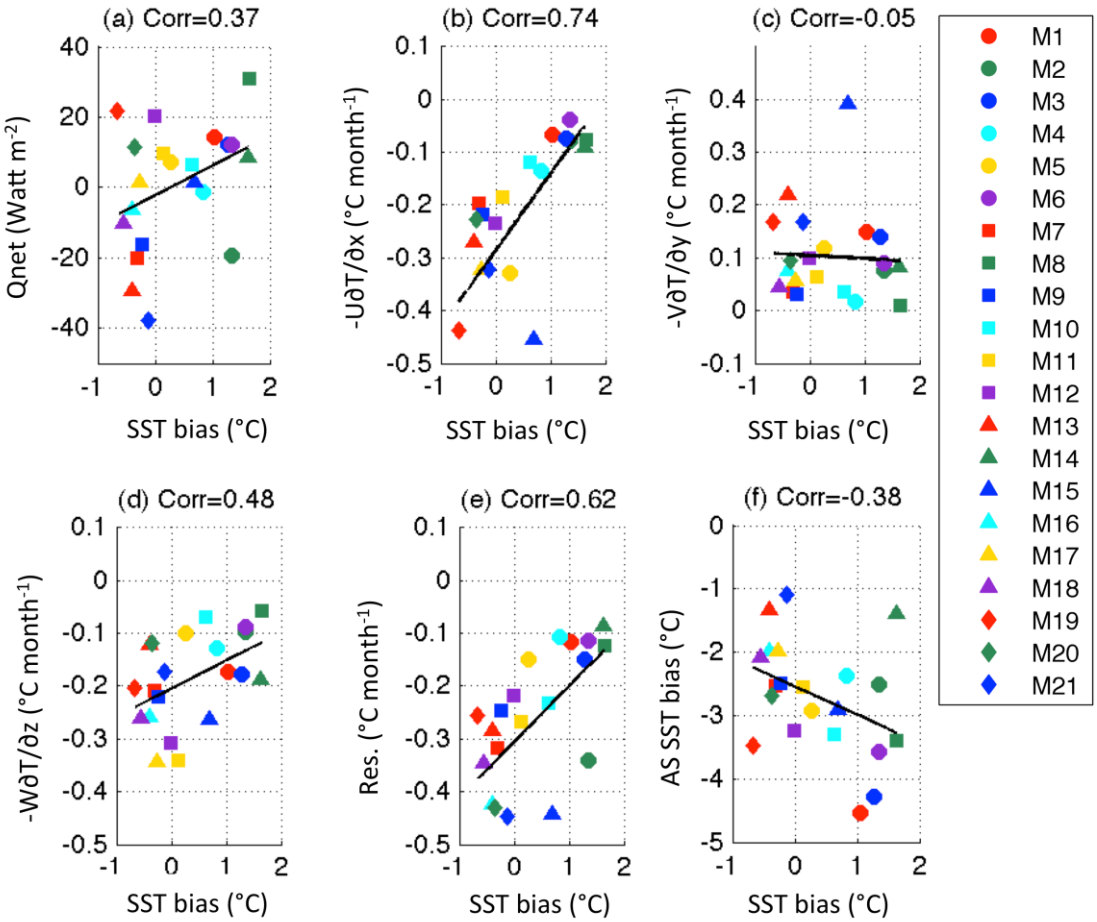

Figure 4.9 Scatterplot of July SST bias (°C) over the WEIO (45°–60°E, 10°S–10°N) vs. (a) surface net heat fluxes (W m^{-2}), (b) zonal advection term (°C $month^{-1}$), (c) meridional advection term (°C $month^{-1}$), (d) vertical advection term (°C $month^{-1}$), (e) residual term (°C $month^{-1}$) in May, and (f) April SST bias (°C) over the Arabian Sea (55°–70°E, 15°–25°N) among the CMIP5 models. A correlation coefficient falls in 99%, 95%, and 90% confidence level if it exceeds 0.41, 0.48, and 0.61 for a sampling size of 17 CMIP5 models based on a student *t*–test, respectively. Black solid lines denote the trend line. Model labels are referred to Table 2.1.

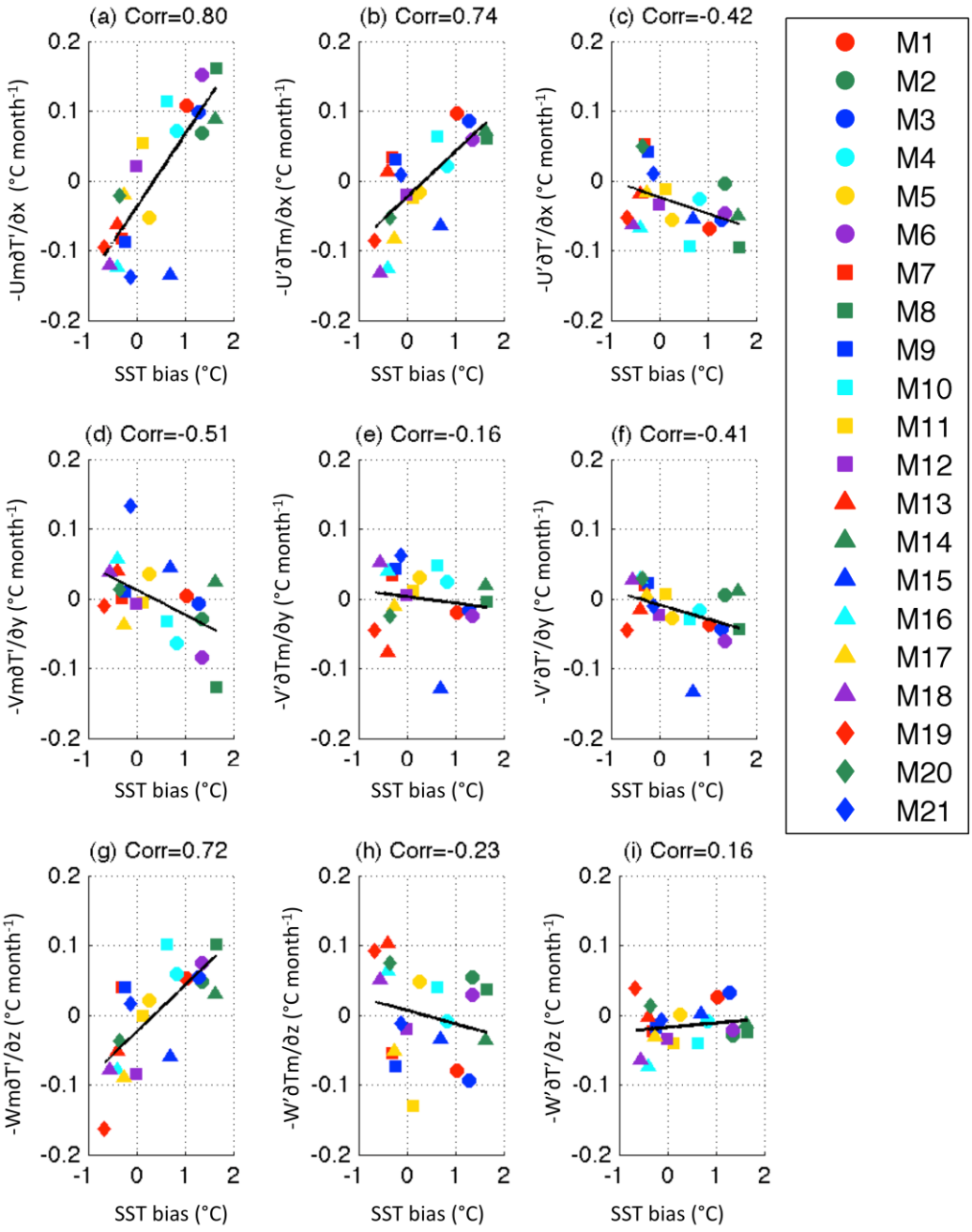

Figure 4.10 Scatterplot of July SST bias (°C) over the WEIO (45°–60°E, 10°S–10°N) vs heat budget decomposed components, namely (a) zonal advection term of temperature deviation by MME current (°C month^{-1}), (b) zonal advection term of MME temperature by current deviation (°C month^{-1}), and (c) zonal advection term of temperature deviation by current deviation (°C month^{-1}) in May among CMIP 5 models. (d)–(f) Same as (a)–(c) but for meridional advection term (°C month^{-1}). (g)–(i) Same as (a)–(c) but for vertical advection term (°C month^{-1}). A correlation coefficient falls in 99%, 95%, and 90% confidence level if it exceeds 0.41, 0.48, and 0.61 for a sampling size of 17 CMIP5 models based on a student *t*–test, respectively. Black solid lines denote the trend line. Model labels are referred to Table 2.1.

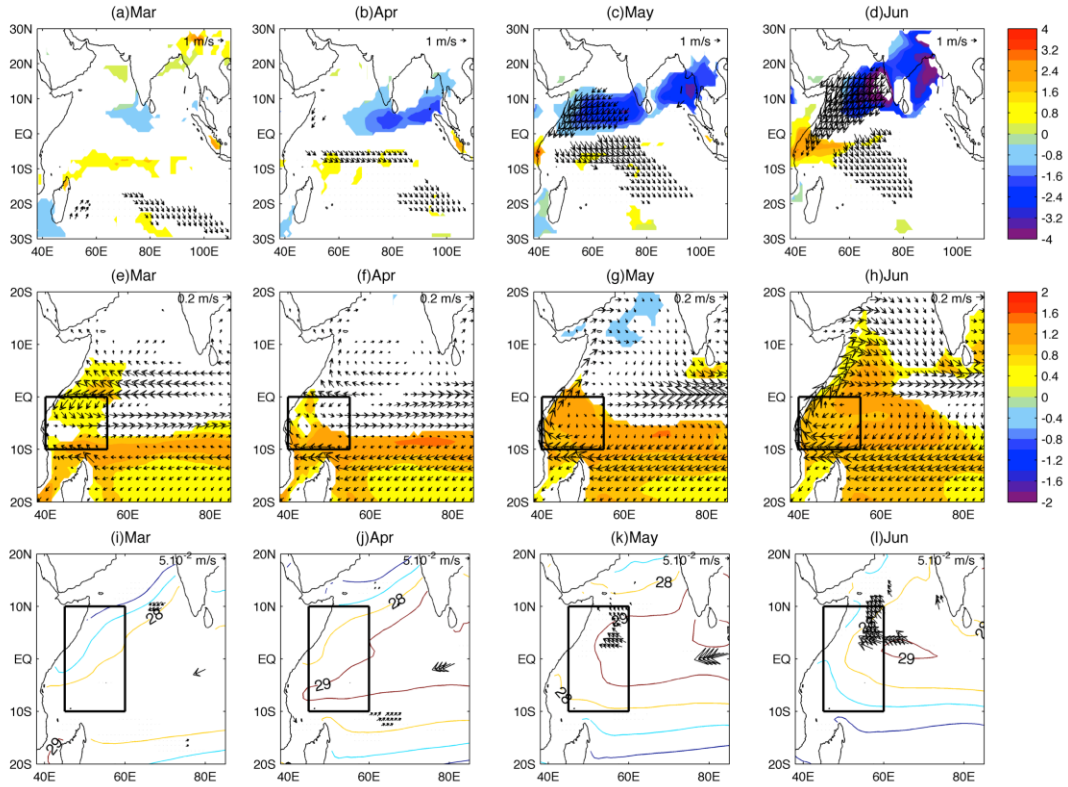

Figure 4.11 Early summer development of MME bias in the WEIO. Precipitation (mm day^{-1}) and surface wind deviations among the CMIP5 models from MME for (a) March, (b) April, (c) May, and (d) June, regressed on July SST bias (°C) over the WEIO (45°–60°E, 10°S–10°N). SST deviations regressed on July SST biases (°C) over the WEIO among the CMIP5 models and monthly mean MME ocean surface currents (m s^{-1}) at a depth of 5 m for (e) March, (f) April, (g) May, and (h) June. Vectors of ocean current speed <0.05 m s^{-1} have been masked. Ocean surface current deviations at a depth of 5 m regressed on July SST bias (°C) over the WEIO, and monthly mean MME SSTs (°C) for (i) March, (j) April, (k) May, and (l) June. Only values with significance at the 99% level using a student *t*–test are shown. Boxes over the southwestern equatorial Indian Ocean (40°–55°E, 10°S–Eq.) and WEIO (45°–60°E, 10°S–10°N) for computing the heat budget analysis are shown in the middle and lower panels, respectively.

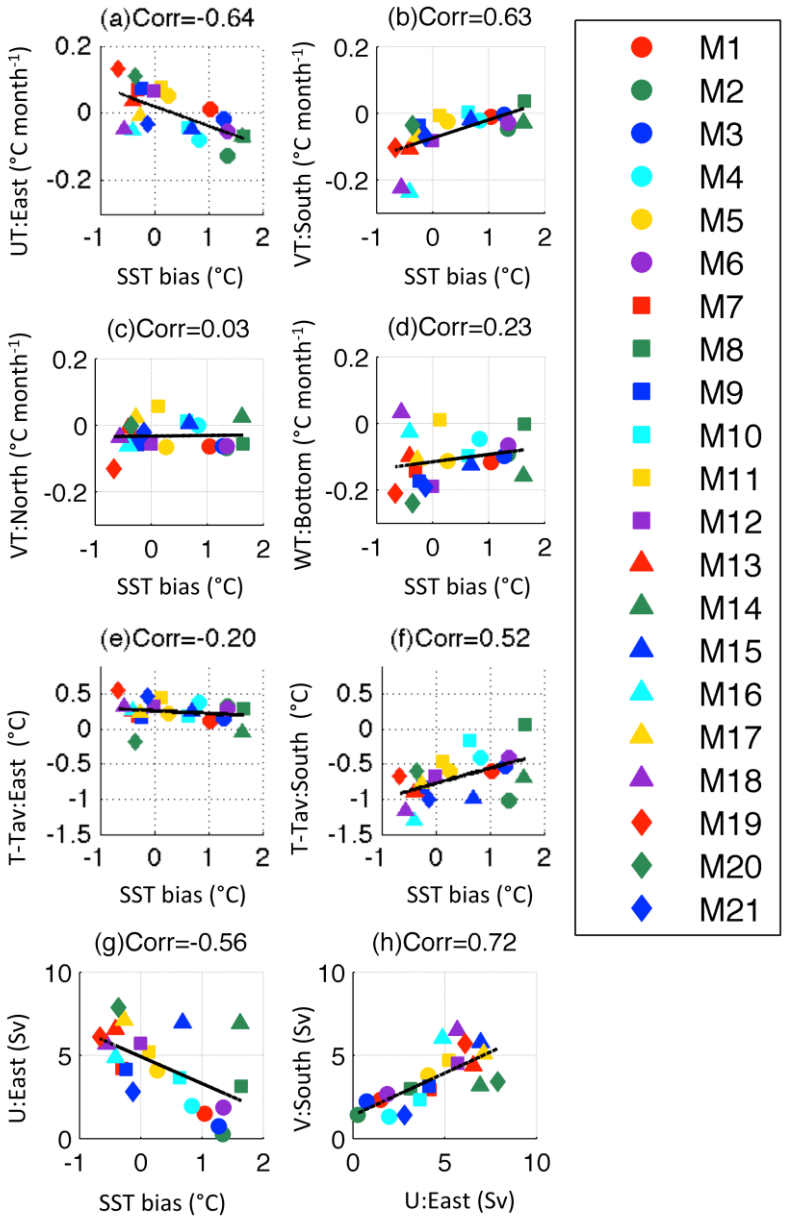

Figure 4.12 Scatterplot analysis for July SST bias considering modified boundary heat flux for advection. Scatterplot of July SST bias (°C) over the WEIO (45°–60°E, 10°S–10°N) vs. (a) zonal heat transport through the eastern, (b) meridional heat transport through the southern, (c) meridional heat transport through the northern, and (d) vertical heat transport through the bottom faces of the box over the southwestern equatorial Indian Ocean (40°–55°E, 10°S–Eq.) in March among the CMIP5 models (Unit: °C month^{-1}). (e)–(f) Same as (a) but for temperature difference between box-averaged temperature and temperature at the eastern and southern faces of the box, respectively (°C). (g) Same as (a) but for eastward transport through eastern face of the box (Sv. = 10^6 m^3 s^{-1}). (i) Scatterplot of March eastward transport through the eastern face of the box vs. northward transport through the southern face (Sv. = 10^6 m^3 s^{-1}). A correlation coefficient falls in 99%, 95%, and 90% confidence level if it exceeds 0.41, 0.48, and 0.61 for a sampling size of 17 CMIP5 models based on a student *t*–test, respectively. Model labels are referred to Table 2.1.

Table 4.1 Pearson correlation value and p-value between number of horizontal and vertical grid and resolution of CMIP5 models and ocean transport at southern and eastern boundary in southwestern equatorial Indian Ocean (40°–55°E, 10°S–Eq.). Student t-test is used to determine p-value of Pearson correlations coefficient that is statistically significant at 5% level (p-value < 0.05).

	Pearson Correlation value	P-value
number of Lat grid vs V:South(Sv)	-0.35	0.12
number of Lon grid vs U:East(Sv)	-0.02	0.94
number of vertical grid vs V:South (Sv)	0.17	0.45
number of vertical grid vs E:East (Sv)	-0.03	0.89
Finest grid VS V:South (Sv)	0.31	0.21
Finest grid VS E:East (Sv)	0.26	0.3

5 Conclusions

This thesis has investigated the role of advection on generating SST anomaly in western Indian Ocean. The development of ocean observation networks and state-of-the-art CGCMs give scientist opportunity to study the ocean process in more details. An effort through CMIP models experiment was carried out in order to study the past, present and future climate changes arising from natural, unforced variability or in response to changes in radiative forcing in a multi-model context. CMIP experiments assess the climate model performance and response for historical and future projections and investigate climate model's predictability. However, both CMIP3 and CMIP5 models still pronounce systematic bias in simulating atmosphere-ocean simulation. One of systematic bias in Indian Ocean is positive IOD-like bias that develops in boreal summer and autumn. This bias is represented in warm (cool) SST bias positive (negative) precipitation bias, strong easterlies (westerlies), too deep (shallow) thermocline bias in WIO (EIO). Previous study suspected that weak summer monsoon bias and insufficient ocean dynamical cooling contribute to warm SST bias in WIO. However, to the best of our knowledge, the ocean advection role on initiating SST bias is still obscure.

In order to complete the puzzle, this thesis focused is to reveal the ocean advection role in generating SST bias in WIO in CMIP5 models. Before evaluating the CMIP5 models, preliminary studies were performed on ocean reanalysis models, namely, GECCO2, SODA3, ORAS4 and GODAS. Monsoon index (Kawamura, 1998) was used to select strong and weak summer monsoon years. During weak (strong) monsoon years, the SST in WIO shows warmer (cooler) SST than usual. The surface wind in weak (strong) summer monsoon is northeasterlies (southeasterlies) in north (south) of equator. Ocean heat budget and scatter plot analysis revealed that anomaly of SST in June is initiated by zonal advection in May for WEIO (45°-60°E, 10°S-10°N). Meanwhile, the anomaly of SST in July is initiated by vertical advection in May for WAS (50°-65°E, 13°-23°N). The vertical advection also initiates the anomaly of SST in April in SWIO (50°-65°E, 15°-5°S). It is noted that vertical advection plays more important role during boreal winter than summer to initiate SST anomaly. This is possibly caused by shallower thermocline during winter.

Evaluation of CMIP5 models revealed that about half of models show warm and cool bias of SST in WEIO during summer monsoon season. Models with warm SST bias display positive IOD-like bias with deep thermocline and easterly wind bias during autumn. The other half of models displays cool bias, which exist throughout the year over entire tropical Indian Ocean. The wind biases over equatorial Indian Ocean are southeasterly during summer and autumn. Ocean heat budget analysis showed consistent result with reanalysis models where warm/cool SST bias could be induced by advection process in WEIO. Heat budget analysis revealed the importance of ocean currents in forming the early summer development of SST biases over the WEIO. Weak southwesterly wind biases induce the surface current bias, which contribute to SST bias in WEIO. The bias in WEIO is attributed to SST bias in southwestern equatorial Indian Ocean (40°–55°E, 10°S–Eq) that is advected by EACC. Meanwhile, bias in southwestern equatorial Indian Ocean is induced by bias in EACC and SECC associated with bias in thermocline depth in southwestern Indian Ocean (0-30°S of WIO region). The SST bias over southwestern equatorial Indian Ocean south of 10°S, which is mainly due to surface heat flux bias, is also advected by EACC and contribute to SST bias in southwestern equatorial Indian Ocean and WEIO.

The new finding of this thesis is emphasized to the contribution of surface current bias in early summer development of SST bias in WIO. The significance of this study contributes to further understanding of the cause of systematic bias over WIO. The new finding of this study poses more questions for future climate prediction. It was documented by previous study that the CMIP5 models show a future IOD-like climate change (Li et al., 2015a). The peak of the SST warming over the WEIO occurs off the equator, somewhat similar to the biases in the historical simulations among the CMIP5 models. Examination of the process causing the future SST changes over the western Indian Ocean will be performed in future work.

References

Adler, R. F., Huffman, G. J., Chang, A., Ferraro, R., Xie, P. P., Janowiak, J., Rudolf, B., Schneider, U., Curtis, S., Bolvin, D., and Gruber, A. (2003). The version-2 global precipitation climatology project (GPCP) monthly precipitation analysis (1979–present). *J. Hydrometeor*., **4(6)**, 1147-1167.

Alexander, M. A., Bladé, I., Newman, M., Lanzante, J. R., Lau, N. C., and Scott, J. D. (2002). The atmospheric bridge: The influence of ENSO teleconnections on air–sea interaction over the global oceans. *J. Climate*, **15(16)**, 2205-2231.

Balmaseda, M. A., Mogensen, K., and Weaver, A. T. (2013). Evaluation of the ECMWF ocean reanalysis system ORAS4. *Q. J. R. Meteorol. Soc.*, **139(674),** 1132-1161.

Behera, S. K., Luo, J. J., Masson, S., Delecluse, P., Gualdi, S., Navarra, A., and Yamagata, T. (2005). Paramount impact of the Indian Ocean dipole on the East African short rains: A CGCM study. *J. Climate*, **18(21)**, 4514-4530.

Behringer, D. W., and Xue, Y. (2004). Evaluation of the global ocean data assimilation system at NCEP: The Pacific Ocean. Eighth Symposium on Integrated Observing and Assimilation Systems for Atmosphere, Oceans, and Land Surface, AMS 84th Annual Meeting, Washington State Convention and Trade Center, Seattle, Washington, 11-15.

Bellenger, H., Guilyardi, É., Leloup, J., Lengaigne, M., and Vialard, J. (2014). ENSO representation in climate models: from CMIP3 to CMIP5. *Clim. Dyn.*, **42(7-8)**, 1999-2018.

Bentsen, M., Bethke, I., Debernard, J. B., Iversen, T., Kirkevåg, A., Seland, Ø., Drange, H., Roelandt, C., Seierstad, I. A., Hoose, C., and Kristjánsson, J. E. (2013). The Norwegian Earth System Model, NorESM1-M – Part 1: Description and basic evaluation of the physical climate, *Geosci. Model Dev.*, **6**, 687-720.

Berlage, H. P., and De Boer, H. J. (1960). On the Southern Oscillation, its way of operation and how it affects pressure patterns in the higher latitudes. *Geofisica pura e applicata*, **46(1)**, 329-351.

Bi, D., Dix, M., Marsland, S. J., O'Farrell, S., Rashid, H., Uotila, P., and Yan, H. (2013). The ACCESS coupled model: description, control climate and evaluation. *Aust. Meteorol. Oceanogr. J*, **63(1)**, 41-64.

Bjerknes, J. (1969). Atmospheric teleconnections from the equatorial Pacific. *Mon. Wea. Rev.*, **97**, 163–172.

Bryan, K. (1969). A numerical method for the study of the circulation of the world ocean. *J. Comput. Phys.,* **4**, 347-376.

Cai, W., and Cowan, T. (2013). Why is the amplitude of the Indian Ocean Dipole overly large in CMIP3 and CMIP5 climate models? *Geophys. Res. Lett.*, **40 (6)**, 1200–1205.

Carton, J. A., and Giese, B. S. (2008). A reanalysis of ocean climate using Simple Ocean Data Assimilation (SODA). *Mon. Wea. Rev.*, **136(8)**, 2999-3017.

Chylek, P., Li, J., Dubey, M. K., Wang, M., and Lesins, G. (2011). Observed and model simulated 20th century Arctic temperature variability: Canadian Earth System Model CanESM2, *Atmos. Chem. Phys. Discuss*., **11**, 22893–22907.

Dee, D. P., Uppala, S. M., Simmons, A. J., Berrisford, P., Poli, P., Kobayashi, S., Andrae, U., Balmaseda, M. A., Balsamo, G., Bauer, P., and Bechtold, P. (2011). The ERA-Interim reanalysis: Configuration and performance of the data assimilation system. *Q. J. R. Meteorol. Soc.*, **137**, 553–597.

Du, Y., Xie, S. P., Yang, Y. L., Zheng, X. T., Liu, L., and Huang, G. (2013). Indian Ocean variability in the CMIP5 multimodel ensemble: the basin mode. *J. Climate*, **26(18),** 7240-7266.

Dufresne, J. L., Foujols, M. A., Denvil, S., Caubel, A., Marti, O., Aumont, O., Balkanski, Y., Bekki, S., Bellenger, H., Benshila, R., and Bony, S. (2013). Climate change projections using the IPSL-CM5 Earth SystemModel: From CMIP3 to CMIP5. *Clim. Dyn.*, **40**, 2123–2165.

Dunne, J. P., John, J. G., Adcroft, A. J., Griffies, S. M., Hallberg, R. W., Shevliakova, E., Stouffer, R. J., Cooke, W., Dunne, K. A., Harrison, M. J., Krasting, J. P., Malyshev, S. L., Milly, P. C., Phillipps, P. J., Sentman, L. T., Samuels, B. L., Spelman, M. J., Winton, M., Wittenberg, A. T., and Zadeh, N. (2012). GFDL's ESM2 Global Coupled Climate–Carbon Earth System Models. Part I: Physical Formulation and Baseline Simulation Characteristics. *J. Climate*, **25**, 6646–6665.

Fathrio, I., Manda, A., Iizuka, S., Kodama, Y., and Ishida, S. (2017). Evaluation of CMIP5 models on sea surface salinity in the Indian Ocean. *IOP Conf. Ser. : Earth Environ. Sci.*, **54**, 012039. IOP Publishing.

Fathrio, I., Iizuka, S., Manda, A., Kodama, Y., Ishida, S., Moteki, Q., Yamada, H., and Tachibana, Y. (2017). Assessment of western Indian Ocean SST bias of CMIP5 models. *J. Geophys. Res. Oceans,* **122,** 3123–3140.

Feng, M., and Meyers, G. (2003). Interannual variability in the tropical Indian Ocean: A two-year time scale of IOD. *Deep Sea Research Part II*, **50(12–13)**, 2263–2284.

Findlater, J. (1969). A major low‐level air current near the Indian Ocean during the northern summer. *Q. J. R. Meteorol. Soc.*, **95(404)**, 362-380.

Fogli, P. G., Manzini, E., Vichi, M., Alessandri, A., Patara, L., Gualdi, S., Scoccimarro, E., Masina, S., and Navarra, A. (2009). INGV-CMCC carbon (ICC): A carbon cycle Earth system model. *CMCC Research Paper*, **61**, 31.

Gaillard, F., Reynaud, T., and Thierry, V. (2016). In situ-based reanalysis of the global ocean temperature and salinity with ISAS: Variability of the heat content and steric height. *J. Climate,* **29**, 1305–1323.

Gaillard, F. (2015). ISAS-13 temperature and salinity gridded fields. SEANOE, doi, 10, 45945.

Gaillard, F., Autret, E., Thierry, V., Galaup, P., Coatanoan, C., and Loubrieu, T. (2009). Quality control of large Argo datasets. *J. Atmos. Oceanic Technol.*, **26,** 337-351.

Giese, B. S., and Ray, S. (2011). El Niño variability in simple ocean data assimilation (SODA), 1871–2008. *J. Geophys. Res*., **116**, C02024.

Goddard, L., and Graham, N. E. (1999). Importance of the Indian Ocean for simulating rainfall anomalies over eastern and southern Africa. *J. Geophys. Res*., **104**, 19,099–19,116.

Griffies, S. M., Winton, M., Donner, L. J., Horowitz, L. W., Downes, S. M., Farneti, R., Gnanadesikan, A., Hurlin, W. J., Lee, H. C., Liang, Z., and Palter, J. B. (2011). The GFDL CM3 Coupled Climate Model: Characteristics of the Ocean and Sea Ice Simulations. *J. Climate*, **24**, 3520–3544.

HadGEM2 Development Team (2011). The HadGEM2 family of Met Office Unified Model climate configurations, *Geosci. Model Dev*., **4**, 723–757.

Huang, C. J., Qiao, F., and Dai, D. (2014). Evaluating CMIP5 simulations of mixed layer depth during summer. *J. Geophys. Res.*, **119**, 2568–2582.

Ishii, M., Shouji, A., Sugimoto, S., and Matsumoto, T. (2005). Objective analyses of SST and marine meteorological variables for the 20th century using COADS and the Kobe Collection. *Int. J. Climatol*., 25, 865-879.

Ishii, M., Kimoto, M., Sakamoto, K., and Iwasaki, S. I. (2006). Steric sea level changes estimated from historical ocean subsurface temperature and salinity analyses. *J. Oceanogr.*, **62(2)**, 155-170.

Iizuka, S., Matsuura, T., and Yamagata, T. (2000). The Indian Ocean SST dipole simulated in a coupled general circulation model. *Geophys. Res. Lett.*, **27(20)**, 3369–3372.

Izumo, T., Montégut, C. B., Luo, J. J., Behera, S. K., Masson, S., and Yamagata, T. (2008). The role of the western Arabian Sea upwelling in the Indian monsoon rainfall variability. *J. Climate*, **21**, 5603–5623.

Johnson, E. S., Bonjean, F., Lagerloef, G. S., Gunn, J. T., and Mitchum, G. T. (2007). Validation and Error Analysis of OSCAR Sea Surface Currents. *J. Atmos. Oceanic Technol.*, **24**, 688–701.

Jungclaus, J. H., Fischer, N., Haak, H., Lohmann, K., Marotzke, J., Matei, D., Mikolajewicz, U., Notz, D., and von Storch, J. S. (2013). Characteristics of the ocean simulations in MPIOM, the ocean component of the MPI-Earth system model, *J. Adv. Model. Earth Syst.*, **5**, 422–446.

Kalnay, E., Kanamitsu, M., Kistler, R., Collins, W., Deaven, D., Gandin, L., Iredell, M., Saha, S., White, G., Woollen, J., Zhu, Y., Leetmaa, A., Reynolds, R., Chelliah, M., Ebisuzaki, W., Higgins, W., Janowiak, J., Mo, K. C., Ropelewski, C., Wang, J., Jenne, R., and Joseph, D. (1996). The NCEP/NCAR 40-Year Reanalysis Project. *Bull. Amer. Meteor. Soc.*, **77**, 437–471.

Kanamitsu, M., Ebisuzaki, W., Woollen, J., Yang, S. K., Hnilo, J. J., Fiorino, M., and Potter, G. L. (2002). NCEP–DOE AMIP-II Reanalysis (R-2). *Bull. Amer. Meteor. Soc.*, **83**, 1631–1643.

Kawamura, R. (1998). A possible mechanism of the Asian summer monsoon-ENSO coupling. *J. Meteor. Soc. Japan*, **76,** 1009－1027.

Kawamura, R., Matsuura, T., and Iizuka, S. (2001). Role of equatorially asymmetric sea surface temperature anomalies in the Indian Ocean in the Asian summer monsoon and El Niño–Southern Oscillation coupling. *J. Geophys. Res.,* **106**, 4681–4693.

Kim, S. B., Fukumori, I., and Lee, T. (2006). The closure of the ocean mixed layer temperature budget using level-coordinate model fields. *J. Atmos. Ocean Technol.*, **23**, 840-853.

Klein, S. A., Soden, B. J., and Lau, N. C. (1999). Remote sea surface temperature variations during ENSO: Evidence for a tropical atmospheric bridge. *J. Climate.,* **12,** 917–932.

Köhl, A. (2015). Evaluation of the GECCO2 ocean synthesis: transports of volume, heat and freshwater in the Atlantic. *Q. J. R. Meteorol. Soc.*, **141**: 166–181.

Latif, M., Dommenget, D., Dima, M., and Grötzner, A. (1999). The Role of Indian Ocean Sea Surface Temperature in Forcing East African Rainfall Anomalies during December–January 1997/98. *J. Climate*, **12**, 3497–3504.

Lau, W. K. M., and Waliser, D. E. (2011). *Intraseasonal variability in the atmosphere-ocean climate system*. Springer Science & Business Media.

Lee, T., Fukumori, I., and Tang, B. (2004). Temperature advection: Internal versus external processes. *J. Phys. Oceanogr.*, **34**, 1936–1944.

Lee, T., Waliser, D. E., Li, J. L. F., Landerer, F. W., and Gierach, M. M. (2013). Evaluation of CMIP3 and CMIP5 wind stress climatology using satellite measurements and atmospheric reanalysis products. *J. Climate*, **26(16)**, 5810-5826.

Levine, R. C., Turner, A. G., Marathayil, D., and Martin, G. M. (2013). The role of northern Arabian Sea surface temperature biases in CMIP5 model simulations and future projections of Indian summer monsoon rainfall. *Clim. Dyn*, **41**, 155–172.

Li, G., and Xie, S. P. (2012). Origin of tropical-wide SST biases in CMIP multi-model ensembles. *Geophys. Res. Lett.,* **39**.

Li, G., Xie, S. P., and Du, Y. (2015a). Monsoon-induced biases of climate models over the tropical Indian Ocean. *J. Climate*, **28**, 3058–3072.

Li, G., Xie, S. P., and Du, Y. (2015b). Climate model errors over the south Indian Ocean thermocline dome and their effect on the basin mode of interannual variability. *J. Climate*, **28**, 3093–3098.

Li, T., Zhang, Y., Lu, E., and Wang D. (2002). Relative role of dynamic and thermodynamic processes in the development of the Indian Ocean dipole: An OGCM diagnosis. *Geophys. Res. Lett.*, **29(23)**, 2110.

Lloyd, J., Guilyardi, E., Weller, H., and Slingo, J. (2009). The role of atmosphere feedbacks during ENSO in the CMIP3 models. *Atmospheric Science Letters*, **10(3)**, 170-176.

Liu, Z., and Alexander, M. (2007). Atmospheric bridge, oceanic tunnel, and global climatic teleconnections. *Rev. Geophys.*, **45**, RG2005.

Liu, L., Yu, W., and Li, T. (2011). Dynamic and thermodynamic air–sea coupling associated with the Indian Ocean dipole diagnosed from 23 WCRP CMIP3 models. *J. Climate*, **24(18)**, 4941-4958.

Liu, L., Xie, S. P., Zheng, X. T., Li, T., Du, Y., Huang, G., and Yu, W. D. (2014). Indian Ocean variability in the CMIP5 multi-model ensemble: the zonal dipole mode. *Clim. Dyn.*, **43(5-6)**, 1715-1730.

Marathayil, D., Turner, A. G., Shaffrey, L. C., and Levine, R. C. (2013). Systematic winter sea-surface temperature biases in the northern Arabian Sea in HiGEM and the CMIP3 models. *Environ. Res. Lett.*, **8**, 014028.

McPhaden, M. J., Meyers, G., Ando, K., Masumoto, Y., Murty, V. S. N., Ravichandran, M., Syamsudin, F., Vialard, J., Yu, L., and Yu, W. (2009). RAMA: The Research Moored Array for African–Asian–Australian Monsoon Analysis and Prediction. *Bull. Amer. Meteor. Soc.*, **90**, 459–480.

Meehl, G. A., Covey, C., Delworth, T., Latif, M., McAvaney, B., Mitchell, J. F., Stouffer, R. J., and Taylor, K. E. (2007). The WCRP CMIP3 multimodel dataset: A new era in climate change research. *Bull. Amer. Meteorol. Soc*., **88**, 1383–1394.

Meyers, G., McIntosh, P., Pigot, L., and Pook, M. (2007). The years of El Niño, La Niña, and interactions with the tropical Indian Ocean. *J. Climate*, **20**, 2872–2880.

Montégut, C. B., Vialard, J., Shenoi, S. S., Shankar, D., Durand, F., Ethé, C., and Madec, G. (2007). Simulated Seasonal and Interannual Variability of the Mixed Layer Heat Budget in the Northern Indian Ocean. *J. Climate*, **20**, 3249–3268.

Murtugudde, R., and Busalacchi, A. J. (1999). Interannual variability of the dynamics and thermodynamics of the tropical Indian Ocean. *J. Climate*, **12**, 2300–2326.

Murtugudde, R., McCreary, J. P., and Busalacchi, A. J. (2000). Oceanic processes associated with anomalous events in the Indian Ocean with relevance to 1997–1998. *J. Geophys. Res.*, **105(C2)**, 3295–3306.

Nagura, M., Sasaki, W., Tozuka, T., Luo, J. J., Behera, S. K., and Yamagata, T. (2013). Longitudinal biased in the Seychelles dome simulated by 35 ocean-atmosphere coupled general circulation models. *J. Geophys. Res.,* **118**, 831-846.

Nagura, M., Terao, T., and Hashizume, M. (2015). The role of temperature inversions in the generation of seasonal and interannual SST variability in the far northern Bay of Bengal. *J. Climate*, **28**, 3671-3693.

Neelin, J. D. (2011). *Climate change and climate modeling*. Cambridge University Press.

Ng, B., Cai, W., Walsh, K., and Santoso, A. (2015). Nonlinear processes reinforce extreme Indian Ocean Dipole events. *Sci. Rep.* **5**, 11697.

Niedzielski, T. (2014). Chapter Two-El Niño/Southern Oscillation and Selected Environmental Consequences. *Advances in Geophysics*, **55,** 77-122.

Nishida, T., Kitakado, T., and Matsuura, H. (2011). *Validation of the Global Ocean Data Assimilation System (GODAS) data in the NOAA National Centre for Environmental System (NCEP) by theory, comparative studies, applications and sea truth*. Indian Ocean Tuna Commission Rep. IOTC-2011-WPB09-11, 18 pp.

Palastanga, V., Van Leeuwen, P. J., and De Ruijter, W. P. M. (2006). A link between low-frequency mesoscale eddy variability around Madagascar and the large-scale Indian Ocean variability. *J. Geophys. Res.*, 111.

Qu, T., Du, Y., Strachan, J., Meyers, G., and Slingo, J. (2005). Sea surface temperature and its variability in the Indonesian region. *Oceanography*, **18(4)**, 50.

Ramage, C. S. (1971). *Monsoon meteorology* (No. 551.518 R3).

Rao, S. A., Behera, S. K., Masumoto, Y., and Yamagata, T. (2002). Interannual subsurface variability in the tropical Indian Ocean with a special emphasis on the Indian Ocean dipole. *Deep Sea Research Part II: Topical Studies in Oceanography*, **49(7)**, 1549-1572.

Rao, S. A., and Behera, S. K. (2005). Subsurface influence on SST in the tropical Indian Ocean: Structure and interannual variability. *Dyn. Atmos. Oceans*, **39**, 103–135.

Reynolds, R. W., and Smith, T. M. (1994). Improved Global Sea Surface Temperature Analyses Using Optimum Interpolation. *J. Climate*, **7**, 929–948.

Reynolds, R. W., Rayner, N. A., Smith, T. M., Stokes, D. C., and Wang, W. (2002). An improved in situ and satellite SST analysis for climate. *J. Clim*ate, **15**, 1609–1625.

Rotstayn, L. D., Jeffrey, S. J., Collier, M. A., Dravitzki, S. M., Hirst, A. C., Syktus, J. I., and Wong, K. K. (2012). Aerosol- and greenhouse gas-induced changes in summer rainfall and circulation in the Australasian region: a study using single-forcing climate simulations. *Atmos. Chem. Phys.*, **12**, 6377–6404.

Saji N. H., Goswami B. N., Vinayachandran, P. N., and Yamagata, T. (1999). A dipole mode in the tropical Indian Ocean. *Nature*, **401**, 360–363.

Saji, N. H., and Yamagata, T. (2003). Structure of SST and surface wind variability during Indian Ocean Dipole mode events: COADS observations. *J. Clim*ate, **16**, 2735–2751.

Saji, N. H., Xie, S. P., and Yamagata, T. (2006). Tropical Indian Ocean variability in the IPCC 20th-century climate simulations. *J. Climate*, **19**, 4397–4417.

Sandeep, S., and Ajayamohan, R. S. (2014). Origin of cold bias over the Arabian Sea in Climate Models. *Sci. Rep.*, **4**, 6403.

Santoso, A., Sen Gupta, A., and England, M. H. (2010). Genesis of Indian Ocean mixed layer temperature anomalies: A heat budget analysis. *J. Climate*, **23**, 5375–5403.

Schott, F. A., and McCreary Jr, J. P. (2001). The monsoon circulation of the Indian Ocean. *Prog. Oceanogra*., **51**, 1–123.

Schott, F. A., Xie, S. P., and McCreary, J. P. (2009). Indian Ocean circulation and climate variability. *Rev. Geophys*., **47** (1), RG1002.

Schmidt, G. A., Kelley, M., Nazarenko, L., Ruedy, R., Russell, G. L., Aleinov, I., Bauer, M., Bauer, S. E., Bhat, M. K., Bleck, R., and Canuto, V. (2014). Configuration and assessment of the GISS ModelE2 contributions to the CMIP5 archive. *J. Adv. Model. Earth Syst.*, **6**, 141–184.

Shaji, C., Iizuka, S., and Matsuura, T. (2003). Seasonal Variability of Near-Surface Heat Budget of Selected Oceanic Areas in the North Tropical Indian Ocean. *J. Oceanogr.*, **59,** 87-103.

Shankar, D., Vinayachandran, P. N., and Unnikrishnan, A. S. (2002). The monsoon currents in the northern Indian Ocean. *Prog. Oceanogra.,* **52(1)**, 63–120.

Shinoda, T., Hendon, H. H., and Alexander, M. A. (2004). Surface and subsurface dipole variability in the Indian Ocean and its relation with ENSO. *Deep Sea Research Part I: Oceanographic Research Papers*, **51(5)**, 619-635.

Slingo, J., Spencer, H., Hoskins, B., Berrisford, P., and Black, E. (2004). The meteorology of the western Indian Ocean and the influence of the east African highlands. *Philos. Trans. Roy. Soc. London*, A363, 25–42.

Taylor, K. E., Ronald, J. S., and Meehl, G. A. (2012). An overview of CMIP5 and the experiment design. *Bull. Amer. Meteorol. Soc.*, **93**, 485–498.

Tokinaga, H., and Tanimoto, Y. (2004). Seasonal transition of SST anomalies in the tropical Indian Ocean during El Niño and Indian Ocean Dipole years. *J. Meteor. Soc. Japan*, **82**, 1007–1018.

Tomczak, M., and Godfrey, J. S. (1994). *Regional oceanography: An introduction. elsevier science ltd,* 660, 10591-5153.

Tozuka, T., Yokoi, T., and Yamagata, T. (2010). A modeling study of interannual variations of the Seychelles Dome, *J. Geophys. Res.*, **115**, C04005.

Vialard, J., Duvel, J. P., McPhaden, J. P., Bouruet-Aubertot, P., Ward, B., Key, E., Bourras, D., Weller, R., Minnett, P., Weill, A., Cassou, C., Eymard, L., Fristedt, T.,

Basdevant, C., Dandonneau, Y., Duteil, O., Izumo, T., Montégut, C. B., Masson, S., Marsac, F., Menkes, C., and Kennan, S. (2009). Cirene: Air—Sea Interactions in the Seychelles—Chagos Thermocline Ridge Region. *Bull. Amer. Meteor. Soc*., **90**, 45–62.

Vinayachandran, P. N., Iizuka, S., and Yamagata, T. (2000). Indian Ocean dipole mode events in an ocean general circulation model. *Deep Sea Research Part II: Topical Studies in Oceanography*, **49**, 1573–1596.

Vinayachandran, P. N., and Yamagata, T. (1998). Monsoon response of the sea around Sri Lanka: Generation of thermal domes and anticyclonic vortices. *J. Phys. Oceanogr.*, **28**, 1946–1960.

Voldoire, A., Sanchez-Gomez, E., y Mélia, D. S., Decharme, B., Cassou, C., Sénési, S., Valcke, S., Beau, I., Alias, A., Chevallier, M., and Déqué, M. (2013). The CNRM-CM5.1 global climate model: Description and basic evaluation. *Clim. Dyn.*, **40**, 2091–2121.

Watanabe, M., Suzuki, T., O'ishi, R., Komuro, Y., Watanabe, S., Emori, S., Takemura, T., Chikira, M., Ogura, T., Sekiguchi, M., and Takata, K. (2010). Improved Climate Simulation by MIROC5: Mean States, Variability, and Climate Sensitivity. *J. Climate*, **23**, 6312–6335.

Watanabe, S., Hajima, T., Sudo, K., Nagashima, T., Takemura, T., Okajima, H., Nozawa, T., Kawase, H., Abe, M., Yokohata, T., Ise, T., Sato, H., Kato, E., Takata, K., Emori, S., and Kawamiya, M. (2011). MIROC-ESM 2010: model description and basic results of CMIP5-20c3m experiments. *Geosci. Model Dev.*, **4**, 845-872.

Wang, C., Zhang, L., Lee, S. K., Wu, L., and Mechoso, C. R. (2014). A global perspective on CMIP5 climate model biases. *Nature Climate Cha*nge, **4(3)**, 201-205.

Webster, P. J., and Yang, S. (1992). Monsoon and ENSO: Selectively interactive systems. *Q. J. R. Meteorol. Soc.*, **118**, 877-926.

Webster, P. J., Moore, A. M., Loschnigg, J. P., and Leben, R. R. (1999). Coupled oceanic-atmospheric dynamics in the Indian Ocean during 1997–98. *Nature*, **401**, 356–360.

Wyrtki, K. (1969). An equatorial jet in the Indian Ocean. *Science*, **181**, 262–264.

Xie, P., and Arkin, P. A. (1997). Analyses of Global Monthly Precipitation Using Gauge Observations, Satellite Estimates, and Numerical Model Predictions. *J. Climate*, **9**, 840–858.

Xie, S. P., Annamalai, H., Schott, F. A., and McCreary Jr, J. P. (2002). Structure and mechanisms of south Indian Ocean climate variability. *J. Climate*, **15**, 864–878.

Xie, S. P., Hu, K., Hafner, J., Tokinaga, H., Du, Y., Huang, G., and Sampe, T. (2009). Indian Ocean capacitor effect on Indo-western Pacific climate during the summer following El Niño. *J. Climate*, **22**, 730–747.

Xiao-Ge, X., Tong-Wen, W., and Jie, Z. (2013). Introduction of CMIP5 experiments carried out with the climate system models of Beijing Climate Center. Adv. *Clim. Change Res.*, **4(1)**, 41-49.

Yang, J., Liu, Q., and Liu, Z. (2010). Linking Observations of the Asian Monsoon to the Indian Ocean SST: Possible Roles of Indian Ocean Basin Mode and Dipole Mode. *J. Climate*, **23**, 5889–5902.

Yang, W., Seager, R., Cane, M. A., and Lyon, B. (2015). The rainfall annual cycle bias over East Africa in CMIP5 coupled climate models. *J. Climate*, **26**, 9789–9802.

Yokoi, T., Tozuka, T., and Yamagata, T. (2008). Seasonal Variation of the Seychelles Dome. *J. Climate*, **21**, 3740–3754.

Yoshida, K. (1959). A theory of the Cromwell current and of the equatorial upwelling - An interpretation in a similarity to a coastal circulation. *J. Oceanogr. Soc. Japan*, **15**, 159–170.

Yukimoto, S., Adachi, Y., Hosaka, M., Sakami, T., Yoshimura, H., Hirabara, M., Tanaka, T. Y., Shindo, E., Tsujino, H., Deushi, M. and Mizuta, R., Yabu, S., Obata, A., Nakano, H., Koshiro, T., Ose, T., and Kitoh, A. (2012). A New Global Climate Model of the Meteorological Research Institute: MRI-CGCM3-Model Description and Basic Performance. *J. Meteor. Soc. Japan*, **90A**, 23-64.

Zheng, X. T., Gao, L., Li, G., and Du, Y. (2016). The southwest Indian Ocean thermocline dome in CMIP5 models: Historical simulation and future projection. *Adv. Atmos. Sci.*, **33**, 489–503.

List of Acronyms

AMIP	Atmospheric model intercomparison project
AS	Arabian Sea
AVISO	Archiving, Validation and Interpretation of Satellite Oceanographic data
CPC	Climate Prediction Center
CGCM	Coupled global circulation model
CMIP	Coupled model intercomparison project
CMIP3	CMIP phase three
CMIP5	CMIP phase five
DJF	December, January and February
EACC	East African coastal current
ECCO	Estimating the Circulation and Climate of the Ocean
ECMWF	European Centre for Medium-Range Weather Forecasts
EIO	Eastern Indian Ocean
ENSO	El Niño southern oscillation
ERA	ECMWF Re-Analysis
GCM	Global circulation model
GECCO	German contribution of the Estimating the Circulation and Climate of the Ocean
GODAS	NCEP Global Ocean Data Assimilation System
IOD	Indian Ocean dipole
ISAS13	In Situ Data Analysis System 13
ITCZ	Intertropical convergence zone
JJA	June, July and August
MAM	March, April and May
MLD	Mixed layer depth
MLT	Mixed layer temperature
MME	Multi model of ensemble mean
NCAR	National Center for Atmospheric Research

NCEP	National Centers for Environmental Prediction
NOAA	National Oceanic and Atmospheric Administration
ORAS4	Ocean reanalysis system 4
OSCAR	The NOAA Ocean Surface Current Analyses - Real Time
RAMA	Research Moored Array for African-Asian-Australian Monsoon Analysis and Prediction
RCP	representative concentration pathways
RES	Residual term
SECC	South equatorial counter current
SEIO	Southeastern Indian Ocean
SODA	Simple Ocean Data Assimilation
SON	September, October and November
SST	Sea surface temperature
SWIO	Southwestern Indian Ocean
WAS	Western Arabian Sea
WEIO	Western Equatorial Indian Ocean
WGCM	Working group of climate modeling
WIO	Western Indian Ocean
WOA	World Ocean Atlas
Z20	Depth of 20 ℃ isothermal surface

Appendix

Contribution of convective adjustment process to residual term in heat budget with a fixed mixed layer depth

Kim et al. (2006) and Nagura et al. (2015) discussed the formulation of mixed layer heat budget with a variable MLD. In the case of variable MLD, the mixed layer temperature is governed by the following equation without a horizontal temperature advection term:

$$\frac{\partial T}{\partial t} = \frac{Q}{\rho_0 C_p h} - \frac{\Delta T}{h}\frac{dh}{dt}, \tag{A1}$$

where t, T, Q, h, and ΔT denote the time, mixed layer temperature, surface heat flux, MLD, the temperature difference between mixed layer water and entrained water, respectively, and C_p and ρ_0 denote the specific heat of seawater at constant pressure and a reference density of seawater, respectively. Equation (A1) for an entrainment case in which the MLD increases from Δz_1 at time t to $\Delta z_1 + \Delta z_2$ at $t + \Delta t$ can be discretized as follows (Kim et al., 2006):

$$T_1(n+1) = T_1(n) + \frac{Q}{\rho_0 C_p (\Delta z_1 + \Delta z_2)}\Delta t - \frac{\Delta z_2}{\Delta z_1 + \Delta z_2}\left[T_1(n) - T_2(n)\right], \tag{A2}$$

where Δz is the vertical thickness of the model grid, the subscripts indicate the vertical grid level, and $n + 1$ and n denote the new and old time steps, respectively.

Hydrostatic ocean models have to employ convective adjustment process to remove statically unstable stratification at the end of each time step. One method, called explicit convective adjustment, mixes vertically adjacent grid boxes if they are found to be unstable (Bryan, 1969). Mixing is instantaneous and complete and it does not require intermediate computation of diffusivities. Another method, called implicit convection, parameterizes convective overturning by increasing the coefficient for vertical diffusion, which enters the differential representation of vertical mixing.

Temperature in the uppermost level of an ocean model is governed simply by the following equation without any advection and diffusion terms:

$$\frac{\partial T_1}{\partial t} = \frac{Q}{\rho_0 C_p \Delta z_1}. \tag{A3}$$

Let us consider the change in temperature under surface cooling. The resulting temperature can be written numerically as follows:

$$T_1^*(n+1) = T_1(n) + \frac{Q}{\rho_0 C_p \Delta z_1}\Delta t, \tag{A4}$$

where T^* is the temperature at time step $t + \Delta t$ after all tendency terms (i.e., surface fluxes) have been added. For simplicity, we ignore the effect of salinity on density. If the temperature in the uppermost level of an ocean model becomes cooler than the temperature below that level through surface cooling, the unstable parts of the water column must be homogenized. The resulting temperature can be written as follows:

$$T_1(n+1) = T_2(n+1) = \frac{T_1^*(n+1)\Delta z_1 + T_2^*(n+1)\Delta z_2}{\Delta z_1 + \Delta z_2}. \tag{A5}$$

Let us consider the following conditions:

$$T_2(n) = T_1(n) - \Delta T, \tag{A6}$$

where ΔT is the difference in temperature between levels 1 and 2. Then, the temperature at time step $t + \Delta t$ after all tendency terms including the convective adjustment term have been added becomes:

$$T_1(n+1) = T_2(n+1) = T_1(n) + \frac{Q}{\rho_0 C_p (\Delta z_1 + \Delta z_2)}\Delta t - \frac{\Delta z_2}{\Delta z_1 + \Delta z_2}\Delta T. \tag{A7}$$

Comparing Eq. (A7) with (A4), the tendency due to the convective adjustment (CA) term becomes:

$$T_1(n+1) = T_1(n) + \frac{Q}{\rho_0 C_p \Delta z_1}\Delta t + CA\Delta t, \tag{A8}$$

where

$$CA = -\left[\frac{Q}{\rho_0 C_p \Delta z_1}\frac{\Delta z_2}{(\Delta z_1 + \Delta z_2)} + \frac{\Delta z_2}{(\Delta z_1 + \Delta z_2)}\Delta T\right]. \tag{A9}$$

When the MLD used to compute the surface heat budget is shallower than the actual MLD, ΔT becomes zero. Then, the CA contributes to the warming of the temperature in the uppermost level. Thus, the contribution of the CA acts to compensate the surface

cooling that is overestimated in the heat budget with a constant depth compared with that of a variable MLD.

Figure 3a shows the sensitivities of the terms in the heat budget using seasonal minimum and maximum MLD over the Arabian Sea. The use of a thinner constant MLD amplifies the surface heat flux term, while the differences in advection terms are relatively smaller. It is apparent that the effect of the residual term is amplified when the actual mixed layer is deep during winter and spring. Thus, part of the residual term associated with the CA terms is closely related to surface cooling in the heat budget with a constant MLD.